ELECTRON ENERGY-LOSS SPECTROSCOPY AS AN ATOMIC-SCALE PROBE FOR ELECTRONIC, CHEMICAL, AND PHOTONIC DENSITIES OF STATES IN NANO-SCALE SYSTEMS

A Dissertation

Presented to the Faculty of the Graduate School

of Cornell University

in Partial Fulfillment of the Requirements for the Degree of

Doctor of Philosophy

by

Jee Young Cha

May 2009

ELECTRON ENERGY-LOSS SPECTROSCOPY AS AN ATOMIC-SCALE PROBE FOR ELECTRONIC, CHEMICAL, AND PHOTONIC DENSITIES OF STATES IN NANO-SCALE SYSTEMS

Jee Young Cha, Ph.D.

Cornell University 2009

When bulk materials join at atomic scale, new and unexpected physical regimes can emerge due to nano-scale effects which arise from newly imposed quantum-mechanical boundary conditions at interfaces. To discover and investigate these physical regimes, knowing what the atoms are, and how they are arranged at interfaces is essential. Over the last few decades, electron microscopy and spectroscopy have become indispensable tools to study nano-scale effects because they provide structural as well as electronic, chemical, and optical information at atomic scale.

In this thesis, I used electron energy-loss spectroscopy (EELS) as a primary experimental tool to explore how a nano-scale interfacial chemistry and geometry determine the overall properties of nano-scale systems. By investigating the inelastic scattering events between the incident probe electrons and the nano-scale systems, EELS gives site-specific electronic, chemical, and optical information about the systems. Three topics were investigated with EELS in detail: modifications in the electronic structure of carbon nanotubes in contact with islanding and wetting metals, effects of barrier/electrode interfacial chemistry on tunneling magnetoresistance in sputtered MgO-based magnetic tunnel junctions, and nanometer-scale imaging of and finite size effects on photonic modes of diamond and silicon photonic structures.

In the carbon nanotube project, I used electron tomography to reconstruct the three-dimensional contact geometry between carbon nanotubes and metal contacts, which

showed that carbon nanotubes were deformed by islanding metals, implying that the electronic band structure of a nanotube could be modified by making contact to a metal. EELS measurements on carbon nanotubes deformed by islanding metals showed differences in the C-K fine structure between pristine and deformed regions of the nanotubes, which suggested that the band structure of the nanotubes was modified upon deformation.

In the MgO-based magnetic tunnel junction project, core-loss spectroscopic imaging of the MgO/B-alloy electrode interface showed a clear presence of B as B oxide in the MgO layer due to the inevitable oxidation of the base electrode during radio frequency sputtering of MgO. Subsequent annealing of the magnetic tunnel junctions resulted in a hybrid Mg-B-O layer which still produced high tunnel magnetoresistance and low resistance-area product in thin ($\sim$ 1 nm) Mg-B-O barrier regime, making the thermally stable Mg-B-O a technologically relevant barrier material for magnetic tunnel junctions.

Lastly in the diamond and silicon photonic structure project, I used monochromated EELS in the low energy-loss region to probe optical modes of diamond and silicon photonic structures at nanometer resolution, made possible by retardation effects where emitted radiation by relativistic electrons acted as a virtual light source, coupling to the photonic modes of the diamond and silicon photonic structures. In particular, spatial distributions of the photonic modes and damping of the modes due to finite size effects were investigated in detail.

This thesis provides background information on core- and low-loss EELS and discusses experimental set-ups and results for each project.

BIOGRAPHICAL SKETCH

Judy Jeeyoung Cha was born on May 12^{th}, 1979 in Seoul, South Korea to Kee-chul David Cha and Sinae Grace Kang. She is the eldest of the three children David and Grace have: herself, Ellen, and Brian. At the age of seventeen when she began to feel the weight of the Korean national examination heavy on her shoulder, her family moved to Vancouver, BC, Canada in hopes for better education. There in Vancouver, she named herself Judy and reviewed quadratic equations using a graphics calculator - something she couldn't have dreamt of in Korea. In 1998, she entered Simon Fraser University (SFU) perched on Burnaby Mountain because a bus ride to SFU was shorter than to University of British Columbia (UBC). In her junior year in engineering physics, she met the love of her life, Alex. She obtained a B.A.Sc. with honours in 2003 with a thesis titled, "Transmit and receive coils for magnetic resonance imaging of hyperpolarized ^{3}He gas in ultra-low fields", under the guidance of Prof. M. E. Hayden.

In 2003, she moved to Ithaca, New York to continue her studies in physics as a Ph.D. candidate at School of Applied and Engineering Physics at Cornell. She joined David Muller's group and found the joy of looking at atoms both in gray scale (ADF-STEM) and in color (EELS spectroscopic imaging). Her marital status changed from single to married in May 2007 when she and Alex got married. She completed her Ph.D. in 2009 with her thesis titled "Electron energy-loss spectroscopy as an atomic-scale probe for electronic, chemical, and photonic densities of states in nano-scale systems". After six long and cold winters in Ithaca, she is moving to sunny California, where she will continue her passion of studying small things as a post-doctoral scholar at Stanford.

To my parents.

ACKNOWLEDGEMENTS

Without a doubt, the completion of my Ph.D. thesis would not have been possible without the help and support I received from numerous people. Professors, collaborators, and lab mates have contributed to my research output while my family and friends kept me sane and happy when life at Ithaca seemed confined and too academic. I am glad to have a section dedicated to thank all the people who made it possible for me to come this far.

I express my sincere gratitude to my thesis advisor, Prof. David A. Muller. Truly this dissertation could not have been possible without his financial support and scientific guidance throughout the entire span of my thesis. Daily, he was available for questions and discussions on numerous topics: how to use a particular Matlab script, channeling problems in single columns of atoms, my three thesis projects, and pros and cons of an academic versus an industry career to name a few. I also thank him for giving me freedom to explore different topics even though some of them did not lead to anywhere. Last but not least, I express my genuine appreciation to him for having faith in me despite the fact that he caught me sleeping in the office at least three times.

I earnestly thank Prof. Disalvo and Prof. Arias for serving in my thesis committee. I realize reading a Ph.D. thesis where six years of experiments and results are crammed into one document is not an easy task. I feel the task becomes much harder when the thesis covers a wide range of topics like mine.

Prof. Silcox financially supported me in my second semester as a graduate research assistant in his group. He introduced me to the joys of electron microscopy both experimentally (the good old VG 501B microscope in the basement of Clark Hall) and theoretically (Multislice code by Dr. Earl Kirkland). Dr. Andre Mkhoyan was the first person to teach me how to polish wedge-shaped samples (by hand!) and how to turn knobs and press buttons in the VG 501B microscope. I thank them especially for in-

cluding me as a co-author in their Science paper even though my contribution to the project was small.

Prof. Arias and his students, Jean-Francois Briere and Ivan P. Daykov, contributed to my carbon nanotube project by calculating the equilibrium shape of a carbon nanotube sitting on a palladium plane, which was a valuable confirmation to my experimental results. Regarding the nanotube project, I also thank Prof. Sethna who initially helped me in formulating the energy balance equation (which is in Appendix A) analytically.

The MgO-based magnetic tunnel junctions work was truly a collaborative effort between myself and John Read from Prof. Buhrman's group. Much credit needs to go to John who initiated the project, grew all the samples, and measured the magnetic tunnel junction properties. John is an excellent colleague whose endless passion for the subject is quite contagious. He encouraged me, and treated me as an expert in electron microscopy. Thanks to John, I finally made a mental leap and accepted the notion that I was a microscopy expert (at least among non-microscopists). He taught me how to collaborate with peers professionally. I thank Prof. Buhrman also for his questions which were always probing and timely.

I thank Dr. Matthew Weyland for training me on Tecnai F20 and for teaching me electron tomography. Looking back, I am especially grateful for his patient mentoring because I was only a confused second year graduate student when he trained me. I thank Dr. Martin Couillard for introducing me to the beauty of low-loss EELS. His research interest in Cherenkov radiation and his gentle encouragement pushed me to develop low-loss EELS as a probe for optical modes of nano-scale photonic structures. On this note, I thank Eric Smith, my summer REU student in 2008, because having to mentor him jump-started the photonic crystal project. He was a smart, hard-working student who unfortunately decided to do theory after working with me. Sometimes I wonder, 'What have I done wrong?'.

My office mates who started out at roughly the same time as me - Aycan (who graduated in summer of 2008), Lena, Peter, Jerome - made my daily life in the basement of Clark Hall meaningful and fun. Stimulating research discussions as well as random gossips were a daily occurrence with them. They were all ears whenever I couldn't help but being a chattering box, which I hope wasn't too often. They also made the yearly microscopy conference more like a summer vacation than work. I feel lucky to have such a friendly and happy bunch as office mates. Huolin always has an interesting topic to discuss and I thank him for raising sharp and relevant questions for my research. Julia, Robert, and Pinshane gave me a chance to finally become that senior graduate student - someone that I was not prepared to be until my 6th year in the Ph.D. program. It is fun to watch them and think back at how I used to be in my early years.

I would also like to express my sincere gratitude to Mick Thomas and John Grazul who make graduate students' lives so much easier and much more productive. Without their dedicated work and professionalism, I am sure that much of my time would have been spent on fixing (perhaps trying to fix would be more accurate) things rather than doing experiments. Honestly, they are the unsung heroes for many graduate students including myself. I also thank Dr. Earl Kirkland for his awesome multislice simulation codes. His multislice codes are an indispensable tool for an electron microscopist.

Many thanks to my lunch buddies - Sara, Mike, Jen, and Alex. There were days when the lunch hour with them provided the only excitement for the day. Daily sudoku puzzles were a great reminder that I was not stupid. I also thank my Korean church friends - especially Chanmi, Hyejeong, Sujin unni, sunday school teachers, and KCC members (in the years of 2003-2007) - who made sure that my life at Ithaca wasn't just about getting a Ph.D. degree.

I am deeply deeply grateful to my parents who made a bold decision to move to Canada for their children. I do not doubt for a moment that being educated in Canada

opened many doors for me. Truly without their support and life-changing decision, I will not be where I am today. Ellen and Brian have been a great sister and brother who entertained me whenever I went home during school breaks and reminded me what normal life looked like. At times, I became the better self simply because I felt they looked up to me.

Lastly, thank you Alex for loving me and supporting me steadfastly. Alex, you have been my supporter and the most honest critic. Your unchanging support for me makes me know that everything will be all right. At the same time, your brutal honesty keeps me grounded and helps me see my research as is, not as I want it. I look forward to our new life in sunny California and wherever our future leads us.

TABLE OF CONTENTS

LIST OF FIGURES

CHAPTER 1

INTRODUCTION

The performance of electron microscopes such as the resolving power and the mechanical and electronic stability has steadily improved over the last few decades largely due to the increase in computing power, making electron microscopes an indispensable characterization tool for crystalline and nano-scale materials. Thanks to aberration correctors and monochromators, a new generation of microscopes can achieve a sub-angstrom spatial resolution and 100 meV energy resolution. During my graduate research at Cornell, I applied advanced analytical electron microscopy techniques to a wide range of materials, focusing on three classes of samples: carbon nanotubes with metal contacts, MgO-based magnetic tunnel junctions, and diamond and silicon photonic structures.

Electron energy-loss spectroscopy (EELS) was consistently used to study these samples. By carefully investigating the fine structure and the signal strength of EELS data, the chemical, electronic, and even optical properties of the samples were obtained. In carbon nanotube study, a modified electronic structure of carbon nanotubes deformed by metal contacts was elucidated by comparing changes in C-K EELS edges of deformed and pristine carbon nanotubes. In the MgO-based magnetic tunnel junction project which was a collaborative effort with John Read from Buhrman group, EELS was a primary tool to observe B oxide present in the MgO tunnel barrier layer by tracking the B-K EELS edge across the MgO barrier layer. Spectroscopic images of a MgO/B-alloyed electrode interface showed formation of a hybrid Mg-B-O material at the interface. Finally, monochromated EELS on finite size diamond and silicon photonic structures showed that EELS could be used as a nanometer optical probe to examine a local photonic density of states via induced radiation due to fast electrons. Through

spectroscopic imaging, photonic modes with distinct spatial distributions were observed and finite-size effects on the photonic modes were investigated.

This chapter is two-fold. First, I will briefly discuss the theory of EELS to provide basic background knowledge in EELS. Then, I will provide background information and motivation for each project.

1.1 Theory of Electron Energy-loss Spectroscopy

As high energy electrons pass through a sample in an electron microscope, they go through different types of inelastic scattering events such as surface and bulk plasmons, valence electron excitations, radiative losses such as Cherenkov and transition radiation, and core-level electron excitations. EELS probes these inelastic scattering events by dispersing the transmitted, inelastically scattered electrons according to their energy losses. The first demonstration of EELS of transmitted electrons was reported by Ruthemann who studied the plasmon oscillations of a thin Al foil using a magnetic spectrometer [1]. By carefully examining the fine structure, the energy on-set, and the signal strength of EEL spectra, a lot can be learned about the sample: chemical compositions, oxidation states, local electronic densities of states, and bonding information to name a few.

The energy range of EELS is typically divided into two energy-loss regions: a low- and core-loss region. The low-loss region corresponds to energy losses below 50 eV and includes surface and bulk plasmons, valence electron excitations, and radiative losses. The core-loss region typically corresponds to energy losses above 50 eV where core-level electron excitations occur.

1.1.1 Core-loss EELS for probing local electronic densities of states

When high-energy probe electrons hit a sample (the target), the incident probe electrons can excite sample electrons that are bound at core-levels. The sample electrons are excited to the first available densities of states in the conduction band before relaxing back to the initial core-levels. Figure 1.1 shows one specific excitation, O-K edge (excitation of the 1s electron in an O atom), as an example. This section will describe the theory of core-loss EELS and its relation to the local densities of states.

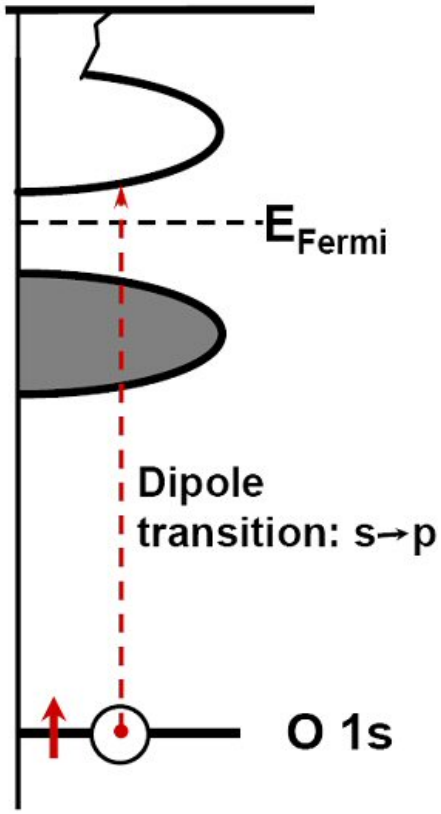

Figure 1.1: Excitation of a 1s electron in oxygen by high-energy probe electrons. The electron bound at the 1s level of oxygen is excited to the conduction band by the high-energy probe electrons. A dipole transition dominates in this process. This graph is reproduced from David Muller's EELS lecture given at Kavli institute summer school in 2006 [2].

The transition rate for the fast probe electron to excite a core-level (inner-shell) electron in a target with an energy loss ΔE is given by Fermi's golden rule (although it is Dirac's work), which states that the probability of a transition occurring per unit time, $\Gamma_{i^\star \to f^\star}$, is given by,

$$\Gamma_{i^\star \to f^\star} = \frac{2\pi}{\hbar} \mid \langle f^\star \mid V \mid i^\star \rangle \mid^2 \delta(E_i - E_f - \Delta E), \tag{1.1}$$

where V is the interaction Hamiltonian and $|f^\star\rangle$ and $|i^\star\rangle$ are the final and initial state of the system (the probe electron + the target electron).

The initial (or the final) state can be taken as the product of the ground (or the excited) state of the target electron and the wavefunction of the probe electron, ignoring the negligible overlap between the target electron and the probe electron. The probe electron can be described as a sum of plane waves, and here a plane wave with only one wave vector will describe the probe electron for simplicity. Hence $|f^\star\rangle$ and $|i^\star\rangle$ become,

$$|f^\star\rangle = e^{-i\mathbf{k_f}\cdot\mathbf{r}'}|f\rangle \tag{1.2}$$

$$|i^\star\rangle = e^{-i\mathbf{k_i}\cdot\mathbf{r}'}|i\rangle \tag{1.3}$$

where $|f\rangle$ and $|i\rangle$ denote the final and initial state of the target electron; $\mathbf{k_f}$ and $\mathbf{k_i}$ denote the final and initial wave vector of the probe electron; and $\mathbf{r}'$ is the coordinate of the probe electron. Letters in bold indicate that they are vectors. The interaction Hamiltonian between the probe and the targe electron is the Coulomb interaction, $-\frac{e^2}{|\mathbf{r}'-\mathbf{r}|}$ where $\mathbf{r}$ is the coordinate of the core-level target electron.

The transition rate in Equation (1.1) becomes then,

$$\Gamma_{i\to f} = \frac{2\pi}{\hbar} \left| \left\langle f \left| \frac{-e^2 e^{i(\mathbf{k_f}-\mathbf{k_i})\cdot\mathbf{r}'}}{\mid \mathbf{r}' - \mathbf{r} \mid} \right| i \right\rangle \right|^2 \delta(E_i - E_f - \Delta E). \tag{1.4}$$

The overlap integral in Equation (1.4) can be performed analytically by applying Bethe's integral [3, 4],

$$\int d\mathbf{R} \frac{e^{i\mathbf{K}\cdot\mathbf{R}}}{R} = \frac{4\pi}{K^2}. \tag{1.5}$$

Hence, the differential cross section in the first Born approximation is given by,

$$\frac{d^2I}{d\Omega dE} = \frac{4\gamma^2}{a_0^2} \sum_{i,f} \left| \frac{\langle i|e^{i\mathbf{q}\cdot\mathbf{r}}|f\rangle}{q^2} \right|^2 \delta(E_i - E_f - \Delta E), \tag{1.6}$$

where $\mathbf{q}$ denotes the momentum transfer, $\mathbf{k_f} - \mathbf{k_i}$, $\gamma = (1 - \beta^2)^{-1/2}$ is the relativistic factor, and a_0 is the Bohr radius. Because $\mathbf{q} \cdot \mathbf{r} \ll 1$ is generally true, the term $e^{i\mathbf{q}\cdot\mathbf{r}}$ can be expanded by Taylor series and the differential cross section becomes,

$$\frac{d^2I}{d\Omega dE} = \frac{4\gamma^2}{a_0^2 q^2} \sum_{i,f} \left| \hat{\epsilon}_q \cdot \langle i|\mathbf{r}|f\rangle \right|^2 \delta(E_i - E_f - \Delta E). \tag{1.7}$$

where $\hat{\epsilon}_q$ is a unit vector in the direction of $\mathbf{q}$. After Taylor expansion, the first non-zero term is a dipole term, $\mathbf{q} \cdot \mathbf{r}$, indicating that a dipole transition dominates in core-level scattering events. Therefore, the selection rule dictates that the angular momentum of the final state l' is given by $l' = l \pm 1$ where l is the angular momentum of the initial state.

When the differential cross section is averaged over all scattering wave vectors (all $\mathbf{q}$'s), which is the case in experiments with a large entrance aperture to the detector at the end of a spectrometer, then EELS can be related to a local density of states in the conduction band, projected in the basis of $r|i\rangle$. This is because the general definition of a local density of states projected onto a state labeled $|n\rangle$ is,

$$d_n(E) = \sum_{all f} |\langle n|f\rangle|^2 \delta(E - E_f). \tag{1.8}$$

Hence, after averaging over all scattering wave vectors, the differential cross section in Equation (1.7) can be separated into a product of two terms: atomic-like matrix elements that vary slowly with energy and angular-momentum-resolved densities of states that represent the near-edge fine structure of EELS [5–7]. We can state the product as below,

$$\frac{d^2I}{d\Omega dE} = \frac{4\gamma^2}{a_0^2} [|\langle f_{L+1}|r|i_L\rangle|^2 \rho_{L+1}(E) + |\langle f_{L-1}|r|i_L\rangle|^2 \rho_{L-1}(E)], \tag{1.9}$$

where $\langle f_{L\pm1}|r|i_L\rangle$ is the matrix elements, $\rho_{L\pm1}(E)$ is the angular-momentum-resolved densities of states, and L is the angular momentum of the initial state. Therefore according to Equation (1.9), core-loss EELS probes the unoccupied, angular-momentum-resolved local density of states.

Care has to be taken, however, when experimental spectra are compared with theory. The separation of the differential cross section in Equation (1.9) is not unique, which means that the density of states is not uniquely defined. Also, Equation (1.9) needs to be modified in the case when the symmetry at the site of the excited atom is lower than orthorhombic [7]. Furthermore, the unoccupied density of states that core-loss EELS probes may not be the ground-state electronic structure of the examined material if there is a strong core hole effect such as cations in ionic materials [8]. For further study of EELS, an EELS book by Egerton [9] and the recent review paper by Rez and Muller [10] are recommended. A more detailed description of EELS and its link to local densities of states can be found in David Muller's Ph.D. thesis [11].

1.1.2 Low-loss EELS for probing local photonic densities of states

Surface and bulk plasmons, valence electron excitations, and radiative losses such as Cherenkov [12] and transition [13] radiation are all low energy-loss scattering events. In EELS, they correspond to the energy range below $\sim$ 50 eV. A big effort in low-loss EELS has been extracting frequency-dependent dielectric constants of materials using Kramers-Kronig analysis [14, 15] and direct bandgap measurements. Steady improvement in energy resolution of electron microscopes due to the recent development of monochromators [16–18] has pushed the research efforts in the low-loss region noticeably in recent years.

The recent efforts in low-loss EELS studies renewed interests in retardation effects induced by the fast probe electrons because, in some cases, radiation generated by the relativistic electrons significantly contributed to the EELS signal in the low energy-loss region, making a direct bandgap measurement and a simple Kramers-Kronig analysis for extracting dielectric constants difficult [19, 20]. While the retardation effects complicate direct bandgap measurements and Kramers-Kronig analysis, they offer new possibilities for probing photonic densities of states [21, 22].

When fast electrons travel through or near a dielectric material, a time-varying dipole moment is induced in the material. Classical electromagnetism shows that a time-varying dipole moment generates radiation. Hence, the fast electrons travelling in a dielectric medium undergo radiative losses. If the speed of the electrons traveling in the material is slow, then the generated radiation damps out quickly and the contribution from the radiative losses to the low-loss EELS signal is negligible. However, when the speed of the electrons exceeds the speed of light in the material due to the high index of refraction, then the radiative waves coherently interfere to build a sizeable contribution to the EELS signal in the low-loss energy region. This particular radiation is called Cherenkov radiation [12]. Another type of radiation called transition radiation can also occur even when the speed of the electrons does not exceed the speed of light in the material. Transition radiation can be emitted when the electrons pass through discontinuities in dielectric constants [13, 23]. Both Cherenkov and transition radiation can be considered as a virtual broad-band light source, which can couple to photonic densities of states. This coupling allows EELS to probe the local photonic density of states.

The energy-loss mechanisms in the low energy-loss region, which mirrors the photonic density of states, can be obtained by considering the force exerted on the fast electron. The exerted force comes from the electric field induced by the fast electron. A

fast electron moving in the z direction can be described as a time-varying current density $\mathbf{j}(\mathbf{r}, \omega)$,

$$\mathbf{j}(\mathbf{r}, \omega) = -e\delta(\mathbf{R} - \mathbf{R}_0)e^{i\omega z/v}\mathbf{z}, \tag{1.10}$$

where $\mathbf{r} = (\mathbf{R}, z)$ and $\mathbf{R_0}$ denotes the location of the electron. $\mathbf{R}$ is the displacement vector in the x-y plane and z is in the direction of the electron path. The current density $\mathbf{j}(\mathbf{r}, \omega)$ induces an electric field $E^{ind}(\mathbf{r}, \omega)$ which can be calculated by using Green tensor,

$$\mathbf{E}^{ind}(\mathbf{r}, \omega) = -4\pi i\omega \int d\mathbf{r}' G(\mathbf{r}, \mathbf{r}', \omega)\mathbf{j}(\mathbf{r}', \omega) \tag{1.11}$$

where the Green tensor G satisfies Maxwell's equations in Gaussian units,

$$\nabla \times \nabla \times G(\mathbf{r}, \mathbf{r}', \omega) - (\omega^2/c^2)\epsilon(\mathbf{r}, \omega)G(\mathbf{r}, \mathbf{r}', \omega) = -1/c^2\delta(\mathbf{r} - \mathbf{r}'). \tag{1.12}$$

The induced electric field $\mathbf{E}^{ind}(\mathbf{r}, t)$ exerts a force back on the electron, resulting in an energy loss. The induced electric field is modulated by the dielectric material and its geometry, as indicated by $\epsilon(\mathbf{r}, \omega)$. The modulation is directly related to the local photonic density of states, which can now be probed by EELS. For detailed theoretical work for connecting EELS to the photonic density of states and Cherenkov radiation, F. J. Garcia de Abajo's work [24] and Jackson [25] are recommended. A detailed description of Cherenkov radiation and its use in Si particles embedded in SiO_2 can be found in Aycan Yurtsever's Ph.D. thesis [26].

1.2 Motivation

Three classes of samples - carbon nanotubes, MgO-based magnetic tunnel junctions, and finite-size silicon and diamond photonic structures - were investigated using EELS. Brief background information on each project is given here to motivate this study. A detailed discussion of experiments, results, and conclusions for each project is given in

later chapters. In particular, Chapter 2 discusses the carbon nanotube project; Chapters 3 and 4 discuss the MgO-based magnetic tunnel junction work, which was done in collaboration with John Read from Buhrman group; and finally Chapter 5 discusses the low-loss, monochromated EELS study on photonic structure work. I conclude my thesis work and discuss future projects in Chapter 6.

1.2.1 Improving contact resistance in carbon nanotube devices

Since the discovery by S. Iijima in 1991 [27] (although a carbon tubular structure was observed by G. Tibbetts in 1984 [28]), carbon nanotubes have been extensively studied for their unique electronic and structural properties. Mechanically, the strength of carbon nanotubes exceeds that of stainless steel due to the strong C-C covalent bond. Typical Young's moduli for carbon nanotubes are in the $1 \sim 10$ TPa range [29–31], which is a factor of two to three higher than that of stainless steel. Electronically, the electronic band structure of a carbon nanotube is determined uniquely by the chirality and the diameter of the nanotube [32, 33].

A single-walled carbon nanotube can be constructed by rolling up a single graphene sheet, as shown in Figure 1.2. A rolling vector $\mathbf{R} = n_1\mathbf{R}_1 + n_2\mathbf{R}_2$ will make a (n_1, n_2) nanotube with radius $r = |\mathbf{R}|/2\pi$. When $n_1 - n_2$ is an integer multiple of 3, then the (n_1, n_2) nanotube is metallic; in all other cases, the nanotube is semiconducting [32–35]. This is because the densities of states of the nanotube cross the Fermi level when $n_1 - n_2$ is an integer multiple of 3. For semiconducting nanotubes, the band gap is inversely proportional to the diameter of the nanotube [35].

The fact that the electronic structure of a carbon nanotube is directly determined by its physical geometry means that modifications in the geometry of the nanotube will

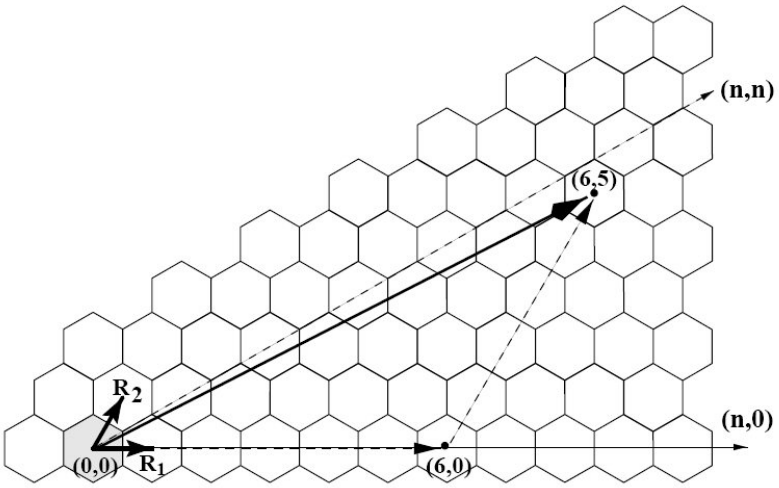

Figure 1.2: Carbon nanotube is made by rolling up a planar graphene sheet. The graph is reproduced from Mintmire and White's Physical Review Letter paper in 1998 [34].

induce corresponding changes in the electronic structure of the nanotube. Extensive theoretical work has been carried out to show that a band gap of a carbon nanotube can close (or open) upon both axial and radial deformations [36–41]. Experimentally, deforming carbon nanotubes by pressing them with an AFM tip showed a reversible change in their conductance by orders of magnitude [42–44].

For a wide, successful application of carbon nanotubes devices, it is essential to control the electronic behavior of the nanotubes precisely. In 1998, a transistor using carbon nanotubes was successfully demonstrated [45]. Theoretical work showed that the nanotube-based transistor is a schottky barrier transistor, where the schottky barrier at the contact dominated the device performance [46]. This suggests that the contact geometry and the subsequent electric field induced around the contact will play a major role in nanotube devices. How does the contact geometry between nanotubes and metals look like in equilibrium? Will nanotubes deform when metals make a contact

to them? Will the band structure of nanotubes be modified upon attaching a contact? Using electron tomography, a three-dimensional contact geometry between nanotubes and metal contacts is reconstructed to answer the possible deformation of nanotubes by the contacts. Moreover, EELS measurements on nanotubes in contact with metals are obtained to study whether structural changes in nanotubes can indeed lead to changes in the electronic structure of nanotubes. Chapter 2 discusses the tomography and EELS results in detail.

1.2.2 What is the tunneling mechanism in CoFeB/MgO/CoFeB magnetic tunnel junctions?

Magnetic random access memory (MRAM) is emerging as one of the candidates for an universal memory solution for its non-volatility, long retention time, nearly infinite write-cycling capability and scalability. The key component in MRAM is the magnetic tunnel junction (MTJ), a sandwich layer of a ferromagnetic electrode / a barrier layer / a ferromagnetic electrode. The resistance across the junction is low/high when the relative orientation of the magnetizations of the two electrodes are parallel/anti-parallel. The difference in resistance between the two states gives rise to tunneling magnetoresistance ratio (TMR), defined as $(R_p - R_{ap})/R_p$ where R_p and R_{ap} are the resistance in the parallel and anti-parallel state respectively [47]. The low resistance (R_p) state is usually considered a "0" while the high resistance (R_{ap}) state is a "1".

Conventionally, amorphous aluminium oxide and titanium oxide were used as a barrier material in MTJs, giving rise to $\sim$ 60 to 70 % TMR [48, 49]. In 2001, two seminal theoretical papers by Butler *et al.* [50] and Mathon *et al.* [51] reported that using magnesium oxide (MgO) as a barrier layer and iron (Fe) as electrodes in a single-crystal

MTJ can produce TMR over 1000 %, which is more than an order of magnitude improvement compared to TMR values of previous MTJs. In 2004, following the theoretical work, experimental results showed that epitaxially grown single-crystal Fe/MgO/Fe MTJs produce TMR of ~ 180 % [52]. In the same year, Parkin *et al.* showed that a poly-crystalline MgO layer that is radio-frequency (rf) sputtered onto CoFe electrodes produces TMR of ~ 220 % at room temperature after annealing [53]. In 2005, Yuasa and Ando group showed that the use of an amorphous CoFeB electrode with a rf sputtered MgO layer produces even higher TMR values after annealing at roughly 350 C° [54–56]. The improved TMR upon annealing the MgO-based MTJs was attributed to the fact that the amorphous CoFeB electrodes crystallized during annealing as the MgO layer imprinted its crystallinity onto the electrodes, meeting the lattice-match condition at the barrier/electrode interface, which was required for the high TMR predicted by the theories.

Despite the recent, remarkable progress in the improvement of TMR values experimentally, discrepancies between the theory and the experimental work in both the TMR values and the crystal structure of the MgO-based MTJs suggest that the direct tunneling via different tunneling states for the majority and minority spin carriers laid out in the theory [50, 51] does not entirely capture sputter-grown MgO-based MTJ systems. Hence, using EELS and spectroscopic imaging, I investigated the effect of annealing, different growth techniques (rf sputtering versus electron-beam evaporation), and B in the electrodes on TMR in search for an explanation for the discrepancy between the theory and the experiments. Chapter 3 discusses the effect of annealing and growth techniques on the structural and chemical properties of CoFeB/MgO/CoFeB MTJ sandwich layers. Chapter 4 discusses the presence of BO_x in the MgO layer, which results in a hybrid Mg-B-O layer after annealing, and shows that Mg-B-O-based MTJs can produce high TMR (~ 200%) and low resistance-area product, making Mg-B-O a tech-

nologically relevant barrier material for the next generation of MRAM technology and high-performance sensing applications.

1.2.3 Probing photonic densities of states with EELS

Manipulation of light - slowing the light, confining it in a specified volume, directing it in a certain way, allowing only a certain frequency region to propagate but not the other regions, etc. - has been a focus of the optics community in recent years for its technological implications. Fiber-optic cables which revolutionized the telecommunications industry are a good example of how light can be used to advance current technologies. Comparing to electrons in semiconductor devices, light has several advantages: greater speed in materials, larger bandwidth to carry information, and lower energy losses [57].

One way to manipulate light is by engineering a photonic crystal, a dielectric material patterned with a periodicity in dielectric constants. By providing periodic variations in the dielectric constant, the nature of photonic modes can be significantly influenced [58]. Therefore, a photonic crystal creates an artificial band structure for photons, in much the same way that a solid-state crystal creates a band structure for electrons. Yablonovitch and John proposed the early idea of using photonic crystals to manipulate light; Yablonovitch's aim was to control radiative properties of materials [59] while John's was to localize photons [60].

Conventionally, photonic crystals and other optical devices have been studied with optics-based techniques such as near-field scanning optical microscopy [61, 62] and lasers coupling to the photonic structures. However, with minaturization of these photonic structures and defect engineering, the photonic modes can be greatly modified by sub-wavelength features that cannot be resolved by optical techniques whose resolu-

tions are diffraction-limited. Electron microscopes on the other hand provide excellent resolution in the range of a sub-Angstrom to a nanometer. Therefore, examining photonic structures with electron microscopes will allow investigation of photonic modes at nanometer to sub-nanometer resolution, a resolution not achievable by optical techniques.

Photonic modes of optical structures were accessed with focused electron beams in electron microscopes via Cherenkov and transition radiation [21]. With recent development of monochromators, the spectral resolution in electron microscopes has improved drastically to enable EELS to probe fine spectral features. Chapter 5 shows experimental observations of photonic modes probed by monochromated EELS. Spatial distributions of the photonic modes and the damping of the modes due to finite-size effects were observed using spectroscopic imaging.

CHAPTER 2

THREE-DIMENSIONAL IMAGING OF CARBON NANOTUBES DEFORMED BY METAL ISLANDS

This chapter discusses three-dimensional (3D) reconstructions of the buried interface between carbon nanotubes and various metal contacts. Using electron tomography, I observe that carbon nanotubes can be deformed by metal contacts, especially when the metals island on nanotubes rather than wet to nanotubes [63]. Since deforming a nanotube can modify the electronic property of the nanotube, the islanding metal contacts can introduce additional resistance terms beyond the already present Schottky barrier. Using EELS, changes in the electronic properties of the nanotubes deformed by islanding metals were investigated. I find that the popular contact metal, palladium, lies on the margin between wetting and islanding, suggesting a strategy to improve the contact resistance in nanotube-based devices by alloying palladium with elements that will improve the wetting property.

2.1 Introduction

Challenging the widespread application of carbon nanotubes [27] in electronic devices, such as transitors [45] and oscillators [64], is the high contact resistance between the nanotubes and metal contacts. The contact resistance varies very widely, increasing exponentially as the nanotube shrinks in diameter [65, 66]. The contact geometry in nanotube devices plays a significant role because the barrier at contact is considered to be a Schottky barrier whose height can be modified very much by the contact geometry [46]. Although the physics of the metal-nanotube contact has been investigated theoretically [46, 67–69], experimental studies on the microscopic contact geometry and its influence on the electrical resistance are lacking. Here, I report on the first direct

experimental study of the contact geometry between metals and nanotubes in 3D, using annular dark-field (ADF) electron tomography [70] with a scanning transmission electron microscope (STEM) at nanometer resolution.

A good electrical contact between a metal and a nanotube is ensured by minimizing the Schottky barrier at the metal-nanotube contact through band alignment [46, 68, 69] and by ensuring that the atoms of the metal and the nanotube are brought into close registration. Given the incommensurate interface between graphite and most metal planes, this is a challenging problem even with flat graphene sheets. Therefore, accommodating an interface with the curvature and chirality of a nanotube will add a new degree of complexity. What would be the equilibrium shape of a nanotube in contact with a metal? A number of possible contact geometries can be expected. The metal may wet to the nanotube, resulting in a good physical contact. Or the metal may island with facets, either leaving voids along the contact surface, or deforming the nanotube to accommodate these facets. The resulting geometric distortions in the latter case will have consequences for the electronic structure of nanotube devices.

Depending on the metal, both wetting and non-wetting (islanding) contacts to nanotubes can occur [71], which results in different equilibrium shapes of the nanotubes. In the wetting case, the metal would conform to the nanotube and the original shape of the tube would be preserved. In the islanding case, the nanotube can be significantly deformed at, and surrounding, the regions in contact with the metal. I employ a simple elastic theory to analytically model the deformation of the nanotubes in the islanding metal contact case and identify key terms in the energy balance between wetting and deformation. In particular, the binding energy of the metal to the nanotube is examined closely as a useful predictor in determining whether the metal would wet or island on nanotubes. Furthermore, density-functional theory (DFT) calculations are carried out

to find if a fully relaxed single-walled nanotube on a flat metal plate will be deformed. The DFT calculation results are compared with the experimental observations and the analytic theory. Thus, I conducted a systematic study of how the nanotube-metal contact geometry would vary with the propensity to wet nanotubes by reconstructing 3D images of nanotubes in contact with different metals at nanometer resolution using electron tomography. I examined from poorly wetting gold (Au), to Au-palladium (Au-Pd) alloy, Pd, and finally strongly wetting titanium (Ti) contacts, and correlated the propensity to wet with a tendency for nanotubes to deform.

2.2 Electron Tomography

The basic idea of tomography is to reconstruct a higher dimensional object from a series of lower dimensional ”slices” or ”sections”. In electron tomography, a 3D object is reconstructed from a series of 2D projection electron micrographs of the object. Three seminal papers, published in 1968 on the tomographic reconstruction of biological structures from electron micrographs, started the field of electron tomography [72–74]. De Rosier and Klug [72] reconstructed a tail of the T-even bacteriophages in 3D by filling the Fourier space from a single electron micrograph, which was possible due to the high helical symmetry the T-even bacteriophage tail possessed. Hoppe *et al.* [73] suggested that reconstruction of an asymmetrical object should be possible given a sufficient number of projection images. Hart [74] proposed a method to improve the contrast in bright-field electron micrographs by using 3D information generated by electron tomography.

Although electron tomography in structural biology has produced many fruitful discoveries over the years, it is only recent that it was applied in materials science. Recent

examples of various electron tomography techniques in materials science include a 3D network of dislocations by weak-beam dark-field electron tomography [75], nonspherical silicon nano-particles embedded in silicon oxide by plasmon tomography [76], and nano-voids in copper interconnects by incoherent bright field tomography [77].

A Fourier space reconstruction and a real space reconstruction method are two main ways to reconstruct a 3D object from 2D projection images. The Fourier space reconstruction is based on the 'central slice theorem', which states that a projection at a given angle is a central slice through the Fourier transform of that object [78]. Thus, a series of projections acquired at different tilt angles equates to a series of central slices at angles normal to the tilt angles in the Fourier space. Following this logic, a 3D Fourier object is built by inserting these central slices to fill the 3D Fourier space, where each slice corresponds to a projection at a particular tilt angle. The object in real space is reconstructed by inverse Fourier transforming the 3D Fourier object. A direct Fourier transform reconstruction was implemented by Crowther *et al.* to reconstruct spherical human wart viruses in 1970 [79].

Although the Fourier space reconstruction is logically straightfoward, real space reconstructions, such as a weighted back-projection and the simultaneous iterative reconstruction technique (SIRT) [80], are used more widely because interpolation between projections is simpler in real space. The back-projection reconstruction method relies on a simple mathematical fact that a point in space can be uniquely described by any three 'rays' passing through the point. If an object is treated as a collection of points, then it can be uniquely described by many 'rays' that define all the points that make up the object. In this sense, a projection image of an object is a set of rays, which partially describe the object, that are projected to the projection plane. To reconstruct an object, each set of rays from each projection is 'back-projected' to fill the 3D object space at

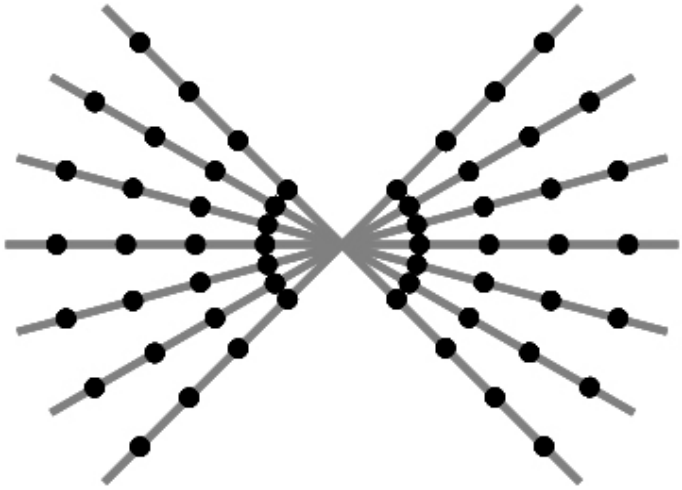

Figure 2.1: Over-sampling of low frequency features and under-sampling of high frequency features. When the tilt increment is fixed, the low spatial frequency features are sampled more than the high spatial frequency features. The dots are closer (higher sampling) to each other near the origin (low spatial frequency) while they are further apart (lower sampling) at the far end from the origin (high spatial frequency).

a particular tilt angle. The superposition of all the back-projected rays will return the shape of the original object. This real space reconstruction method is called a direct back-projection [73, 81].

Reconstructions from the back-projection method tend to be blurred because of the uneven sampling of spatial frequencies. A tilt series with a fixed increment in tilting will result in a high sampling at low spatial frequencies and an under-sampling at high spatial frequencies. Figure 2.1 illustrates this point. The high sampling at low spatial frequencies results in blurred reconstructions. A weighted back-projection compensates this effect by applying a linear weighing filter to the reconstructed object, which weighs the under-sampled high frequencies more. A more complicated reconstruction method SIRT compares the original projections with the projections generated by the reconstructed object. The difference between them is used to modify the previous recon-

struction in order to correct the imperfections due to limited data-set. The comparison between the original and the reconstructed projections and the subsequent modification of the 3D reconstruction are repeated iteratively until a 'best' solution is reached. Further details on the theory and applications of electron tomography can be found in the following references [70, 82, 83].

2.3 Methods

Sample Preparations. Commercially purchased nanotubes (Helix Material Solutions) were dispersed in ethyl ether solvent and the solution was sonicated for roughly 15 minutes to isolate the nanotubes. A drop of solution ($\sim$ 5 micro-liter) was then applied to a copper TEM grid coated with a thin holey carbon film and was allowed to evaporate. Afterward, approximately 10 Å of Au, 15 Å of Au-Pd, 15 Å of Pd, or 25 Å of Ti were deposited on the grid by electron-beam evaporation at $\sim 2\text{x}10^{-6}$ Torr. The samples were examined using a FEI Tecnai F20 STEM with a Fischione model 2020 high-tilt holder. Although the purchased nanotubes were specified to be 90 % pure single-walled carbon nanotubes, many double-walled and multi-walled nanotubes were observed. Experimental results presented in this chapter include multi-walled (double- or triple-walled) nanotubes as well as single-walled nanotubes.

Tilt Series and Reconstructions. To carry out electron tomography, the microscope holder which contained the nanotube sample was tilted over +/- 70 degrees and projected sample images were acquired at 2 degree tilt increments. Annular dark-field (ADF) imaging, which excludes most Bragg scattered beams, was used to suppress the diffraction contrast of the crystalline materials; the intensity then scales monotonically with the atomic number and the sample thickness, making the images suitable for to-

mographic reconstructions [70, 84]. The ADF detector pre-amplifier was replaced with a high-dynamic range pre-amplifier which improved the detective quantum efficiency from 22% to over 90%. This was essential for simultaneously detecting light and heavy elements such as carbon (C) and Au. Tilt series were acquired at either 450 kX magnification or 640 kX magnification. The 450 kX and 640 kX magnifications correspond to roughly 260 nm and 160 nm field of view respectively, acquired at 1024x1024 pixels with a $\sim$ 2 Å diameter focused probe. The acquired ADF STEM tilt series were post-aligned to correct for sample shifts during the tilt and reconstructed using SIRT [80]. I reconstructed six different nanotubes in contact with Au, two nanotubes in contact with Au-Pd, two nanotubes in contact with Pd, and four nanotubes in contact with Ti for the study. One representative reconstruction per metal contact is shown in the result section.

Due to a finite number of projected images, a limited tilt range, and imperfect post-alignment of the tilt series, the final resolution degrades to roughly a nanometer [70]. A 3D viewing program, Amira 3.1.1., was used to view the reconstructed 3D data by creating iso-intensity surfaces and direct volume rendering. Due to the large atomic number difference between C and Au, and resultant differences in image and reconstruction intensities, false color has been used to enhance their relative visibility. The details of the application of electron tomography are covered by Koster [85], and ADF tomography by Midgley et al. [70].

Density-Functional Theory Calculations (J-F. Briere, I. P. Daykov, and T. Arias). The ab initio electronic structure calculations employ the total-energy plane-wave density-functional pseudopotential approach [86] within the local spin-density approximation (LSDA) using a pseudopotential of the Kleinman-Bylander form [87] with p and d non-local corrections. The calculations expand the Kohn-Sham orbitals in a plane-wave basis set with a cutoff energy of 544 eV within an orthorhomic supercell of

dimensions 29.1 X 23.8 X 8.25 Angstroms. Sampling of the Brillioun zone was at 2 k-points, reduced to 1 by time reversal symmetry, and carried out at an effective temperature of 0.0816 eV in order to accurately integrate the Fermi surface. The surface is represented in a supercell slab geometry with 3 layers of palladium metal atoms with the bottom layer held fixed. We employ the analytically continued functional approach [88] to minimize the Kohn-Sham energy with respect to the electronic degrees of freedom, including self-consistency between the electronic orbitals and the Fermi fillings. For all results reported, the relaxation of the total free energy (including entropy associated with the Fermi occupancies) is to within 5 micro-eV. Finally, to determine the final structure, all atoms of the nanotube and the top two layers of the metal slab were relaxed until all forces were less than 0.07 eV/Angstrom.

The relative geometry between the nanotube and the metal surface was determined as follows. The supercell represents a flat Pd 111 surface with a lattice constant matching the relaxed bulk Pd. A (20,0) nanotube was placed on the surface in the deformed geometry expected from the above model with its axis aligned with the [110] direction along the surface and then relaxed.

2.4 Results and Discussions I - Tomographic Reconstructions of Nanotubes with Metal Contacts

I investigated the contact geometry of various metals, Au, Au-Pd alloy, Pd, and Ti, which were electron-beam evaporated onto commercially purchased carbon nanotubes. I obtained tilt series of the nanotubes in contact with these metals using a FEI Tecnai F20 in ADF-STEM mode. From the tilt series, I reconstructed the 3D contact geometry between nanotubes and metal contacts using SIRT.

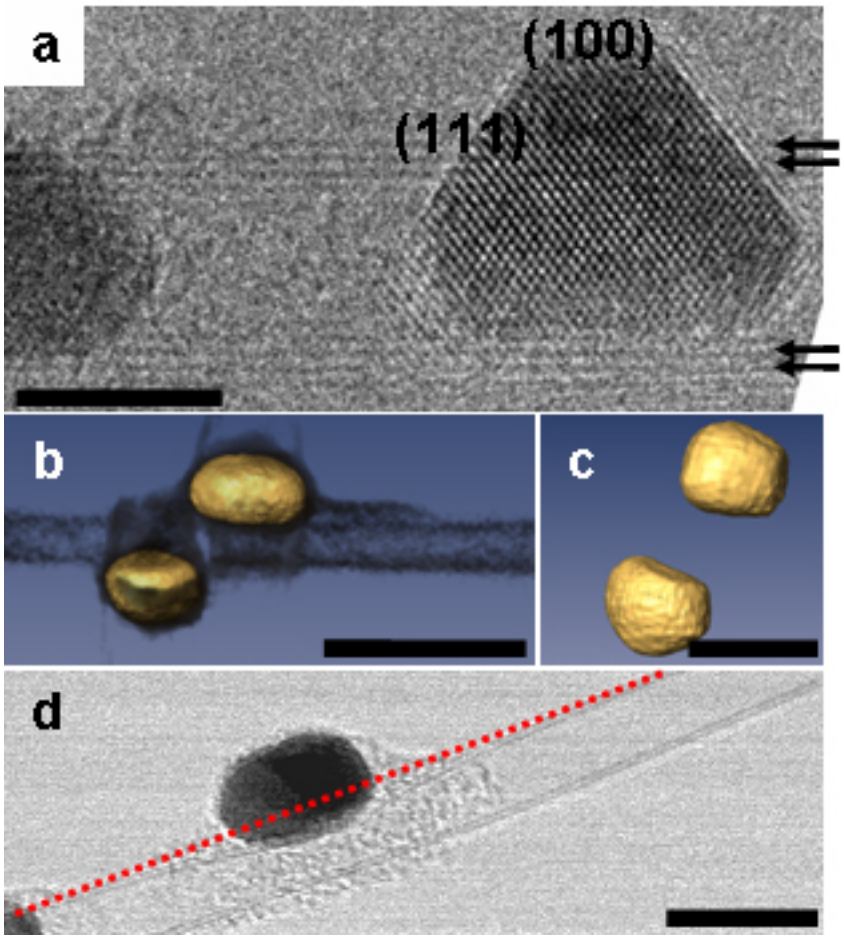

Figure 2.2: 3D images of carbon nanotubes in contact with Au islands from tomographic reconstruction. **a** Phase contrast TEM image of a Au island on a triple-walled nanotube. The side walls of the nanotube are indicated with black arrows. The atom registry of the Au island is aligned along the axial direction of the nanotube. **b** and **c** are views from a tomographically reconstructed nanotube (different from the one shown in **a**) using ADF-STEM projection images. Yellow, iso-intensity surface, and black, volume render, in **b** and **c** denote the Au and the nanotube respectively. **d** shows that a nanotube is kinked at the contact region with a Au island. The red dotted line shows how much the nanotube deviates from a straight line. A contamination layer (which appears like speckles) is also observed around the Au island. Scale bars = 5 nm in **a**; 20 nm in **b**; 10 nm in **c** and **d**.

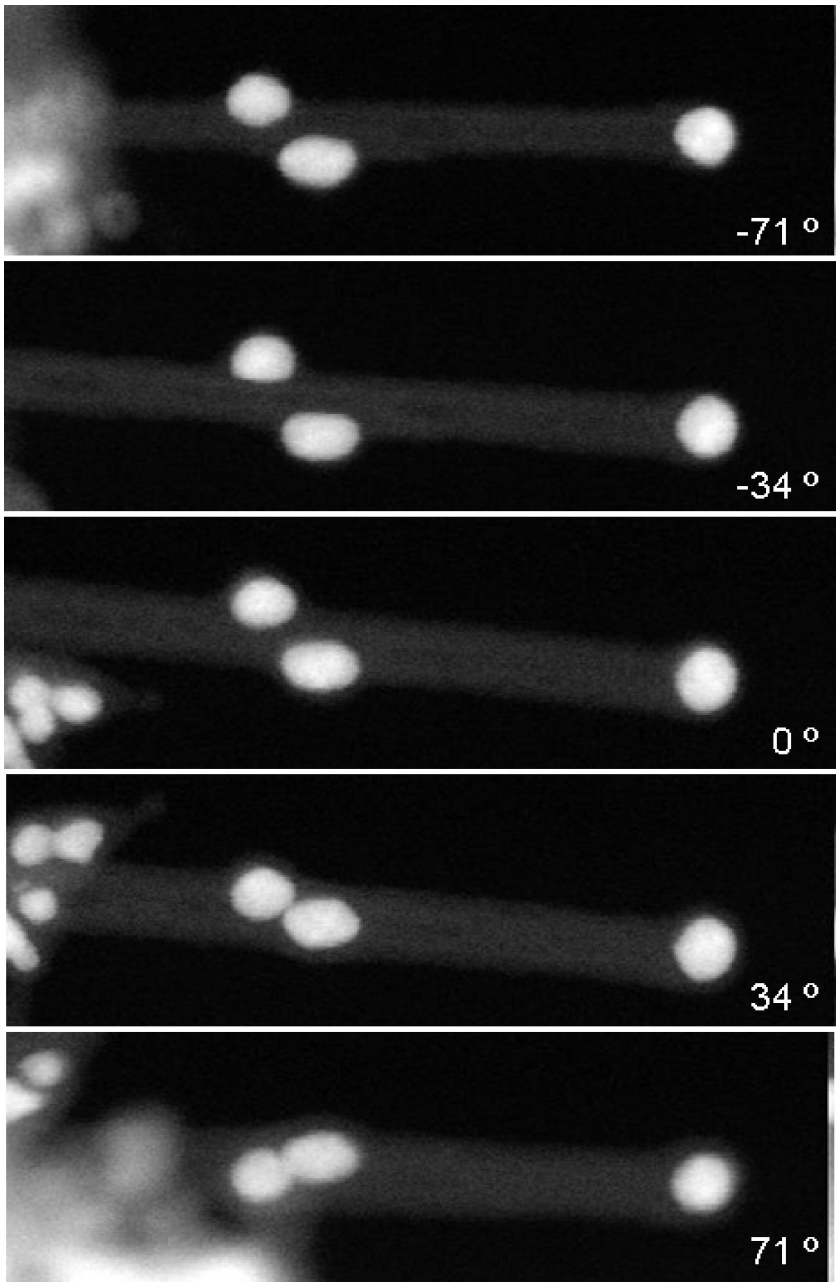

Figure 2.3: ADF-STEM tilt images of a carbon nanotube in contact with Au islands. The sample was tilted from -72 degrees to +72 degrees at a 2 degree tilt increment. Five tilt images from the tilt series are selectively shown here. The field of view (in the horizontal direction) is ~ 225 nm. The number in each panel indicates the tilt angle.

Gold-Nanotube Geometry. The geometry of the high-surface-energy Au contacts on nanotubes was examined first. For the Au contact, $\sim$ 10 Å of Au was e-beam evaporated onto the nanotube. Figure 2.2a shows, at atomic resolution, that Au forms strongly faceted islands on nanotubes. Yet, from such 2D images it is unclear how this faceting is accommodated at the curved surface of the nanotube. Hence, a tilt series of a nanotube (different from the one shown in Figure 2.2a) in contact with strongly faceted Au islands was obtained and Figure 2.3 shows five tilt images from the tilt series selectively. The nanotube was tilted ± 72 degrees at a 2 degree tilt increment. The results of the 3D tomographic study of the buried Au-nanotube interface, shown in Figures 2.2b and 2.2c, reveal what is apparently a flat contact surface. This implies that either the contact surface is very narrow with voids between the Au islands and the nanotube, or the nanotube has undergone significant radial deformation in order to accommodate the faceting of the Au contact. Upon examining the cross-sections of the nanotube carefully from the reconstruction, the latter case is confirmed. The faceting of the Au clusters and the resultant flat contact surfaces are observed universally in all reconstructed nanotubes in contact with Au, although single-walled nanotubes tend to deform more than multi-walled nanotubes. In addition, a kink along the nanotube, like the one shown in Figure 2.2d, is sometimes observed at the contact region, which is similar to nanotube deformation induced by AFM tips [42, 43].

The faceting observed in Figure 2.2c does not appear atomically sharp because the resolution of the tomographic reconstruction degrades to roughly a nanometer [70] even though the focused probe in STEM is approximately 0.2 nm in diameter due to the limited number of projection images and imperfect alignment of the tilt series. However, because the observed clusters are generally larger than a couple of nanometers, a nanometer resolution is sufficient to observe faceting.

Gold-Palladium-Nanotube Geometry. As a material commonly used as a conductive coating layer in scanning electron microscopy, an alloy of 70% Au and 30% Pd should offer improved wetting for contact. Despite this, the tomographic reconstruction shown in Figure 2.4a shows that the Au-Pd alloy also forms islands on nanotubes. But unlike the Au, no strong faceting is observed in the Au-Pd islands, whose surface looks rounded in Figure 2.4a. Nevertheless, a cross-section through the reconstruction, Figure 2.4b, reveals a relatively flat contact surface and resultant nanotube deformation. This finding is confirmed by DFT calculations of the equilibrium nanotube shape for a (20,0) carbon nanotube in contact with three atomic layers of Pd. Pd was used instead of the Au-Pd alloy to simplify the calculation, and I will shortly compare the DFT calculation to Pd experimental data. The equilibrium shape was reached by fully relaxing the nanotube and the first two Pd layers while the last Pd layer was fixed to be planar in order to replicate the flat contact surface. The cross-section view from the DFT calculation is shown in Figure 2.4c and, despite the difference in the size of the nanotubes, the overall shape of the relaxed nanotube agrees well with the experimental result, Figure 2.4b, confirming the prediction that nanotubes can deform on a flat surface [89].

It should be noted that the nanotube in Figure 2.4b is a multi-walled nanotube while the DFT calculations use a single-walled nanotube. Despite the difference in the number of walls, the essential underlying physics is the same in both the experiments and the DFT calculations, namely achieving balance between the energy needed to deform the circular cross-section of the tube and the amount of energy gained by increasing the contact area. As a result, we expect to see geometrically similar cross-sectional shapes in both cases. However, because a multi-walled nanotube would have a larger bending rigidity, in proportion to its number of walls squared [90], than a single-walled nanotube, the length scales associated with the experimental results are expected to be larger than those of the DFT calculations. In fact, the square-root of the ratio of the bending rigidity

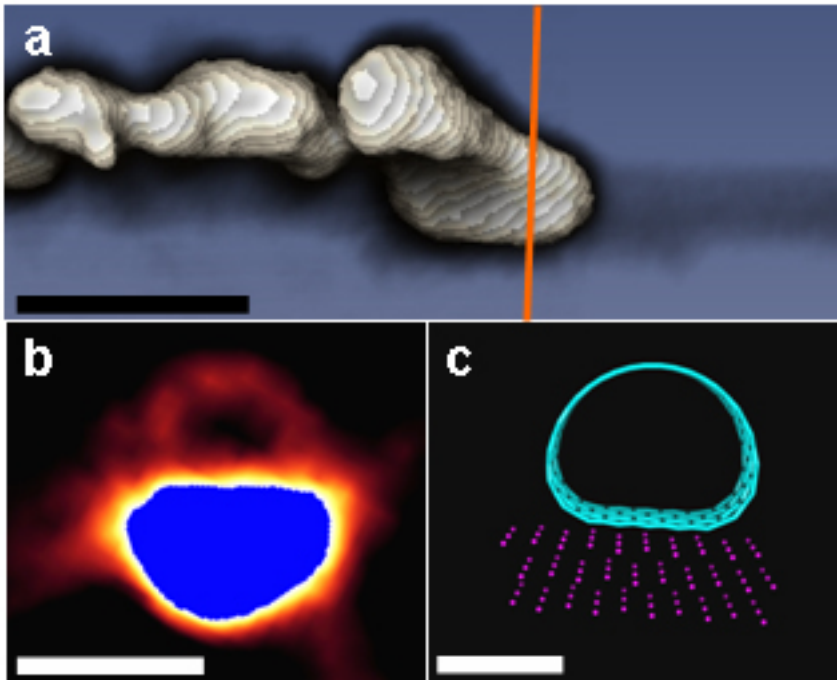

Figure 2.4: 3D images of carbon nanotubes in contact with Au-Pd islands from tomographic reconstruction. White and black in **a**, iso-intensity surface and volume render, denote the Au-Pd islands and the nanotube respectively. **b** is a cross-section view of the orange slice in **a**. From **b**, the radial deformation of the nanotube is evident. **c** is the DFT calculation of a fully relaxed (20,0) carbon nanotube (blue) on three layers of Pd atoms (pink). Scale bars = 10 nm in **a**; 4 nm in **b**; 1 nm in **c**.

to the surface energy of the contact sets the only length scale in the problem, other than the initial radius of the tube. An analytical expression which balances the deformation energy of the nanotube with the contact energy and the surface energy of the metal is discussed later.

Palladium-Nanotube Geometry. Both Au and the Au-Pd alloy form flat contact surfaces due to their islanding on nanotubes, however pure Pd has a greater tendency to wet. The tomographic reconstruction shown in Figure 2.5a reveals that Pd also forms

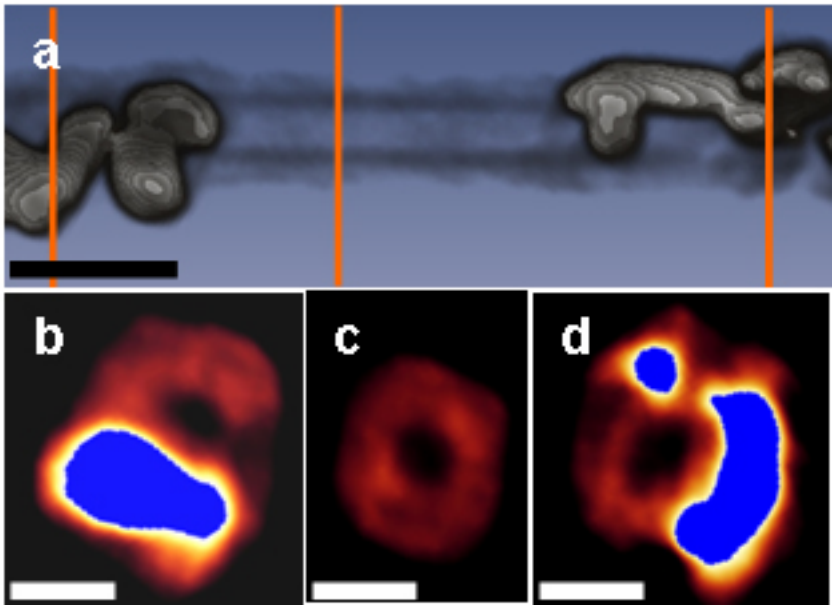

Figure 2.5: 3D images of carbon nanotubes in contact with Pd islands from tomographic reconstruction. **a**. Volume render of the tomographically reconstructed nanotube (black) with iso-intensity surface of Pd islands (white). **b, c**, and **d** are cross-section views of the orange slices in **a**. Scale bars = 10 nm in **a**; 4 nm in **b, c**, and **d**. We note that the diameter ($\sim$ 5 nm) and the wall thickness ($\sim$ 1.4 nm) of the nanotube measured from the reconstruction agree very well with those measured from the ADF-STEM images (not shown in the figure) once the lower resolution of tomographic method is taken into account.

islands on nanotubes. The observation that the shapes of the Pd islands are round with no apparent faceting suggests that the Pd may be poly-crystalline and the islands may have formed by several smaller islands coalescing together. Interestingly, the cross-section views from the reconstruction, Figure 2.5b-d, show a slightly curved contact surface. This results in, on average, less deformation of nanotubes compared to the Au and Au-Pd cases. However, we note that the degree of nanotube deformation varies widely, due to the widely varying shapes of Pd islands and their coalescence. This implies that pure Pd is still some way from perfectly wetting the nanotube.

Balancing Deformation Energy. The wide range in the degree of nanotube deformation observed in the Pd islands case suggests that the nanotube deformation may be related more to the formation of islands (and their coalescence) than to faceting. Hence if the metal wets the nanotube continuously, the deformation may not occur. The energy competition between the metal islanding and nanotube deforming can be estimated by balancing the anisotropic free-surface energy of the metal and the contact-surface energy at the interface against the deformation energy of the nanotube. By summing the energy terms, the total energy of the two extremes, a completely wetting system or an islanding system, is obtained. Although approximate, this calculation helps to identify a general wetting trend for different metals on nanotubes.

The assumed geometries for the ideal wetting and islanding systems are shown in Figure 2.6a, where the cross-sectional area of the metal (in yellow) is the same for both systems. We calculate the total energy (E_{tot}) of the two systems as a function of the contact and remaining surface area, S_c and S_s respectively, as:

$$E_{tot} = \frac{2\pi^2 DL}{\pi R - a} + (u_{fc} - u_{bc})\sigma S_c + u_{fs}\sigma S_s \tag{2.1}$$

where D is the effective bending stiffness of the nanotube [91], L is the length of the deformed region of the nanotube, R is the radius of the nanotube, σ is the number density of the metal per unit area, u_{fc} is the free-surface energy of the contact surface per atom, u_{fs} is the free-surface energy of the remaining surface per atom, and u_{bc} is the binding energy of the metal to the nanotube per atom. The energy unit for E_{tot} is eV. Note that as the cross-sectional area is conserved, the volume energy of the metal is identical for both systems per given metal and thus cancels out. The first term in Equation (2.1) is the deformation energy of the nanotube based on an elastic theory, assuming only the radial deformation [29, 30, 91]. A detailed derivation of Equation (2.1) is provided in Appendix A.

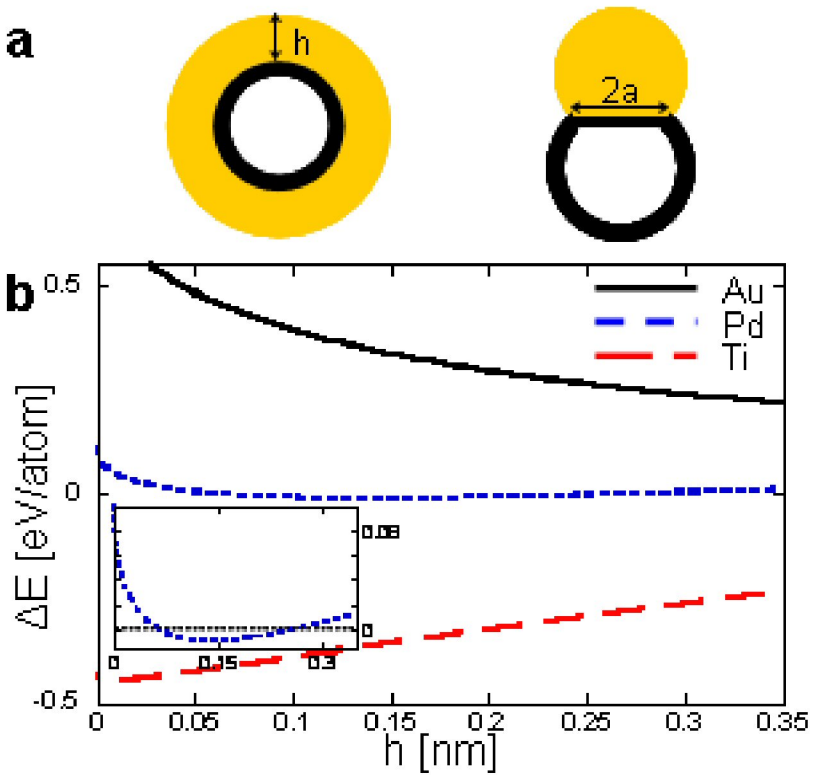

Figure 2.6: Balancing energies among the deformation energy of a carbon nanotube, the surface energy of a metal, and the contact energy between the nanotube and the metal. **a** shows a schematic diagram of a wetting and islanding metal (yellow) on a nanotube (black). **b** shows a plot of energy difference of the two ideal systems per atom, (E_{tot}(wet)-E_{tot}(island))/N_{tot}, for Au (black, solid line), Pd (blue, short-dotted line) and Ti (red, long-dotted line) with a nanotube of radius 1 nm. The inset shows only the Pd case.

We used Equation (2.1) to calculate E_{tot} for the two ideal systems for each metal contact and obtained the energy difference per atom, $\Delta E = (E_{tot}(\text{wet})-E_{tot}(\text{island}))/N_{tot}$ where N_{tot} is the total number of surface atoms for a given metal contact. If ΔE is negative, then the metal would wet nanotubes rather than form islands because E_{tot}(wet) is smaller than E_{tot}(island). Shown in Figure 2.6b are plots of δE, with an increasing thickness of deposited Au, Pd, and Ti for a single-walled nanotube with radius of 1 nm. From Figure 2.6b, Au would always island while Ti would always wet. Palladium lies between the two systems. ΔE for Pd crosses zero and remains close to zero for a wide range of nanotube diameters, which indicates partial wetting. Experimentally, the curved contact surface as shown in Figure 2.5**d** may suggest that Pd partially wets nanotubes.

From the inset in Figure 2.6**b** which shows ΔE for Pd, the predicted thickness of the wetting layer for Pd is about a monolayer. Furthermore, the values of h (the thickness of the wetting layer) for Au, Pd, and Ti cases in Figure 2.6**b** suggest that only a few atomic layers are deposited onto the nanotube with radius of 1 nm in the complete wetting case (this is because of the constraint that the cross-sectional area of the wetting contact is set equal to that of the islanding contact whose base width, a, cannot be larger than the radius of the nanotube). At atomic scale, the simple energy-balance argument using bulk properties of the metals cannot accurately model the system; hence ab initio calculations are required to accurately predict the thickness of the wetting layer for Pd and to fully describe the system when the wetting contact is only a few atomic-layer thick. Figure 2.7 shows plots of ΔE for a single-walled nanotube with radius of 3 nm. In this case, the maximum value for h is 1.1 nm, which is in the range suitable for a simple energy-balance argument. Figure 2.7 also shows that Au would always island while Ti would always wet.

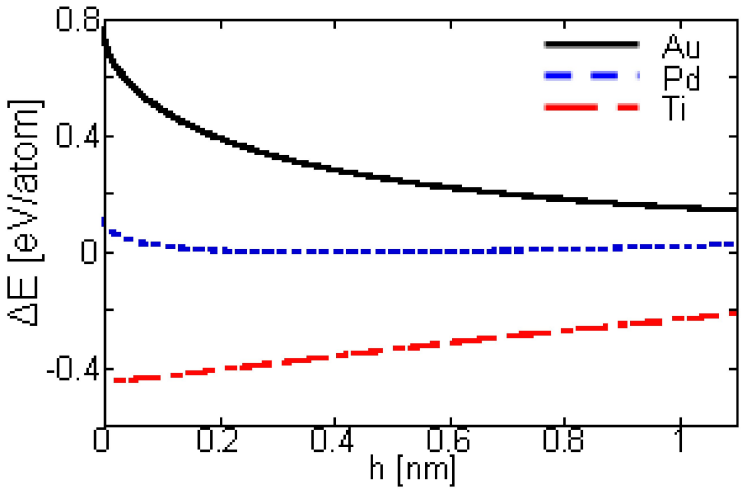

Figure 2.7: Balancing energies among the deformation energy of a carbon nanotube, the surface energy of a metal, and the contact energy between the nanotube and the metal for a nanotube with radius 3 nm. **a** shows a schematic diagram of a wetting and islanding metal (yellow) on a nanotube (black). **b** shows a plot of energy difference of the two ideal systems per atom, (E_{tot}(wet)-E_{tot}(island))/N_{tot}, for Au (black, solid line), Pd (blue, short-dotted line) and Ti (red, long-dotted line) with a nanotube of radius 3 nm.

It is worth noting that both the simple, analytic estimates of the nanotube deformation energy [91] and the DFT calculations [68] suggest that the energy cost to deform a nanotube is negligible [89] until the radius of curvature falls below a few angstroms. For all but the smallest nanotubes (which will not deform), Equation (2.1) suggests that it is largely the binding energy of the metal to the nanotube (with respect to the free-surface energy of the metal) that governs the wettability of the metal to the nanotube. According to DFT calculations within the generalized gradient approximation [92], of the three metals under study, Ti has the highest binding energy to the nanotube, 2.9 eV/atom, while Au has the lowest, 0.6 eV/atom. Hence creating a large contact surface by wetting lowers the total energy of the system significantly for Ti but not appreciably

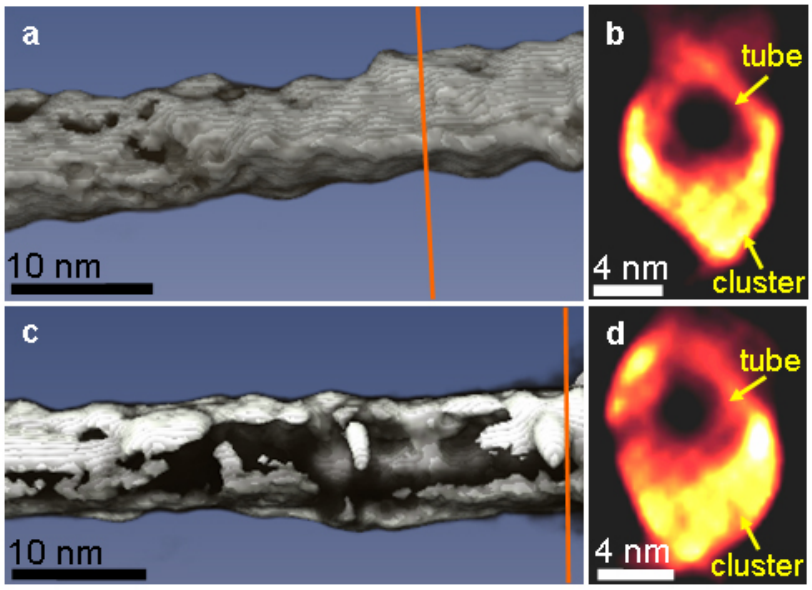

Figure 2.8: 3D images of carbon nanotubes in contact with Ti from tomographic reconstruction. **a** and **c** show a volume render of carbon nanotubes (black) with iso-intensity surface of Ti wetting layers (white). A little intensity of black exists outside of the Ti wetting layers, which indicates a thin contamination layer. **b** and **d** show cross-section views of the orange slices in **a** and **c**. Scale bars = 10 nm in **a, c** ; 4 nm in **b, d**.

for Au. The binding energy of Pd is 1.7 eV/atom [92], which is fairly high. But the free-surface energy of Pd, which the same type of calculation gives to be approximately 1.0 eV/atom [93], prevents Pd from making a large free surface. Therefore, complete wetting does not occur for Pd even though the binding energy is high.

Mobility of surface atoms in metals can also play a role in determining whether the contact metal will island (and facet) on the nanotubes or wet the nanotubes. If the surface atoms are mobile, that is if the energy cost of atomic rearrangements on surfaces is small, then the free energy of the metal-nanotube system can be lowered by creating metal surfaces whose free-surface energy is small. This will result in faceted metal islands on nanotubes, rather than a wetting layer on nanotubes. Because the atomic

surface mobility is related to the melting point, the melting temperature of metals can be another useful parameter. The melting temperature of Au, Pd, and Ti are 1337 K, 1828 K, and 1941 K respectively, suggesting that Au would create faceted islands on nanotubes while the degree of faceting for Pd and Ti would not be as strong as Au. Experimentally, we observe that Au islands facet strongly while Pd islands appear more rounded.

Titanium-Nanotube Geometry. Because Equation (2.1) predicts wetting for Ti contacts, Ti is studied here as an example of a material with good wetting characteristics despite the high Schottky barrier between Ti and a nanotube, which leads to a bad electrical contact. The tomographic reconstruction, Figure 2.8, shows that Ti covers the nanotube uniformly, strongly indicating complete wetting. Cross-section views, Figure 2.8**b** and 2.8**d**, reveal that Ti wraps around the nanotube, which preserves the round shape of the nanotube. The wetting by Ti is observed universally regardless of the nanotube size.

2.5 Results and Discussions II - Modified Electronic Properties of Deformed Nanotubes Using EELS

The structural deformation of carbon nanotubes by the islanding metals such as Au and Au-Pd suggests that the electronic properties of the deformed carbon nanotubes must also change because the electronic property of the carbon nanotubes is determined uniquely by the structure of the nanotubes such as the chirality and the diameter of the tubes [32, 35]. Electron energy-loss spectroscopy (EELS) was used to probe the electronic properties of the deformed nanotubes, as EELS probes the local unoccupied electronic density of states [94–96]. In particular, I investigated the carbon (C) K edge

closely for a hint of electronic changes in the nanotubes upon deformation. C-K EELS spectra taken from the deformed regions of the nanotube were compared with similar spectra taken from the regions of the same nanotube without metal clusters (hence, without deformation). Nanotubes with Au and Au-Pd contacts, which islanded on nanotubes, were examined.

Figure 2.9 shows C-K EELS edges of nanotubes in contact with Au islands. Although ADF-STEM images are obtained when EELS is acquired, bright-field STEM images are shown in Figure 2.9 because the number of walls in carbon nanotubes is shown more clearly in bright-field images. The spectra from the un-deformed regions of the nanotubes (in blue) have a sharp π^* peak and a clear σ^* peak. In contrast, the spectra from the regions of the nanotubes where the Au islands have deformed the tubes (in red) show a broadened π^* and σ^* peak. I also observe that the intensity between the π^* and σ^* peak increases. The broadened peaks and the increased intensity between the π^* and σ^* peak indicate that the s-p hybridized orbitals of the nanotubes are overlapping with each other due to the radial deformation of the nanotubes, which brings the orbitals closer to each other than before. The overlap of the s-p orbitals suggests a modified electronic structure of the nanotubes, deformed by Au islands.

From the tomographic results, the nanotubes in contact with Au-Pd islands deform similarly to the nanotubes in contact with Au islands. Hence, the C-K EELS spectra from the nanotubes in contact with Au-Pd islands should also show similar changes in the shape of the EELS fine structure to those in the Au islands case. Figure 2.10 shows C-K EELS edges of nanotubes in contact with Au-Pd islands. As in the Au islands case, a broadened π^* and σ^* peak and an increased intensity between the π^* and the σ^* peak are observed, which suggests a possible change in the electronic structure of the nanotube due to deformation by the Au-Pd islands.

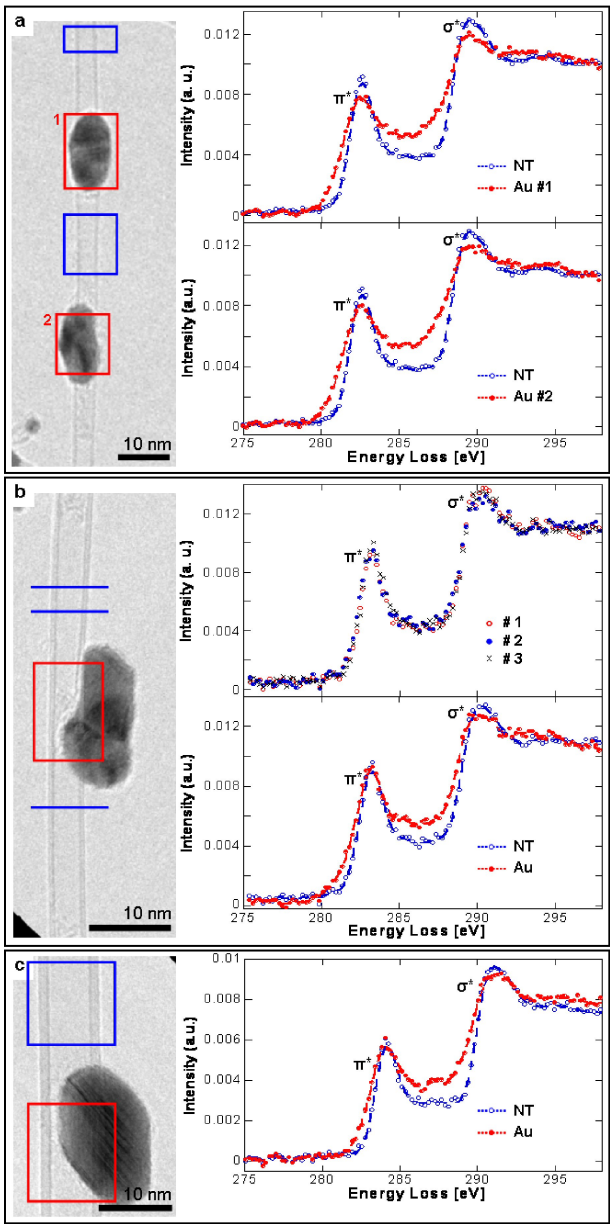

Figure 2.9: Carbon-K EELS edges from carbon nanotubes deformed by Au contacts. The insets are bright-field STEM images. Boxes and lines in the insets indicate the regions in which EELS was acquired in area- and line-mode respectively. Spectra in blue are taken from the undeformed regions of the nanotubes while spectra in red are taken from the deformed regions of the nanotubes.

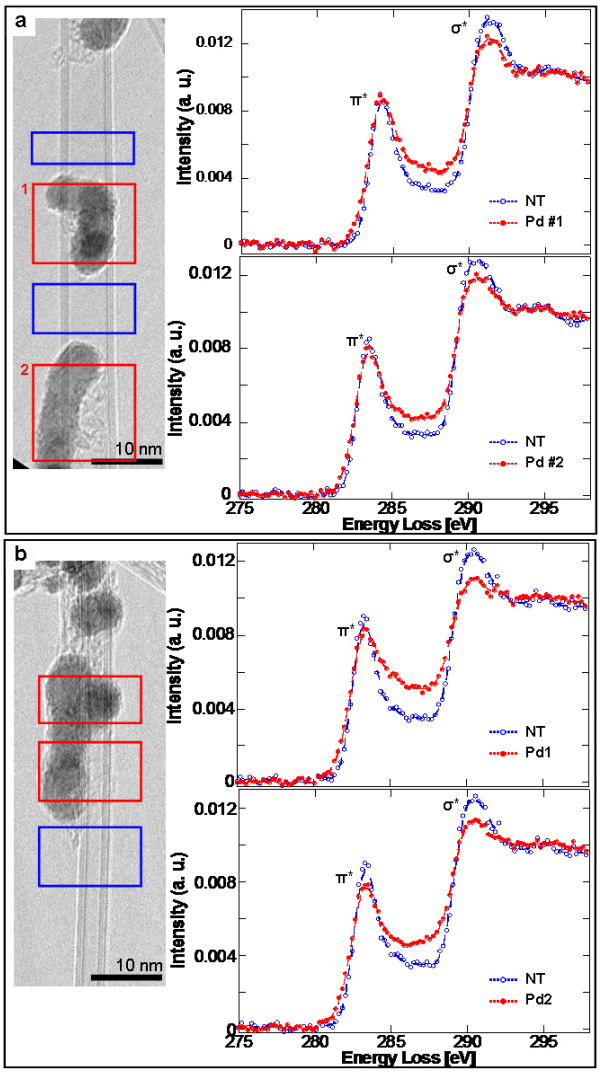

Figure 2.10: Carbon-K EELS edges from carbon nanotubes deformed by Au-Pd contacts. The insets are bright-field STEM images which show the nanotube sidewalls very clearly. Boxes and lines in the insets indicate that EELS was acquired in area- and line-mode respectively. Spectra in blue are taken from the un-deformed regions of the nanotubes while spectra in red are taken from the deformed regions of the naotubes.

The observed changes in the C-K EELS edge obtained from the deformed regions of the nanotubes suggests a modified electronic structure of the nanotubes due to deformation. However, it should be noted that the EELS results do not provide conclusive evidence for a modified electronic structure of the nanotubes because an amorphous carbon layer such as a contamination layer surrounding nanotubes can also yield similar apparent changes in the C-K EELS edge. This is because the C-K EELS edge of the amorphous carbon has a broad π^* peak and increased intensity between the π^* and σ^* peak (a reference spectrum of amorphous carbon can be found in Sandre *et al*. paper [96]). For nanotubes in contact with Au and Au-Pd islands, contamination issues were minor. However, nanotubes in contact with wetting Ti often were surrounded by a noticeable contamination layer, making accurate comparisons of EELS spectra between un-deformed and deformed regions of the nanotubes difficult. Therefore, further experiments such as transport measurements of nanotube transistors with different contact metals are necessary for a definitive experimental proof that deforming nanotubes leads to a change in the band structure.

2.6 Conclusion

The contact geometry bewteen nanotubes and various metal contacts was reconstructed in 3D using electron tomography, which showed that islanding contacts radially deformed carbon nanotubes. As both theoretical calculations and experimental observations show band gap changes due to mechanical nanotube deformation by AFM tips [42–44, 97, 98], the observed deformations by the poorly-wetting contacts imply that the electronic structure of the nanotube may change significantly upon attaching an electrical contact to it. Therefore, in addition to a Schottky barrier at the contact, a geometrically-induced scattering term can also be expected, increasing the contact re-

sistance. EELS was used to infer possible changes in the electronic structure of the nanotubes due to deformation. Hence, promising contact metals for nanotube devices must have good wettability to nanotubes as well as a small Schottky barrier. The popular contact metal, Pd, comes close to satisfying this condition and we anticipate that alloys of Pd, which possess a lower free-surface energy than pure Pd, may provide improved contacts both physically and electrically.

CHAPTER 3

SPATIALLY RESOLVED ELECTRON ENERGY-LOSS SPECTROSCOPY OF ELECTRON-BEAM GROWN AND RADIO FREQUENCY SPUTTERED CoFeB/MgO/CoFeB MAGNETIC TUNNEL JUNCTIONS

In this chapter, I will describe the first part of the MgO-based magnetic tunnel junction (MTJ) work, where I focused on the structural and chemical characterization of the CoFeB/MgO/CoFeB sandwich layer. EELS at sub-nanometer resolution was used to investigate the CoFeB/MgO/CoFeB structures grown by electron-beam (e-beam) evaporation and radio frequency (rf)-sputtering before and after annealing at 375 ° C. Gap states were observed in the MgO layer for both growth methods, although the rf-sputtered MgO layer showed significantly higher densities of gap states. Asymmetry in oxygen bonding between the top and bottom CoFeB/MgO interfaces was also observed for both growth methods. Surprisingly, a significant amount of B as BO_x was observed in the rf-sputtered MgO layer, but not in the e-beam evaporated MgO layer. This is due to the oxidation of the bottom electrode during the rf-sputtering of MgO, which results in the formation of BO_x. BO_x remains in the rf-sputtered MgO layer even after annealing. An insertion of a Mg under-layer between the rf-sputtered MgO layer and the bottom electrode greatly reduced the amount of BO_x in the barrier layer upon annealing.

3.1 Introduction

Magnetic tunnel junctions (MTJs) that use MgO as a tunnel barrier have attracted great interest as memory devices, especially in magnetic random access memory (MRAM) technology, due to the prediction of a high tunneling magnetoresistance (TMR) for epitaxially grown Fe/MgO/Fe MTJs [50, 51]. On-going studies of both epitaxially grown [52] and sputtered [53] MgO-based MTJs have led to steady improvement in TMR, up to

472% at room temperature in a recent demonstration where CoFeB was used as a electrode material and the MTJs were annealed subsequently [99]. Yet, our understanding of what affects the TMR at an atomic level remains incomplete. For example, annealing the MTJs up to a certain moderate temperature has been experimentally shown to increase the TMR substantially [99, 100]. A proposed explanation is that annealing creates lattice-matched, sharp interfaces by crystallizing the electrodes at the interfaces, which subsequently enhances the TMR due to coherent tunneling [53, 101, 102]. Conversely, annealing can promote undesirable diffusion of atoms in the MTJs [99], which may worsen the tunneling properties of the barrier layer due to additional scattering terms introduced by the incorporation of foreign species in the barrier. Therefore, investigating the effects of annealing and of different growth methods on the MgO-based MTJs at an atomic level is crucial to understanding how local chemical and structural changes affect TMR. Here, STEM and EELS with sub-nanometer resolution were used to examine the MgO-based MTJs grown by the two most common deposition methods, e-beam evaporation and rf-sputtering.

3.2 Methods

Film Growth (J. C. Read and R. A. Buhrman). Electron-beam evaporation and rf-sputtering were used to grow 200 Å CoFeB / 20 Å MgO (or 5 Å Mg / 5 Å MgO) / 200 Å CoFeB MTJ structures on thermally oxidized Si(100) substrates at a base pressure of $\sim 2 \times 10^{-9}$ Torr [103]. The structures were studied as-grown as well as after a one-hour anneal at 375 °C in a separate vacuum chamber. The investigated structures are not fully-formed, working MTJ devices which require additional layers such as a pinning layer (IrMn) for a bottom electrode and a capping layer (Ta/Ru). Still, they contain the essential ferromagnetic electrode / barrier / ferromagnetic electrode sandwich layers,

which are sufficient for studying the local chemical profiles in the MgO layer and at the MgO/CoFeB interfaces.

STEM Sample Preparation. The MTJ structures were mechanically polished in a wedge geometry [104] and ion-milled at low voltages (3 kV followed by 1 kV) for STEM and EELS experiments. The wedge geometry allows us to determine the effects of surface oxidations, which become a smaller, and ultimately negligible fraction of the total EELS signal as the projected thickness of the wedge sample increases, provided that the sample is transferred quickly from the ion-mill to the microscope.

Electron Energy-loss Spectroscopy Studies. For EELS studies, a 200 kV FEI Tecnai F20-ST STEM fitted with a monochromator and a Gatan imaging filter 865-ER was used. The electron beam was focused to form a $\sim$ 2 Å diameter probe with a convergence semi-angle of $\sim$ 9.6 mrad. To reduce the electron dose per unit area for minimum radiation damage of MgO-based MTJs, EELS spectra were taken in lines parallel to the MgO/CoFeB interfaces. The spectrometer dispersion was set to 0.3 eV/channel to capture the wide energy range needed to record all edges simultaneously, resulting in an energy resolution of 1 eV.

3.3 Results and Discussion

Figures 3.1 and 3.2 show TEM images of the e-beam grown and the rf-sputtered CoFeB / 20 Å MgO / CoFeB structures (MgO[eb] and MgO[rf] respectively) and the rf-sputtered CoFeB / 5 Å Mg / 5 Å MgO / CoFeB structure (Mg/MgO[rf]) before and after annealing at 375 °C. In the as-grown case, the MgO[eb] junction shows the most straight interfaces. Also, grains showing crystallinity are observed in both the MgO[eb] and the MgO[rf] layer. After annealing, the MgO[eb] layer again shows the most uniform crys-

tallinity with sharp interfaces while the MgO[rf] layer contains many grain boundaries and rough interfaces. Lattice fringes are absent in the Mg / MgO[rf] bi-layer before and after annealing, which implies that the layer is amorphous in both cases. Comparison between Figure 3.1b and Figure 3.2b shows that annealing improves the crystallinity of the MgO[rf] layer although the MgO[rf] layer remains poly-crystalline with many grain boundaries even after annealing.

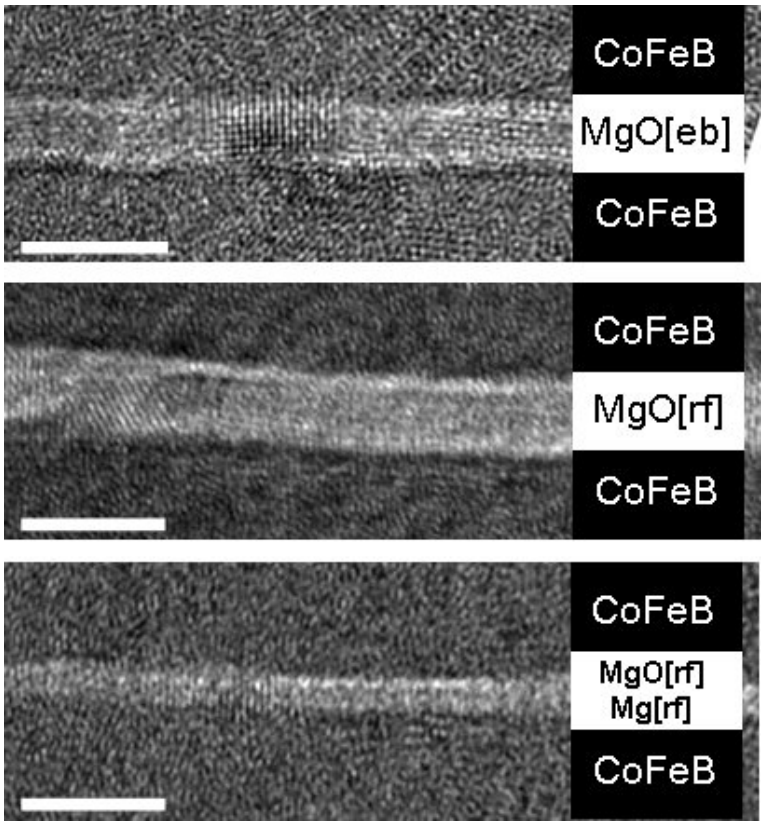

Figure 3.1: TEM images of the as-grown CoFeB/MgO/CoFeB MTJs by e-beam evaporation and rf-sputtering. **a**. E-beam grown 20 Å MgO, **b**. Rf-sputtered 20 Å MgO, and **c**. Rf-sputtered 5 Å Mg / 5 Å MgO barrier layer. Scale bars are 5 nm long in all panels.

The TEM observation that the MgO[eb] layer is the most crystalline of the three growth methods is further supported by examining the O-K EELS edge, which provides

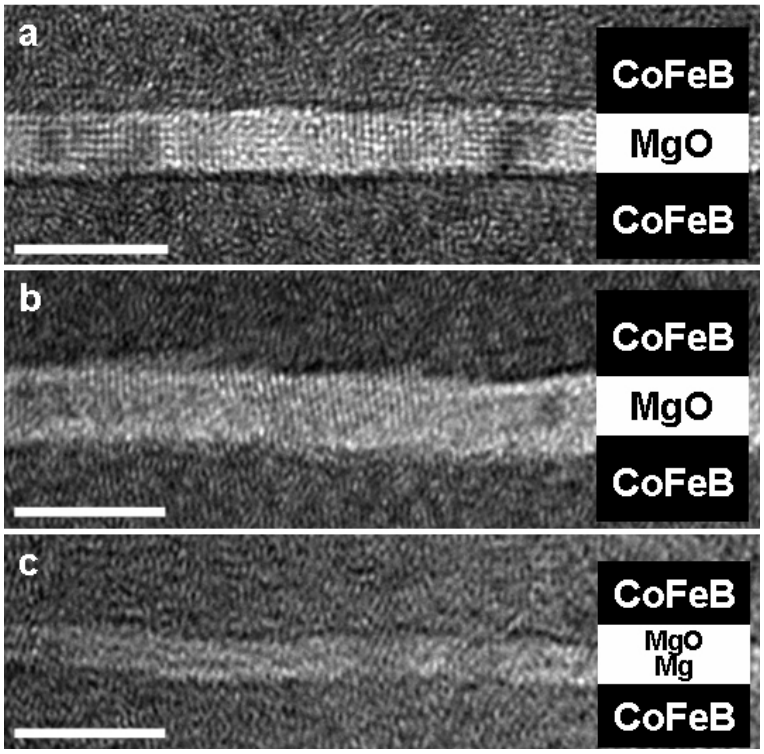

Figure 3.2: TEM images of the annealed CoFeB/MgO/CoFeB MTJs by e-beam evaporation and rf-sputtering. **a**. E-beam-grown CoFeB / 20 Å MgO / CoFeB, **b**. Rf-sputtered CoFeB / 20 Å MgO / CoFeB and **c**. Rf-sputtered CoFeB / 5 Å Mg / 5 Å MgO / CoFeB MTJ structure. Scale bars are 5 nm long in all panels.

information on the chemical ordering of the MgO layer by its fine structure [105]. Figure 3.3 shows the O-K EELS edge of the three barrier layers, MgO[eb], MgO[rf], and Mg/MgO[rf], before and after annealing. The spectra were acquired from the center of the barrier layer to minimize contributions from the top and bottom interfaces. Also, the spectra were acquired in a line mode, where the electron beam was continuously rastered along a line parallel to the interface, to minimize radiation damage of the MgO layers. The spectra in black, shown in all panels in Figure 3.3, are a reference O-K EELS spectrum obtained from a bulk MgO crystal. In agreement with the TEM images, O-K edge data show that the MgO[eb] barrier is most ordered structurally because the

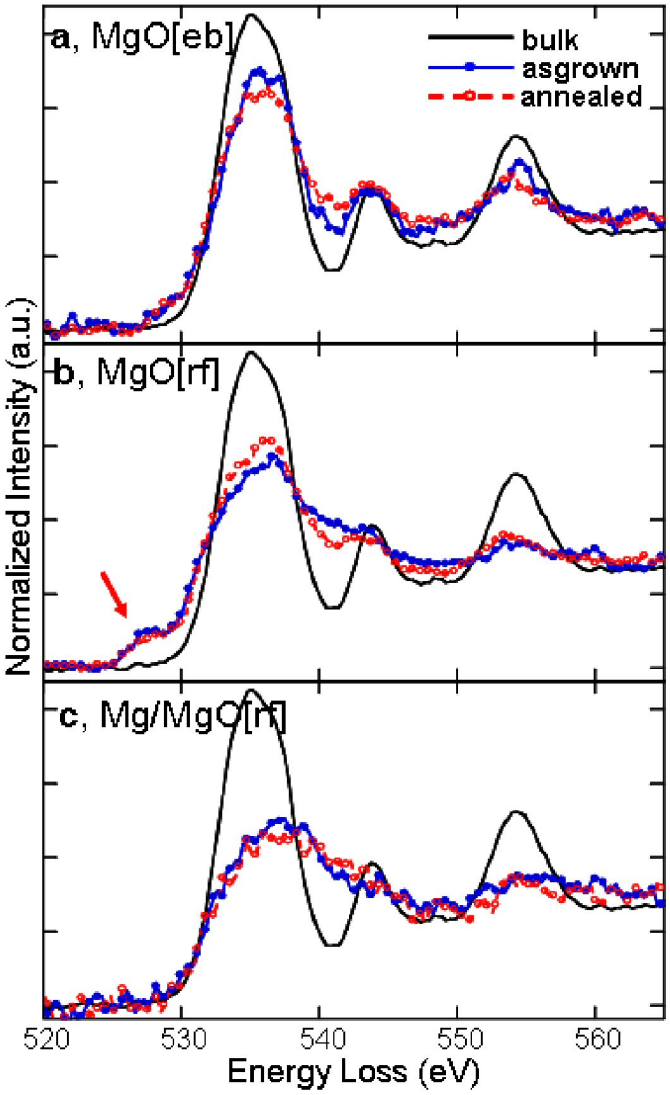

Figure 3.3: Oxygen-K EELS edge of CoFeB/MgO/CoFeB MTJs before and after annealing. O-K of (**a**) CoFeB / 20 Å MgO[eb] / CoFeB, (**b**) CoFeB / 20 Å MgO[rf] / CoFeB and (**c**) CoFeB / 5 Å Mg / 5 Å MgO [rf] / CoFeB MTJ structure. The spectra in black are a reference O-K spectrum from bulk MgO. The spectra in blue are taken from the as-grown samples while the spectra in red are taken from the annealed samples. The arrow in (**b**) indicates gap states in the MgO[rf] layer due to disorder.

spectrum from the MgO[eb] barrier (Figure 3.3a) most closely follows that of the bulk MgO, with three distinct peaks in the fine structure.

The fine structure of the O-K EELS edge provides information on the unoccupied O p-orbital density of states and the local chemical environment surrounding O atoms [105, 106]. Damping of the EELS extended fine structure is indicative of disorder or fewer surrounding O atoms [105, 106]. Therefore, Figure 3.3b indicates that the MgO[rf] layer must contain structural or chemical defects because the second and third peaks in the O-K edge are damped significantly compared to the reference spectrum of bulk MgO. The as-grown MgO[rf] layer is less ordered than the as-grown MgO[eb] layer structurally as evident by the damping of the second peak at $\sim$ 543 eV observed in the O-K edge of the MgO[rf] layer. But after annealing, the O-K edge of the annealed MgO[rf] layer sharpens to follow that of the annealed MgO[eb] layer more closely, which indicates improved structural ordering upon annealing in the MgO[rf] layer (Figure 3.5a shows this more clearly). For the Mg/MgO[rf] bi-layer (Figure 3.3c), the O-K edge has no resemblance to the bulk MgO O-K edge, which suggests that the bi-layer has lost the characteristics of bulk MgO completely. Interestingly, the O-K edges of all the MgO layers are far from that of the bulk MgO even after annealing, suggesting that the 20 Å MgO layers do not exhibit the same characteristics as the bulk MgO.

Figure 3.4 shows the Mg-K EELS edge of the three barriers. The fine structure of the Mg-K edges obtained from the MgO[eb] and MgO[rf] layers follows that of the Mg-K edge obtained from the bulk MgO, which indicates that both layers contain MgO characteristics. However, in the fine structure of the Mg-K edge obtained from the Mg/MgO[rf] bi-layer, the split in the first peak at $\sim$ 1320 eV is lost and the second peak at $\sim$ 1335 eV is suppressed compared to the bulk MgO Mg-K edge, confirming that the Mg/MgO[rf] bi-layer indeed does not resemble bulk MgO at all. The EELS

findings in the Mg/MgO[rf] layer are consistent with the TEM result, which shows that the Mg/MgO[rf] bi-layer remains amorphous even after annealing.

A noticeable EELS signal is observed starting at 525 eV in the O-K pre-edge of the MgO[rf] layer (arrows in Figure 3.3b), which indicates the presence of gap states in the MgO[rf] layer. Additionally, more gap states are observed at the interfaces than in the center of the MgO[rf] layer. Because EELS reflects the unoccupied density of states of a conduction band modified by a core hole effect [105–108], the appearance of the gap states can reflect band tailing in the conduction band of the MgO[rf] layer. Using a scanning tunneling microscope, P. G. Mather et al. [109] observed significant conduction band tailing in the MgO/Fe structure, which was attributed to vacancies [110] and other structural defects.

Figure 3.5a shows the O-K edges of the bulk MgO (dotted black), the MgO[eb] layer (red), the MgO[rf] layer (blue), and the Mg/MgO[rf] bi-layer (solid black) after annealing in one panel for comparison. Figure 3.5b and 3.5c show the O-K edges taken from the top and bottom CoFeB/MgO interfaces of the annealed MgO[eb] and MgO[rf] MTJ structures respectively. Interestingly, the top and bottom interfaces exhibit distinctly different O-K EELS spectra. For the MgO[eb] structure, the top interface shows more disorder in the O-K edge than the bottom interface and hence is less MgO-like than the bottom interface. This asymmetry in the O-K edge could be due to the previously reported chemisorbed O species on the top surface of the MgO[eb] layer [109, 111]. Another possibility is the partial intermixing of the MgO[eb] layer with the top electrode which was deposited using dc magnetron sputtering [103]. Both effects would roughen the top interface, resulting in a more damped O-K spectrum at the top interface compared to the bottom interface. For the MgO[rf] structure, the bottom interface shows more disorder than the top interface and hence is less MgO-like than the top interface.

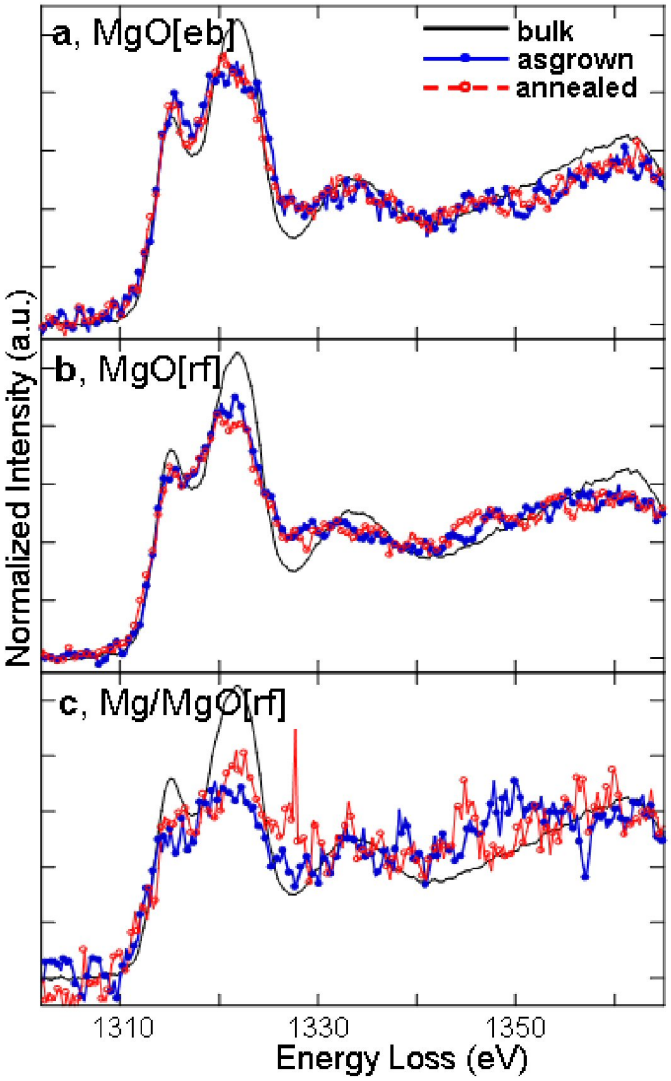

Figure 3.4: Mg-K EELS edge of CoFeB/MgO/CoFeB MTJs before and after annealing. Mg-K of (**a**) CoFeB / 20 Å MgO[eb] / CoFeB, (**b**) CoFeB / 20 Å MgO[rf] / CoFeB and (**c**) CoFeB / 5 Å Mg / 5 Å MgO[rf] / CoFeB MTJ structure. The spectra in black are a reference Mg-K spectrum from bulk MgO. The spectra in blue are taken from the as-grown samples while the spectra in red are taken from the annealed samples.

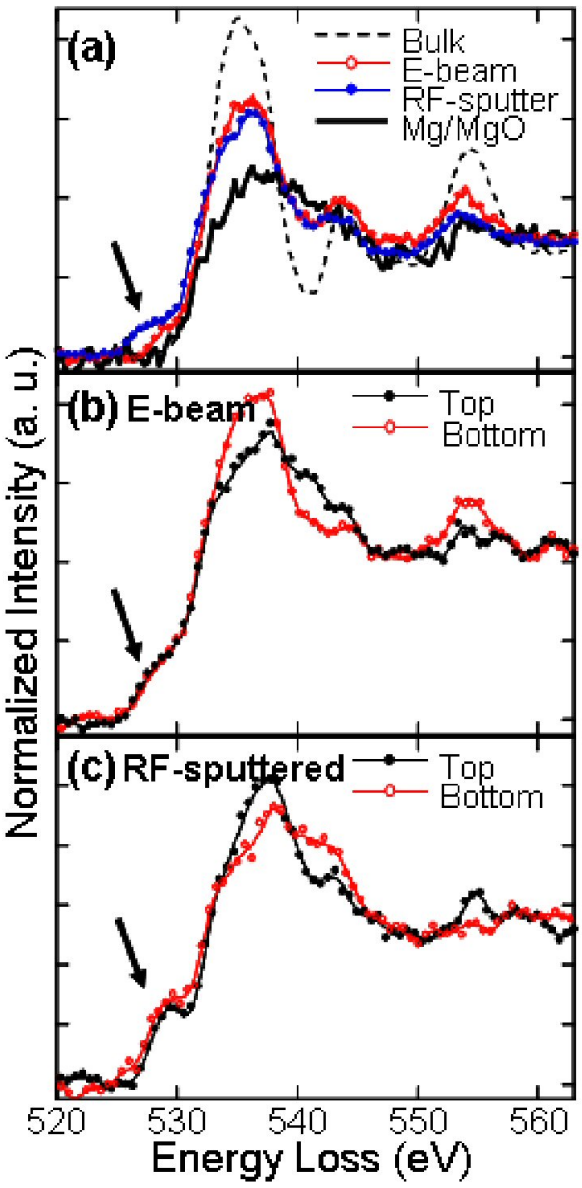

Figure 3.5: O-K EELS edge of CoFeB/MgO/CoFeB MTJs showing assymetry in top and bottom MgO/CoFeB interfaces after annealing. **a** O-K edge of bulk MgO, CoFeB / 20 Å MgO[eb] / CoFeB, CoFeB / 20 Å MgO[rf] / CoFeB, and CoFeB / 5 Å Mg / 5 Å MgO[rf] / CoFeB MTJ structure after annealing. The spectra are normalized. **b** O-K edge of MgO[eb] MTJ structure taken from the top and bottom interfaces. **c** O-K edge of MgO[rf] MTJ structure taken from the top and bottom interfaces. Arrows indicate gap states.

This disorder is from the oxidation of the bottom electrode by O ions released during the rf-sputtering of MgO [103, 112]. Again similar to the case of the MgO[eb] top interface, some disorders are expected in the top interface of the MgO[rf] structure due to chemisorbed O species or the partial intermixing during sputtering of the top electrode. However, the effect of the oxidation of the bottom electrode is more significant than the effect of chemisorbed O species or the partial intermixing at the top interface in the MgO[rf] structure. As mentioned earlier, the arrows in all panels of Figure 3.5 indicate the gap states in the MgO layer due to vacancies and other structural defects.

I investigated the B-K, Fe-$L_{2,3}$, and Co-$L_{2,3}$ EELS edges to study possible diffusion of atomic species across the MgO/CoFeB interfaces as a function of a growth method and annealing. Significant changes in the fine structure of the Co or Fe edges were not detected, which suggests that their chemical intermixing with the MgO is small. If Co or Fe were to intermix with the MgO layer, they would be oxidized and the fine structure of Fe and Co EELS edges should change. Surprisingly, the B-K edge showed a dramatic change across the MgO layer. Figure 3.6 shows the B-K edges acquired from the bottom electrode and the center of the MgO layer of the three structures before and after annealing. The MgO[eb] layer exhibits a low B-K signal (Figure 3.6a and b) before and after annealing, which indicates only a trace amount of B diffused from the electrode into the MgO[eb] layer. For the as-grown MgO[rf] layer (Figure 3.6c), a significant B-K signal is observed, which suggests considerable B diffusion into the MgO layer from the bottom electrode, which agrees with previous XPS studies [103]. Moreover, the observed B-K edge displays a strong π^* peak at 193 eV that is characteristic of oxidized B (BO_x) in trigonal coordination with O atoms [113]. This is in contrast to the metallic B in the electrode (in black in Figure 3.6). Most of the BO_x remains in the barrier after annealing (Figure 3.6d), suggesting that mixing of BO_x into the MgO layer is thermodynamically stable. The formation of BO_x is due to the inevitable oxidation of

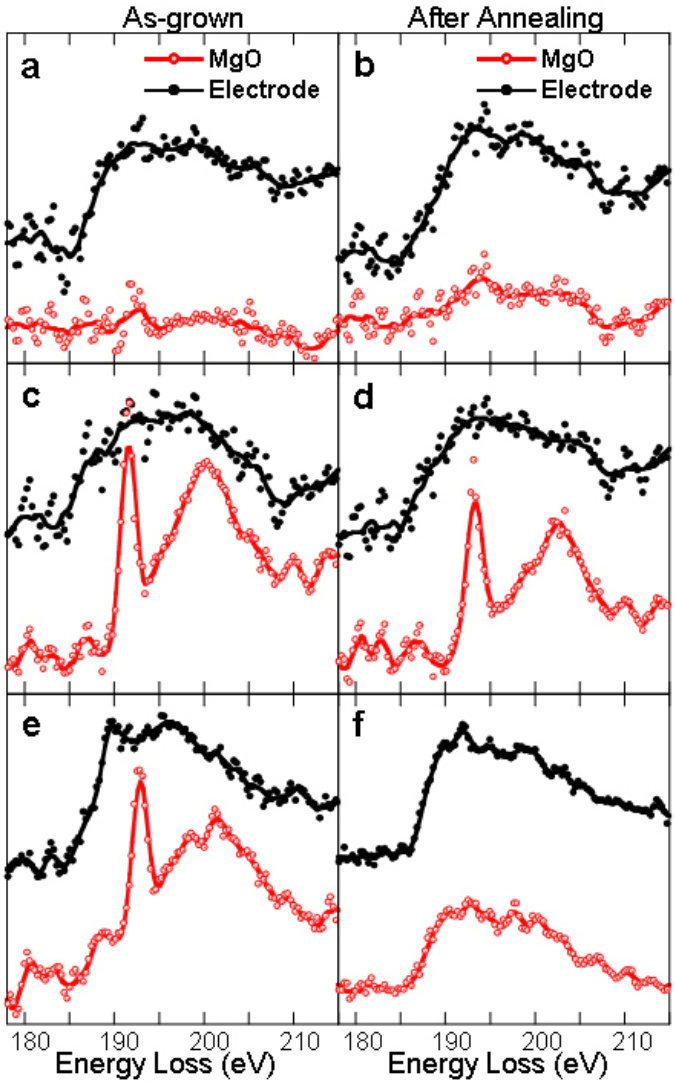

Figure 3.6: B-K EELS edge of CoFeB/MgO/CoFeB MTJ structures showing presence of BO_x in the rf-sputtered MgO layer. B-K edge of CoFeB / 20 Å MgO[eb] / CoFeB MTJ structure before (**a**) and after (**b**) annealing, CoFeB / 20 Å MgO[rf] / CoFeB MTJ structure before (**c**) and after (**d**) annealing, and CoFeB / 5 Å Mg / 5 Å MgO[rf] / CoFeB MTJ structure before (**e**) and after (**f**) annealing. Spectra are plotted with an offset for the purpose of comparison. Spectra are not normalized so that the area under the curve reflects the B content.

the bottom electrode during the growth process, made possible by the release of O ions at the start of MgO sputtering [112].

The presence of BO_x in the MgO[rf] layer, but not in the MgO[eb] layer, partially explains why the O-K edge obtained from the MgO[rf] layer is not as ordered as that obtained from the MgO[eb] layer. Nonetheless, it appears that the MgO[rf] layer still contains MgO characteristics, even though not perfectly, despite the inclusion of BO_x as shown by the O-K and Mg-K edges in Figure 3.3b and 3.4b. Perhaps the gap states evident in the MgO[rf] layer are linked to the presence of BO_x.

The situation for the Mg/MgO[rf] bi-layer is quite different. While BO_x is observed in the as-grown bi-layer (Figure 3.6e) as expected due to the oxidation of the bottom electrode during the rf-sputtering of MgO, after annealing, BO_x is not detected in the bi-layer. Instead, the smaller B-K edge signal from the bi-layer resembles that from the electrode (Figure 3.6f). There are likely two effects at play here - a genuine chemical change in the loss of the BO_x signal, and an artifact of imaging a rough interface in projection in observing the metallic B signal. The total B-K signal found after annealing is less than that before annealing, which indicates that the B content in the bi-layer has been reduced. The remaining B-K edge signal in the annealed Mg/MgO[rf] bi-layer structure has a metallic character that could be due to the presence of un-oxidized B in the bi-layer. However, considering the high affinity of B to O, the presence of un-oxidized B in the MgO[rf] layer seems unlikely. Instead, the metallic B-K edge signal is more likely to be the residual signal from the B in the electrodes, which, due to the rough interfaces between the bi-layer and the electrodes, overlaps with the 5Å-thick Mg under-layer when viewed in projection, as is the case in STEM. This could be most readily checked by a three-dimensional chemical imaging method such as atom-probe tomography [114, 115].

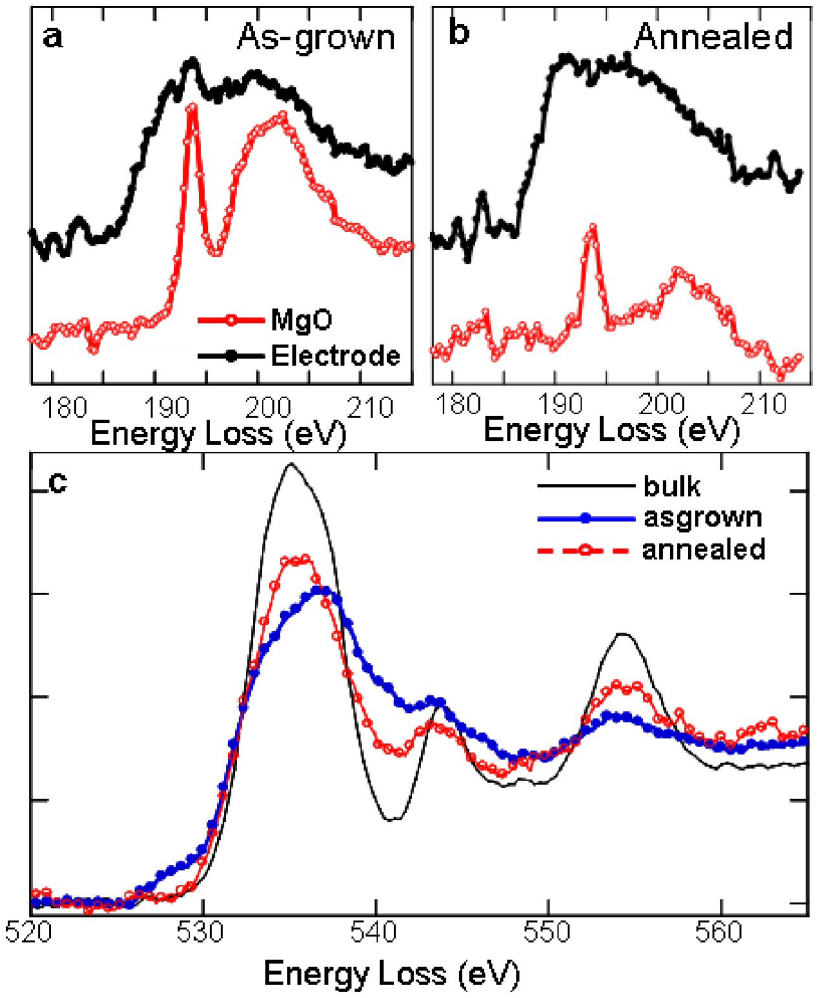

Figure 3.7: B-K and O-K EELS edges of CoFeB / 10 Å Mg / 10 Å MgO / CoFeB structure before and after annealing. B-K edge of CoFeB/ 10 Å Mg / 10 Å MgO[rf] /CoFeB MTJ structure before (**a**) and after (**b**) annealing, **c** O-K edge CoFeB / 10 Å Mg / 10 Å MgO[rf] / CoFeB MTJ structure before and after annealing.

The dramatic BO_x reduction in the annealed Mg/MgO[rf] bi-layer is likely due to the Mg under-layer, which can pull O from the BO_x to form MgO (Mg has a higher affinity to O than B) during annealing and therefore change the B-O bonding configuration. This view is supported by the observation that B remains oxidized in the annealed MgO[rf] layer, where the B-O configuration is unaltered and the O content has not changed. With the Mg/MgO[rf] bi-layer, however, the O-K and Mg-K edge (Figure 3.3c and 3.4c) indicate that the bi-layer is not MgO-like even after annealing. I have also studied a rf-sputtered 10 Å Mg / 10 Å MgO MTJ structure, where annealing is observed to turn the thicker bi-layer into a well-ordered MgO layer that is comparable to the MgO[rf] layer (Figure 3.7). In this case, BO_x is still observed in the as-grown structure but is less than that in the as-grown 5 Å Mg / 5 Å MgO MTJ structure. Again, the amount of BO_x decreased after annealing in the 10 Å Mg / 10 Å MgO [rf] bi-layer. Hence the O concentration seems to be a critical parameter in controlling the BO_x content and a Mg under-layer can act as an O sink that reduces the BO_x content. It should be noted that diffusion of B out of the MgO layer during annealing could also reduce the BO_x content in the MgO layer.

3.4 Conclusion

Using spatially-resolved EELS, significant gap states and BO_x are observed in the MgO[rf] layer of CoFeB / MgO / CoFeB MTJ structure, but not in the MgO[eb] layer. Annealing the structure does not reduce the BO_x content much in the MgO[rf] structure. Since high TMR values have been obtained with thick ($\sim$ 2nm) but not with thin ($\sim$ 1 nm) MgO[rf] layers, this suggests that either some BO_x content can be beneficial for TMR or in those former cases the rf deposition or annealing protocol was sufficiently different from the experiments presented here as to reduce the BO_x content. With the Mg/MgO[rf]

bi-layer structure, BO_x was observed in the as-grown bi-layer but dramatically reduced upon annealing. However, based on O-K and Mg-K edges, the annealed 5 Å Mg / 5 Å MgO[rf] bi-layer does not display MgO characteristics. A thicker Mg/MgO[rf] bi-layer (10 Å Mg / 10 Å MgO[rf]) recovered MgO characteristics and reduced BO_x even further after annealing. Asymmetry in O-K edges between the top and bottom interfaces observed for both the MgO[rf] and MgO[eb] structures may also affect the TMR by breaking the symmetry of the electrode/barrier/electrode junction structure.

CHAPTER 4

TUNNELING MAGNETORESISTANCE OF 200% IN CoFeB/Mg-B-O/CoFeB MAGNETIC TUNNEL JUNCTIONS THROUGH B DIFFUSION REVEALED BY ATOMIC-SCALE SPECTROSCOPIC IMAGING

In the previous chapter, a CoFeB/MgO/CoFeB tri-layer, where the MgO was grown by e-beam evaporation and radio frequency (rf) sputtering, was investigated to find that BO_x formed in the rf-sputtered MgO layer, but not in the e-beam evaporated MgO layer. In this chapter, I will discuss a correlated characterization of the sputtered MgO-based magnetic tunnel junctions (MTJs) with (S)TEM, EELS, and current in-plane tunneling (CIPT) [116] measurements to study how the presence of the BO_x influences tunneling magnetoresistance (TMR). John Read in Buhrman group grew the samples and performed CIPT measurements to obtain TMR values versus resistance-area (RA) products.

Using atomic-scale electron spectroscopic imaging, I observed an interfacial Mg-B-O layer at the sputtered MgO/CoFeB single interface after annealing at 350 °C for up to 2 hours. The ~ 2nm thick layer formed due to oxidation of the base electrode during the rf sputtering of MgO. This suggests that in rf-sputtered MgO-based MTJs with B-alloyed electrodes, BO_x forms during sputtering, and diffuses into the MgO, resulting in Mg-B-O formation. We also observed Mn from the IrMn pinning layer in the Mg-B-O. We measured TMR of ~ 200 % in IrMn/CoFeB/Mg-B-O/CoFeB MTJs after annealing, demonstrating that Mg-B-O barriers can produce relatively high TMR.

4.1 Introduction

Due to their high TMR [52, 53, 117], MgO-based MTJs have become a key component in magnetoresistive random access memory (MRAM) technology, a potential universal memory solution [118], along with other technologies such as read heads and logic circuits. A remarkably high TMR of 1010 % at 5 K was recently reported in sputtered CoFeB/MgO/CoFeB MTJs with a 2.1 nm-thick MgO barrier [119, 120], which approaches the theoretically predicted TMR value [50, 51].

The widely accepted theoretical model to explain high TMR for the MgO-based MTJs is a DFT calculation of an epitaxially grown, defect-free Fe/MgO/Fe sandwich structure [50, 51, 121]. In this model, the majority spin state tunnels through a state that has s-like symmetry, whereas the minority spin state tunnels through a state that has d-like symmetry. The decay rate of the minority spin tunneling state is a few orders of magnitude faster than the decay rate of the majority spin tunneling state because the overlap through the minority spin tunneling state is much smaller than that through the majority spin tunneling state due to the symmetry. The spin-filtering tunneling effect due to the large difference in decay rates for the majority and minority spin states improves TMR drastically for the Fe/MgO/Fe MTJs.

Contrary to the theoretical requirement of a perfect crystal structure for MgO-based MTJs for high TMR, the MgO-based MTJs grown by the rf-sputtering technique exhibit inter-diffusion of species, which must disrupt the overall crystallinity of the structure. (In industry, the rf-sputtering growth method is strongly preferred to other growth methods that can control growth much more precisely for technological reasons such as mass production scalability and production cost.) In the previous chapter, I discussed the presence of BO_x in the rf sputtered MgO layer, observed by EELS [122]. Similarly,

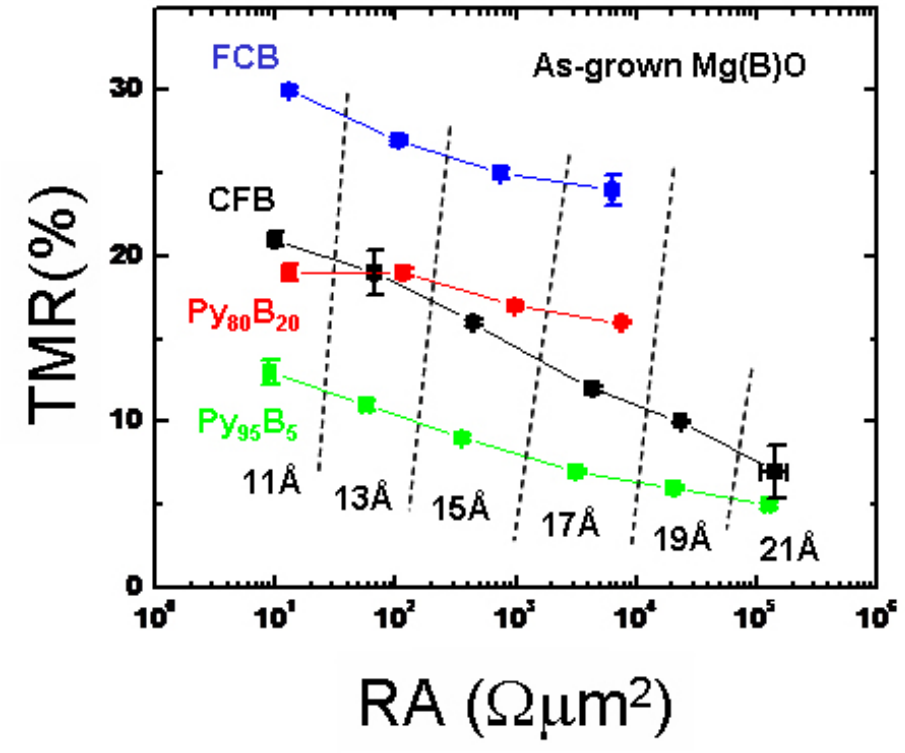

Figure 4.1: Comparative TMR measurements of MgO-based MTJ structures. CIPT measurements of as-grown samples with different electrode alloy compositions show TMR as a function of a RA product. Four different electrodes were used: $Co_{60}Fe_{20}B_{20}$ (CFB) electrodes as both the free and the fixed layer (black), $Fe_{60}Co_{20}B_{20}$ (FCB) electrodes as both the free and the fixed layer (blue), $Ni_{77}Fe_{18}B_5$ as the free layer (green), and $Ni_{65}Fe_{15}B_{20}$ as the free layer (red). Contrary to the theoretical prediction, the TMR of as-grown samples increases with a decreasing RA product(thinner MgO). Error bars represent the standard deviation of multiple CIPT measurements for each data point.

other groups have also reported the presence of BO_x in the MgO layer [103, 123, 124]. Can high TMR be achieved with inclusion of BO_x in the MgO layer? High TMR in an Mg-B-O MTJ could suggest that the tunneling mechanism through the barrier deviates from current theories.

The presence of BO_x in the MgO-based MTJs that produce high TMR presents a challenge to the existing theoretical model because the actual junction structure does not match the ideal structure that allows coherent spin tunneling in the theory. To investigate whether experimental results of MgO-based MTJs with the inclusion of BO_x in the barrier layer would agree with the theoretical prediction, TMR as a function of the barrier thickness was studied. Because the difference in the decay rates between the majority and the minority spin tunneling states gets larger for a thicker MgO barrier, it is predicted that TMR would increase for a thicker barrier. Figure 4.1 shows experimental TMR values as a function of a RA product for as-grown samples with various electrode alloy compositions. Opposite to the theoretical prediction of higher TMR for a thicker MgO, the TMR values decreased for thicker MgO barriers in these as-grown MTJs (the RA product can be directly correlated with the thickness of the MgO layer). This suggests that the tunneling mechanism through the barrier must be more complex than a direct tunneling of the majority and minority spins. The correlated characterization of the MgO-based MTJs with STEM, EELS, and CIPT is discussed in this chapter to examine possible mechanisms for the high TMR.

4.2 Methods

Stack Growth. Thin film stacks, which include the MgO-based MTJs for CIPT and EELS study, were grown in a vacuum system with a nominal base pressure of 3 x 10^{-9}

Torr containing multiple magnetron sputtering sources. To achieve low bottom electrode sheet resistance, necessary for CIPT study of low RA MTJs, a Ta/CuN multi-layer was placed below the MTJ film stack. This low resistance under-layer stack, 5 nm Ta / [20 nm CuN / 3 nm Ta] x 4, served also to form a smooth surface to help seed growth of the subsequent MTJ layers. On the seed layer was grown a 15 nm IrMn anti-ferromagnetic pinning layer, then the MgO-based MTJ, then a capping layer, 10 nm Ta / 7 nm Ru, to facilitate the CIPT measurement. The MTJ structure was 4 nm base electrode / MgO / 2 nm top electrode. The MgO layer was grown with rf sputtering at high power in Ar while a getter material was also being deposited within the deposition chamber, and the CuN layer was grown using reactive dc sputtering of Cu in an Ar / N mixture. Otherwise, the layers were grown with conventional dc sputtering in Ar on 3-inch diameter thermally oxidized Si wafers. The thickness of the Mg-B-O layers studied in this chapter varied from 2.1 to 1.1 nm, with the lower limit set by the ability to obtain a sufficient sheet resistance in the base electrode and probe spacing to obtain reliable CIPT data for the sample.

Additionally, a single interface sample was grown to investigate the formation and the spatial distribution of BO_x in MgO more carefully. The growth condition is the same as above and the stack structure is seed layer / IrMn(15) / $Co_{60}Fe_{20}B_{20}$(4) / MgO(10) / capping layer (in nm) on a thermally-oxidized silicon wafer. The capping layer is Ta(8) / Ru(7) and the seed layer is Ta(5) / [Cu(N)(20) / Ta(3)]x4, which is the same as before.

CIPT Measurements. The centers of the wafers were cut into small $\sim$ 1 cm^2 chips, yielding several samples with a particular barrier thickness and electrode alloy combination. Chips were then annealed in modest vacuum of 3 x 10^{-6} Torr to 250, 300, or 350 $^\circ$ C, for up to 2 hours. The chips were then studied with CIPT using a CAPRES tool which yielded TMR, RA, and the sheet resistance values for both the top and the bottom

electrodes. We used the sheet resistance values as a check for the accuracy of the CIPT fit to assure its validity. The sheet resistance fit values of both the top and bottom electrodes were similar to those measured with the van der Pauw technique using electrode test layers.

(S)TEM Sample Preparations. The chips were also prepared for (S)TEM and EELS study using mechanical polishing and ion milling to create thin wedge-shaped samples of structures identical to those studied with CIPT. A focused ion beam was used to prepare (S)TEM samples as well to study the effects of electrode oxidation during mechanical polishing. Comparison of the two sample preparation methods yielded that mechanical polishing followed by ion milling did not induce serious oxidation in electrodes as long as the time duration in which the samples were left in ambient conditions were limited to less than an hour. The samples were plasma-cleaned for $10 \sim 20$ seconds before being inserted into the microscopes to eliminate contamination issues.

EELS Studies. A NION UltraSTEM, which is equipped with a spherical aberration corrector upto the 5th order, was used to perform spectroscopic imaging at the MgO / CoFeB single interface. Figure 4.2 shows the silicon 110 projection image taken with the NION UltraSTEM. The silicon dumb-bells are clearly resolved to show that the probe resolution is roughly 1 Å, which is evident in the Fourier transform of the image (inset in Figure 4.2). A dark region in the central area of the image is due to the mass loss of silicon induced by the large probe current, typically ranging between 50 to 110 pA. For spectroscopic imaging [125], the acquisition time was set between 10 ms to 30 ms, which was necessary to minimize the sample damage and sample drift during the acquisition. Also, the energy range for EELS was set wide enough to contain all B, O, Mn, Fe, and Co edges within the same spectrum, which was done by setting the energy dispersion to be 0.7 eV/channel or 1 eV/channel.

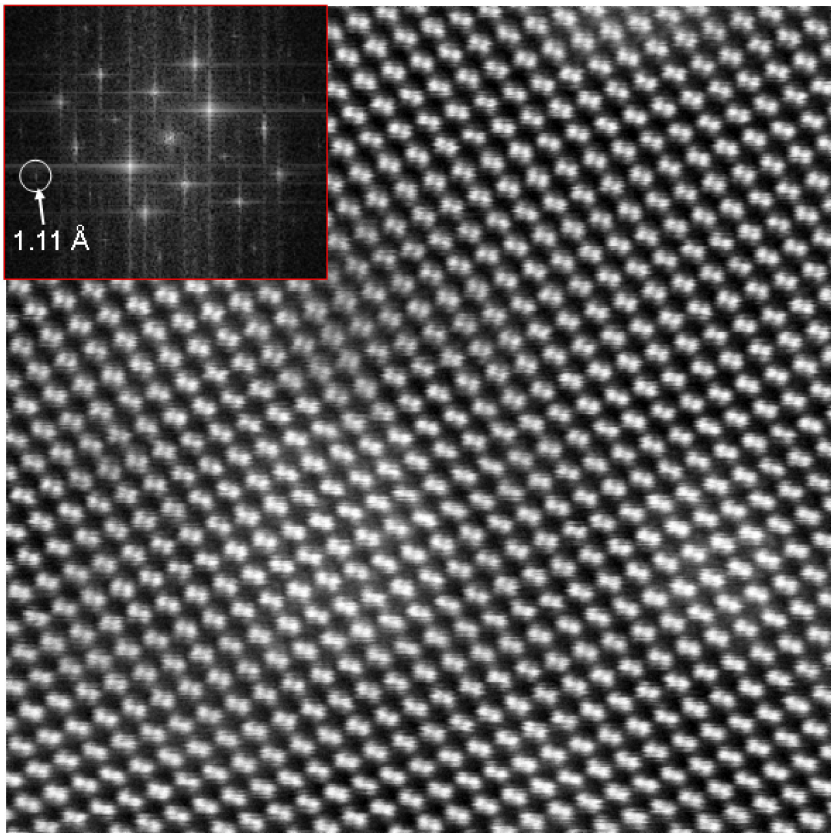

Figure 4.2: ADF-STEM image of Si 110 using the NION UltraSTEM. The inset shows the Fourier transform of the ADF STEM image. The diffraction spot indicated by the arrow is (-4,2,-2), which corresponds to 1.11 Angstrom in real space.

For the remainder of the STEM/EELS studies, a 200 kV FEI Tecnai F20-ST STEM fitted with a monochromator and a Gatan imaging filter 865-ER was used. The electron beam was focused to form a 2 Å-diameter probe with a convergence semi-angle of ~ 9.6 mrad. To reduce the electron dose per unit area for minimum radiation damage, EELS spectra were taken mostly in a line parallel to the electrode-barrier interface. The spectrometer dispersion was set to 0.3 eV/channel or 0.5 eV/channel to capture the wide energy range needed to record all edges simultaneously, resulting in an energy resolution of 1 eV. For CBED measurements, the convergence angle was changed to 2

mrad to produce smaller diffracting disks which overlap less with neighboring disks for clearer diffraction patterns. At a convergence angle of 2 mrad the resolution of the probe degrades to roughly a nanometer.

4.2.1 Issues regarding EELS studies

Electrode Oxidation Problem. The surface of CoFeB electrodes was found to oxidize during mechanical polishing, which was evident by a significant amount of metal oxide component in the O-K edge obtained from the electrodes region. The oxidation problem can be minimized by shortening the time the finished TEM wedge-shaped sample spends in the ambient condition. This was achieved by examining the samples in the electron microscope immediately after ion-milling them. However, the problem cannot be completely avoided. In the very thin part of the sample, the O-K edge from the electrodes showed that the electrodes were still oxidized. Because the oxidation occurs at the surfaces of the wedge sample, the contribution from the oxidation is particularly noticeable at the very thin part of the sample. To minimize this problem to a negligible level, a thicker part of the sample was used for EELS analysis. The O-K edge was used as a guide to determine when the surface oxidation of the electrodes would become a negligible factor in EELS analysis.

Background Issue with B-K Edge. When studying core-loss EELS edges, the background signal is subtracted from the EELS core-loss edge by fitting a power law to a spectrum in the energy-loss region just before the edge. The power law fit to the pre-edge signal is generally excellent, eliminating complications in analyzing the EELS data. However, subtracting the background signal in B-K edge by fitting a simple power law was insufficient because the background signal would change drastically across different

layers due to varying contributions from elastically scattered electrons, which resulted in a poor power law fit in the pre-edge region. Furthermore, the small B-K signal meant that the relative error due to a poor background subtraction was significant. In order to overcome the background issue in the B-K edge, an additional linear background subtraction was performed after the power-law background subtraction. One guideline in doing the linear background subtraction was that the fine structure of the B-K edge should stay positive. This effectively under-estimates the amount of BO_x in MgO.

4.3 Results and Discussion I - MgO/CoFeB Single Interface Study

Several groups reported the presence of a substantial concentration of BO_x in sputtered MgO-based MTJs [103, 122–124, 126], but detailed studies of the spatial distribution of BO_x in the MgO layer and how the mix of BO_x into the MgO layer affects TMR are lacking. To investigate the formation and the spatial distribution of BO_x in MgO, I examined a sputtered, single MgO/CoFeB interface as a means of better understanding the material properties of thin Mg-B-O-based MTJs. A thin film stack of seed layer / IrMn(15) / $Co_{60}Fe_{20}B_{20}$(4) / MgO (10) / capping layer (in nm) was grown on a thermally oxidized Si wafer at a nominal base pressure of $3x10^{-9}$ Torr. The capping layer is Ta(8) / Ru(7) and the seed layer is Ta(5) / [CuN(20) / Ta(3)]x4, served as a low resistance stack for current-in-plane tunneling (CIPT) measurements [116]. The stack was annealed in vacuum at 350 °C for 90 minutes. Because the MgO layer is thick, the single interface structure allows us to investigate the diffusion length of BO_x as well as to study how the ordering of the MgO changes as it gets further away from the interface.

Figure 4.3 shows S/TEM images of the single-interface stack before and after annealing. Rectangular lattice fringes are observed in the MgO layer both before and

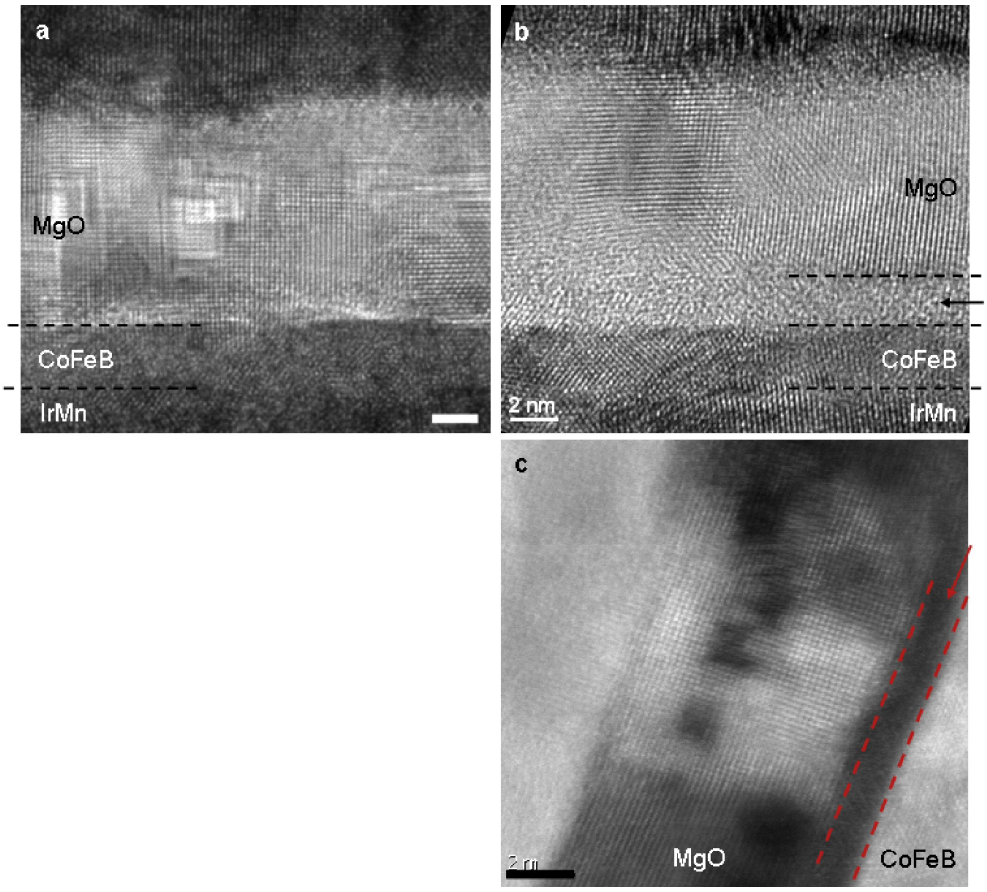

Figure 4.3: TEM/STEM images of the IrMn / CoFeB / MgO (~ 10nm) / Ta structure before (**a**) and after annealing (**b** and **c**). **a** and **b** are TEM images while **c** is a STEM image. An amorphous layer at the MgO/CoFeB interface forms during annealing, as indicated by the arrows in **b** and **c**.

after annealing, indicating that the rock-salt crystal structure of bulk MgO is preserved. However, changes in the direction of the lattice fringe in the MgO layer are observed to indicate grain boundaries, showing that the layer is poly-crystalline. Before annealing, a sharp interface between the MgO and the base electrode CoFeB is observed where the crystalline MgO starts at the interface (Figure 4.3a). After annealing, a ~ 2nm-thick, amorphous layer is observed between the MgO and the base electrode, as indicated by the arrows in Figure 4.3b and 4.3c. Rectangular holes are apparent in the MgO lay-

ers in both the as-grown and annealed case. They formed while continuously imaging the radiation-sensitive MgO with the intense electron probe. For spectroscopic studies, the electron dose was carefully monitored to minimize radiation damage of the barrier materials.

To examine the chemical properties of the amorphous interfacial layer observed in the annealed sample, I acquired EEL spectroscopic images, which give two-dimensional chemical and electronic maps at atomic resolution [125], of the as-grown and annealed MgO/CoFeB interfaces. Figure 4.4 shows a raw spectroscopic image of the annealed sample, where each pixel contains an EEL spectrum. Spectra from two pixels, one near the interface and the other far away from the interface, are selectively shown as an example. It is important that both the B edge and the O edge are contained within the same spectrum so that an atomic ratio of B to O can be obtained. Although not apparent in Figure 4.4, the spectra are noisy because the acquisition time was only 10 ~ 30 ms per spectrum, which was necessary to minimize radiation damage and sample drift during the acquisition. However, all the edges and their fine structures are clearly above the noise level.

First, a 147x60 pixel spectroscopic image (SI) was taken from the as-grown MgO/CoFeB interface and is shown in Figure 4.5. Figure 4.5**a** shows a reference annular dark-field STEM image from which the SI was taken. From the SI, chemical maps were obtained by integrating the area under each edge after background subtraction. Chemical maps of O, B, Co, Fe, and Mn of the as-grown interface are shown in Figure 4.5**b-f** respectively and a concentration profile of Fe is shown in Figure 4.5**g**. Evident from the chemical maps, all elements are found in their corresponding layers where they are supposed to be. The intensity decrease in the center of the O map (Figure 4.5**b**) is a simple mass reduction in the barrier due to holes which formed during imaging (Figure

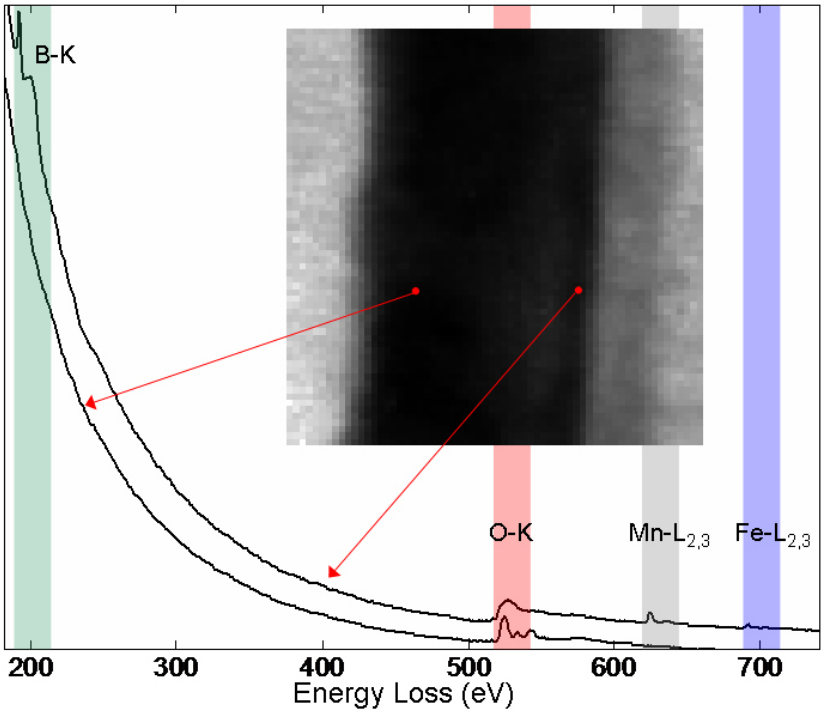

Figure 4.4: Raw EELS spectra from the 2D spectroscopic image. The inset shows the 64x64 pixel spectrum image where each pixel contains an EEL spectrum. Two spectra from the spectrum image are plotted as an example. The spectrum near the interface shows a clear B oxide signature while the O K-edge of the spectrum, acquired deep in the MgO layer, shows three clear peaks which is indicative of bulk MgO. The shaded areas indicate the energy windows over which the EELS edges are integrated to obtain the relative concentration of each element, normalized to the maximum O intensity. The relative concentration of a particular element, for example B to O, is obtained by scaling the integrated intensity of B to O by s(O)/s(B), where s(X) is a cross-section of X using the Hartree-Slater model (Cross-section values for all elements were obtained from Digital Micrograph EELS quantification table).

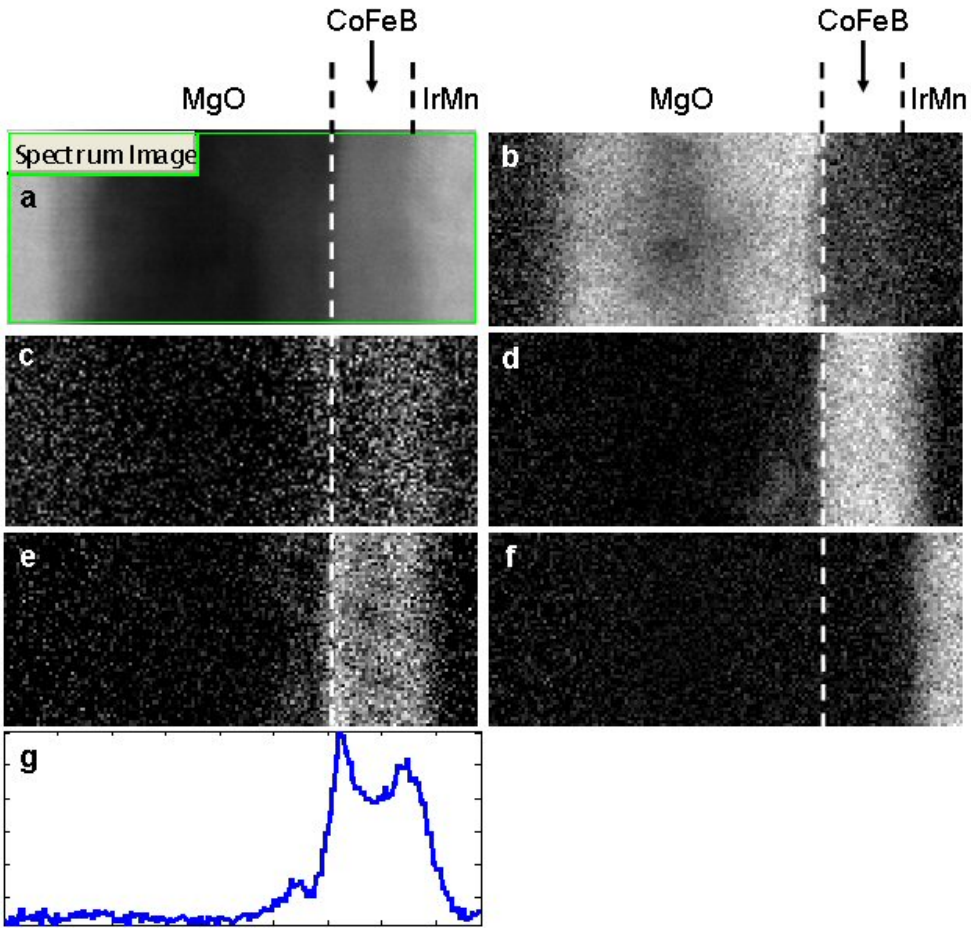

Figure 4.5: Spectroscopic imaging of the as-grown IrMn / CoFeB / MgO (~ 10nm) / Ta structure showing different chemical maps. A 147x60 pixel spectroscopic image was taken from the reference ADF STEM image shown in **a**. The intensity maps of O, B, Co, Fe, and Mn are shown in **b, c, d, e** and **f** respectively. A concentration profile of Fe is shown in **g**.

4.3**a** shows the rectangular holes). From the B map (Figure 4.5**c**), more B is observed in the lower half of the base electrode than in the upper half. The fine structure of the B-K edge indicates that B near the MgO/CoFeB interface is BO_x, which is due to oxidation of the base electrode during rf sputtering of MgO [103]. Also, accumulation of Fe at the interface is observed as seen in Figure 4.5**g**, which we attributed to formation of FeO_x during growth by O ions released by the sputtering of MgO [103, 112]. Despite the presence of BO_x and FeO_x at the interface, the O-K EELS edge obtained from the barrier layer suggests that the MgO near the interface exhibits mostly bulk MgO characteristics, which agrees with the observation that MgO is crystalline at the interface in the as-grown case (Figure 4.3**a**).

To observe how the chemical ordering of MgO changes as a function of distance away from the interface, the fine structure of the O-K edge from the SI (Figure 4.5**b**) was investigated further. The O-K edge in line mode was obtained by summing up pixels that are in parallel with the interface. Figure4.6**a** and 4.6**b** show the O chemical map and the O-K edge (as a function of distance away from the interface) of the as-grown sample respectively. Most of the O-K edge shows bulk MgO characteristics, indicated by the three distinct peaks [105]. Even the O-K edge near the interface appears to follow the bulk MgO characteristics closely, except the reduced signal strength. Mn-L edge shown in Figure 4.6**c** indicates that Mn stays in the IrMn pinning layer in the as-grown case, as expected. The Fe-L edge displayed in Figure 4.6**d** shows that a small amount of Fe, likely as FeO_x exists at the MgO/CoFeB interface. This is manifested in the Fe chemical map (Figure 4.5**e**) as a bright line right at the interface and also in the Fe concentration profile (Figure 4.5**g**) as a peak at the interface.

Figure 4.7 shows a 64x64 pixel SI of the annealed MgO/CoFeB interface. Figure 4.7**a** shows the reference ADF STEM image and Figure 4.7**b-f** show the intensity maps

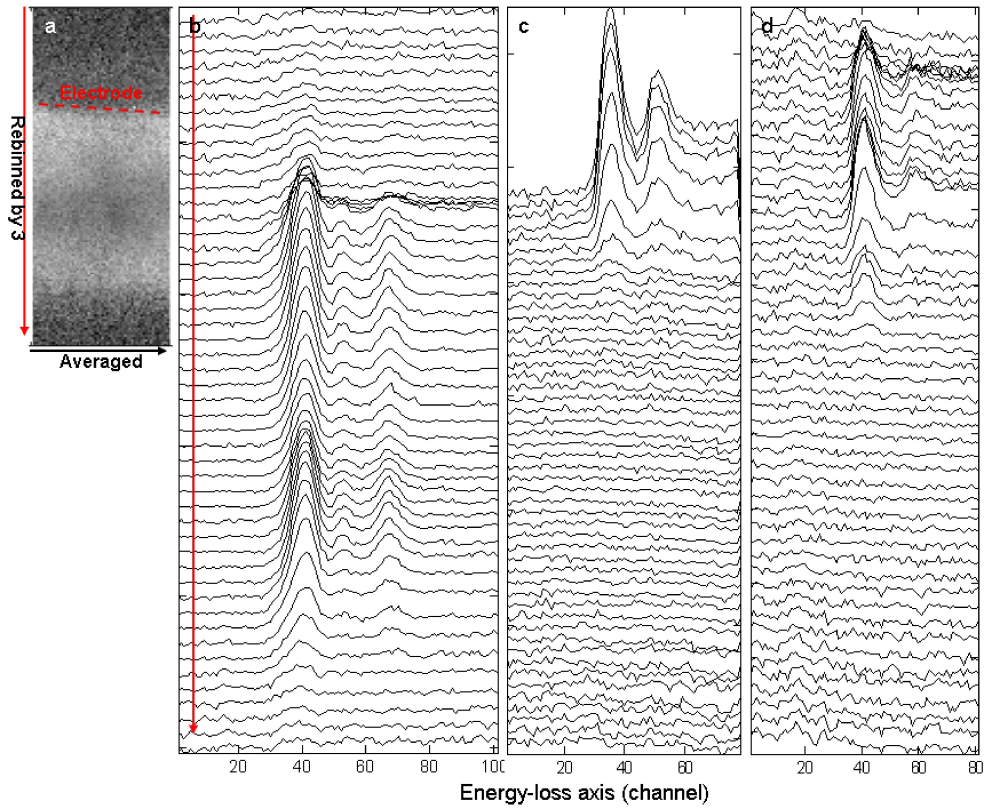

Figure 4.6: O-K, Mn-L, and Fe-L spectra from the spectroscopic image of the as-grown IrMn / CoFeB / MgO (~ 10nm) / Ta structure. **a** shows the O intensity map while **b**-**d** show O-K, Mn-L, and Fe-L edges respectively.

of O, B, Fe, Co, and Mn obtained from the spectroscopic image. The bar charts in each panel **b-f** indicate the relative concentration of each element with respect to maximum O intensity, which is set to 1. A RGB plot of O (red), B (green), and Fe (blue) is shown in Figure 4.7**g**. It is immediately apparent that the amorphous interfacial layer consists of BO_x mainly. Boron is not observed in the electrode. This indicates that "the remaining" B from the electrode reacted with the MgO layer during annealing, in addition to already present BO_x at the interface during rf sputtering. Also, the concentration of BO_x in the interfacial layer is uniform along the layer as evident in Figure 4.7**d**. This spatial

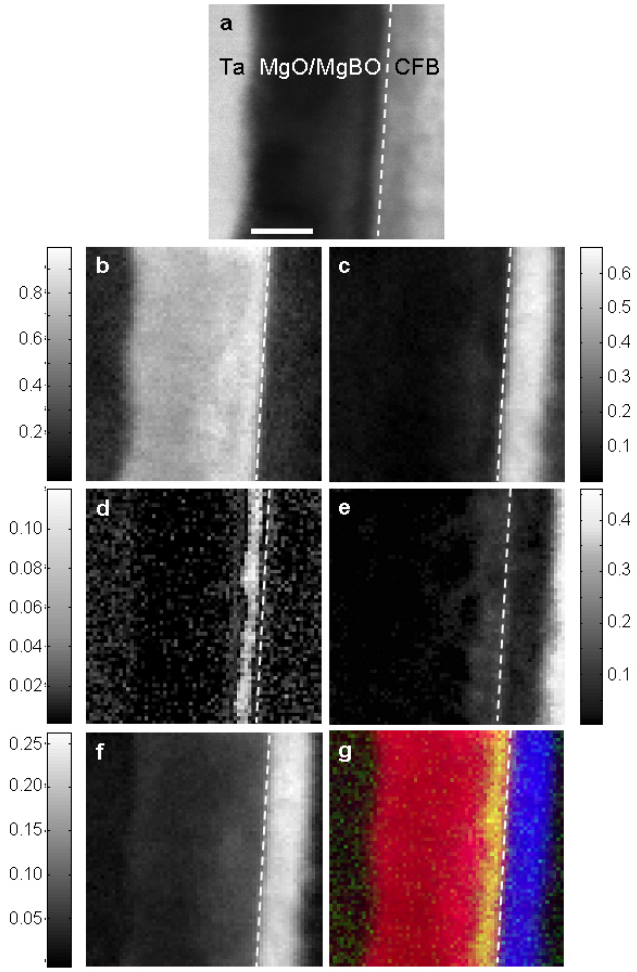

Figure 4.7: Spectroscopic imaging of the annealed IrMn / CoFeB / MgO (~ 10nm) / Ta structure. 64 x 64 pixel EELS were taken from the region shown in the reference image in **a**. The scale bar in **a-g** is 5 nm. The dotted line indicates the MgO/CoFeB interface. The intensity map of the O, B, Fe, Co, and Mn are shown in **b**, **d**, **f**, **c**, and **e**, respectively. The integrated O K-edge intensity is normalized so that the maximum value is 1, and the B, Fe, Mn, and Co intensities are scaled relative to the maximum integrated O K-edge intensity. The gray scale bars in **b-f** indicate the relative concentration of each element, normalized to the maximum O intensity. An RGB plot is displayed in **g**, where O is red, B is green and Fe is blue. In the RGB color scheme, the mixing of red and green yields yellow, indicating BO_x within the barrier material.

distribution of BO_x is clear in the RGB plot where the yellow region (BO_x) is a result of mixing red (O) and green (B). Hence, we conclude that the interfacial layer is a composite Mg-B-O. The significant amount of BO_x in the interfacial layer explains why the layer is amorphous as B is a glass forming material.

Co in the electrode does not diffuse, as evident in the Co intensity map that sharply decreases at the interface. Fe, on the other hand, was observed further into the MgO layer, past the interfacial layer, but not in the interfacial layer. We attribute this to a likelihood that, during annealing, B reduces FeO_x (which forms at the interface during growth), to produce BO_x. Most of the reduced Fe would then return back to the electrode, but some could remain in the MgO layer. Moreover, we observe that Mn from the IrMn pinning layer diffuses all the way into the interfacial layer. Mn was not observed in the electrode. It is likely that Mn is oxidized in the interfacial layer. The observed Mn in the MgO layer may reduce TMR in MgO-based MTJs as suggested by the recent report which achieved $\sim$ 600 % TMR in MgO-based MTJs without the IrMn pinning layer[119, 120].

Experimentally, the MgO layer in full MTJ structures remains crystalline after annealing [122], unlike our observation that a $\sim$ 2nm thick, amorphous Mg-B-O layer forms at the MgO/CoFeB single interface after annealing. In the single interface sample where the MgO was thick (10 nm), the strain of growing MgO on CoFeB could get released fully during annealing by producing two separate phases - a crystalline, low-energy equilibrium state of the top MgO and an amorphous transition Mg-B-O layer near the interface. This could be achieved if Mg near the interface could diffuse upward in the thick MgO, promoting a well-ordered MgO in the upper half of the layer. Indeed we observe that the concentration of Mg near the interface is considerably less than in the crystalline region. The ratio of Mg to O is 1 in the crystalline region of the barrier. In

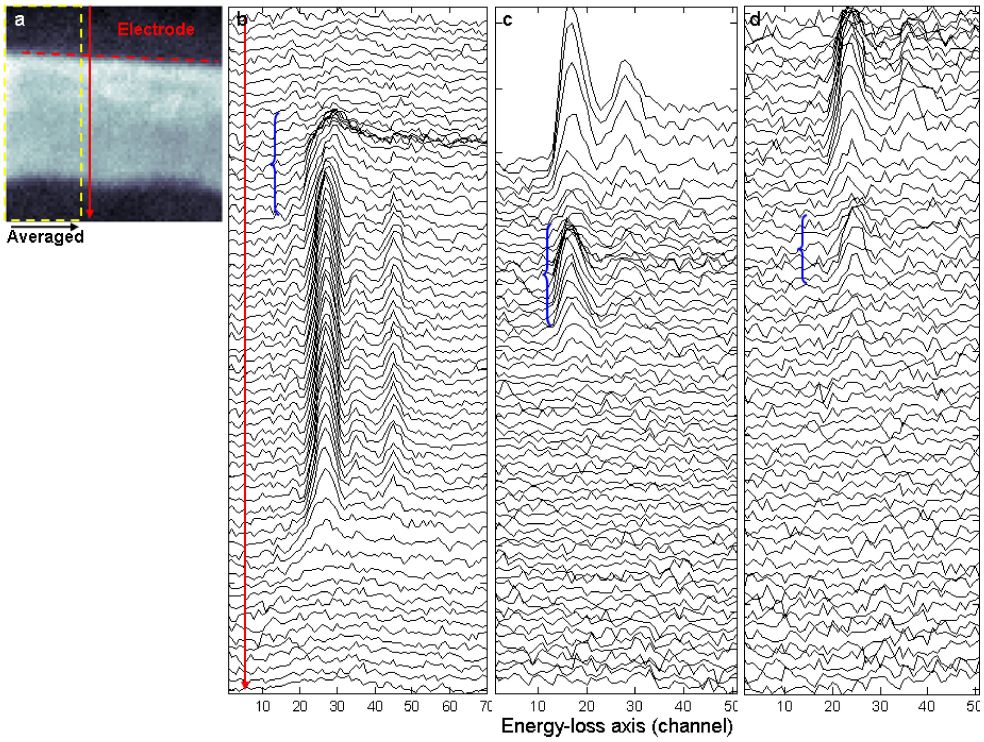

Figure 4.8: O-K, Mn-L, and Fe-L spectra from the spectroscopic image of the annealed IrMn / CoFeB / MgO (~ 10nm) / Ta structure. **a** shows the O intensity map while **b**-**d** show O-K, Mn-L, and Fe-L edges respectively.

MgO-based MTJs where the MgO layer is less than 2 nm thick, there is little space for diffusion of Mg. Hence, it may be energetically favorable for MgO to remain a strained, somewhat disordered poly-crystalline layer that readily accommodates the inclusion of BO_x rather than to separate into two phases, a crystalline and an amorphous phase.

Figure 4.8 shows the fine structure of O-K, Mn-L, and Fe-L edges from the SI of the annealed MgO/CoFeB interface, which was investigated in the same way as the as-grown case shown in Figure 4.6. Most of the MgO region shows the bulk MgO O-K edge except in the interfacial layer. As evident from the O-K edges shown in Figure 4.8b, the O-K edge in the interfacial layer is that of metal-oxide, confirming again that

the interfacial layer contains a significant amount of BO_x and some of MnO_x. The Mn-L edge shown in Figure 4.6c clearly shows the presence of MnO_x in the interfacial layer, but not in the electrode. A small amount of Fe as FeO_x is also observed in the MgO layer, as shown by Figure 4.8d.

Figure 4.9 shows the O-K edge of the SI of the annealed sample, decomposed into two principal components for clear distribution of the interfacial metal-oxide layer in 2D. The first principal component is the bulk MgO O-K edge and the second is the metal oxide O-K edge. Figure 4.9e shows the two principal components. Non-linear least square fitting was used to decompose each O-K edge into the two components. As expected, the metal oxide is found in the amorphous, interfacial layer (Figure 4.9d). The rest of the MgO layer shows a clear bulk MgO characteristics (Figure 4.9c). The top interface also shows a disordered O-K edge.

The clear Mg-B-O interfacial layer along with presence of MnO_x in the Mg-B-O raises a question of how the incorporation of these metal oxides influences TMR. Another question we need to address is, 'Is the diffusion of BO_x in the single-interface structure the same as in the thin MgO-based MTJs?'. In order to address both questions, thin MgO-based MTJs were grown and the TMR and RA products were measured using the CIPT technique, which is discussed in the next section.

4.4 Results and Discussion II - Thin Mg-B-O Magnetic Tunnel Junctions and Their TMR Values

Full MTJs with various thicknesses of the Mg-B-O layer and different compositions of electrodes were grown for TMR and RA measurements. The junction structure was Si

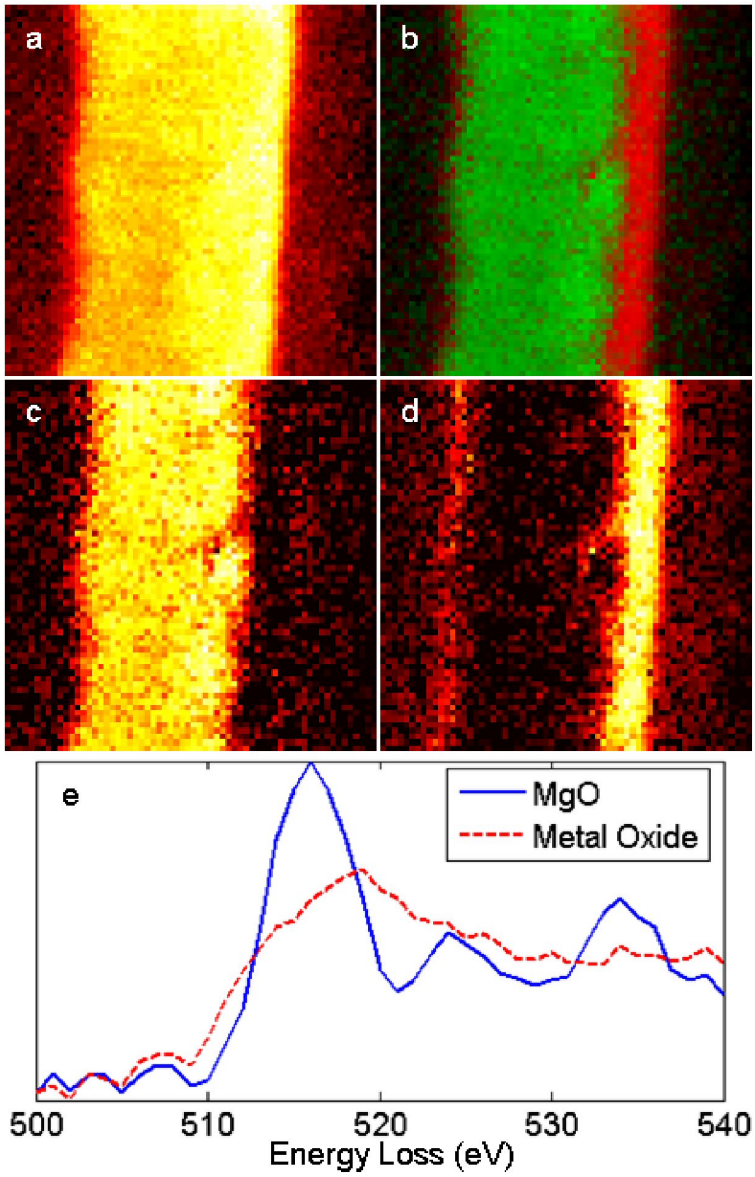

Figure 4.9: O maps decomposed into bulk MgO and transition metal oxide from the spectroscopic imaging of the annealed IrMn / CoFeB / MgO (~ 10nm) / Ta structure. **a** shows the O intensity map. **c** and **d** show the decomposed O intensity map of the bulk MgO component and the transition-metal oxide component. bf b is rg plot combining **c** and **d** together. bf e shows the two component spectra.

/ SiO_x / seed layer / IrMn(15) / base (fixed) electrode (4) / Mg-B-O (1.1 ~ 2.2) / free electrode (3) / capping layer (in nm), where the seed and the capping layers are the same as before [127]. Four different electrode compositions were used in combination: $Co_{60}Fe_{20}B_{20}$, $Fe_{60}Co_{20}B_{20}$, $Ni_{65}Fe_{15}B_{20}$, and $Ni_{77}Fe_{18}B_5$. The IrMn layer serves as a pinning layer to fix the magnetization of the bottom electrode. With the pinning layer, only two relative magnetization orientations are possible between the base and the free electrodes. Figure 4.10 shows a bright field STEM image of a full Mg-B-O-based MTJ stack.

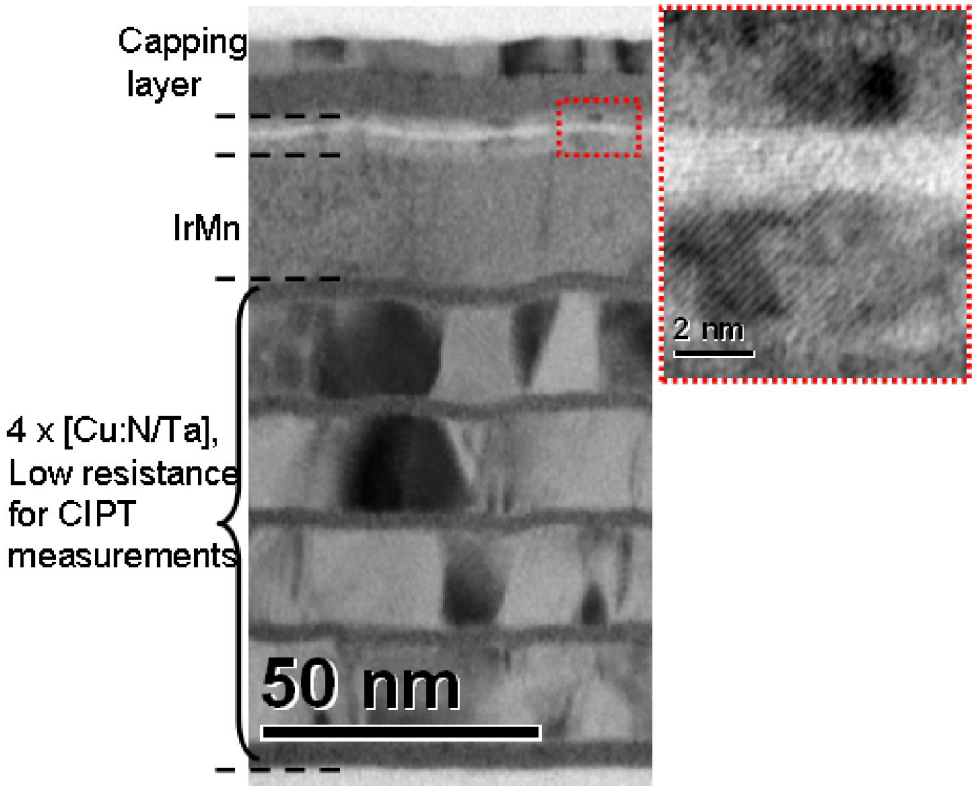

Figure 4.10: A bright-field STEM image of a complete Mg-B-O MTJ stack. The red dotted box indicates the key component of the stack, 4 nm base electrode / 1.1 ~ 2.2 nm Mg-B-O / 3 nm free electrode.

Despite the retained crystallinity in full MTJs as shown in Figure 4.10, I still observe, from EELS measurements, that the barrier is a Mg-B-O material. The B-K and O-K

EELS edges of one of the working Mg-B-O-based MTJs before and after annealing are shown in Figure 4.11. Two types of B edge, metallic B and BO_x, were observed in the MTJ stack. The fine structure of the metallic B consists of one broad peak, as indicated by spectra numbered 1 and 30 in Figure 4.11**e**, while the fine structure of BO_x consists of two distinct peaks, as shown by spectra located in the middle (thick lines) of Figure 4.11**c** and **e**. After annealing from Figure 4.11**e**, BO_x is clearly observed in the barrier layer although the crystallinity of the layer is preserved, as indicated by the three distinct peaks in the O-K edge in Figure 4.11**f** [105, 128]. The concentration ratios of B to O and Mg to O in the barrier after annealing are roughly 8 % (+/- 1.5 %) and 67 % (+/- 11 %) respectively, suggesting the composition of $Mg_{0.38}B_{0.05}O_{0.57}$. B is not observed in the electrodes (spectra obtained from the electrodes are flat), indicating that B diffused out of the electrodes and into the adjacent layers during annealing. The absence of B, a glass-forming material, in the electrodes after annealing leads to crystallization of the electrodes with the barrier, which improves TMR due to coherent tunneling [50, 51].

Four different electrodes were used in combination: $Co_{60}Fe_{20}B_{20}$, $Fe_{60}Co_{20}B_{60}$, $Ni_{65}Fe_{15}B_{20}$, and $Ni_{77}Fe_{18}B_5$. The permalloy electrodes ($Ni_{65}Fe_{15}B_{20}$ and $Ni_{77}Fe_{18}B_5$) were used as free (top) electrodes. Permalloy is a nearly ideal free electrode material because it exhibits no magnetocrystalline anisotropy and has small saturation magnetization, coercivity, and magnetostriction values. Such magnetic properties mean reduced tunneling current densities required to reverse the relative orientation of the free electrode magnetization in spin transfer torque based MRAM (STT-MRAM) architectures [129]. STT-MRAM promises to substantially enhance circuit density and speed, in comparison to magnetic field switching, and could become a universal memory solution.

Figure 4.12 shows TMR versus RA measurements of all Mg-B-O MTJs as a function of annealing temperatures. For all junctions except the junction with the $Ni_{77}Fe_{18}B_5$

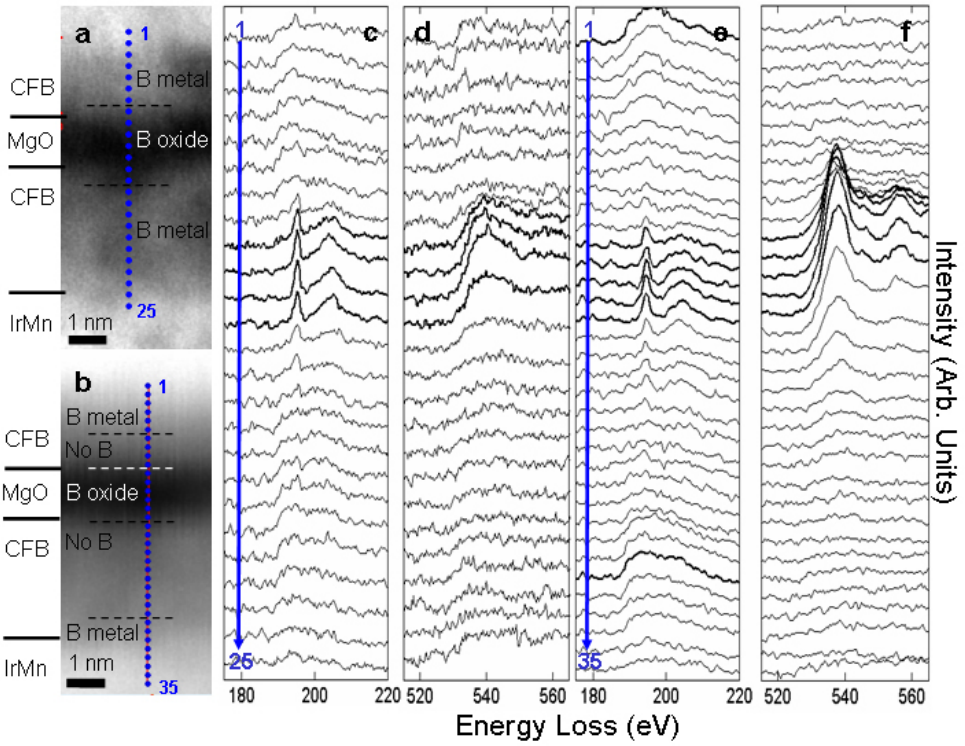

Figure 4.11: STEM and spot mode EELS study of a CoFeB/MgO/CoFeB MTJ. STEM-ADF images of the as-grown and annealed junction are shown in **a** and **b** respectively. Blue dots indicate the probe spots from which EEL spectra were acquired. B-K and O-K EELS from the as-grown junction are shown in **c** and **d**, while those from the annealed junction are shown in **e** and **f** respectively. EELS data from the as-grown sample shows that B oxide forms during growth (**c**), and that the O within the barrier material is significantly disordered as indicated by the O-K edge which has only one broad peak (**d**). After annealing the B oxide remains within the barrier (**e**). During annealing the B oxide is distributed within the MgO layer forming a Mg-B-O material whose O-O ordering improves upon annealing and becomes similar to that of bulk MgO, as shown by the O-K EELS edge in **f**. The boron in the alloy which is not oxidized in the film growth diffuses out of the electrodes into the adjacent non-ferromagnetic material as indicated by the B-depleted regions in the electrodes (**b**).

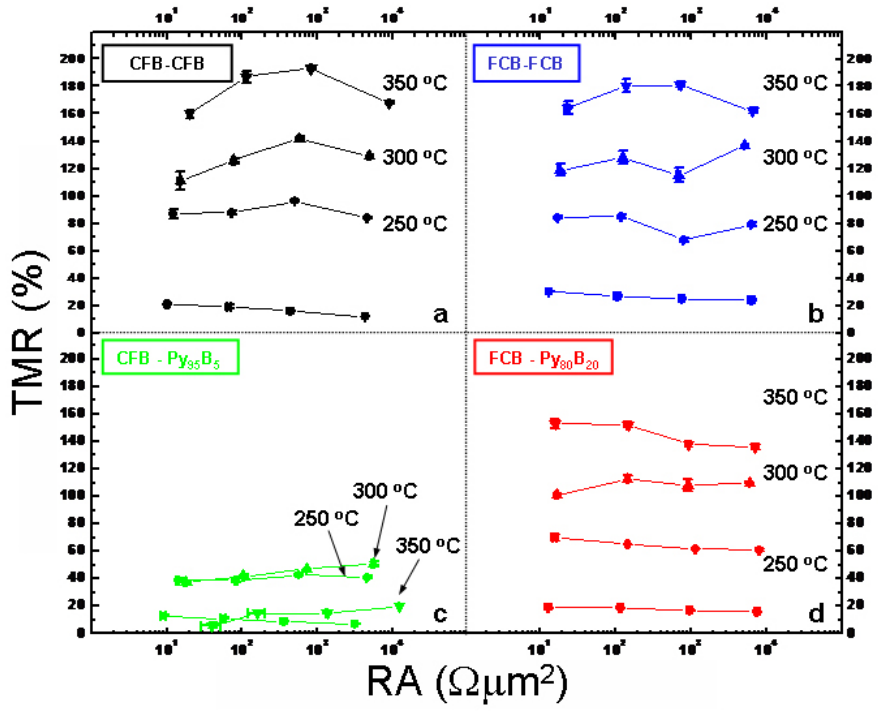

Figure 4.12: Comparison of junction TMR as a function of annealing temperature. Comparative CIPT measurements of MTJ structures showing dependence of TMR versus RA on annealing for (a) all-$Co_{60}Fe_{20}B_{20}$ (CFB) (black) electrodes, (b) all-$Fe_{60}Co_{20}B_{20}$ (FCB) (blue) electrodes, (c) a CFB/Mg-B-O/$Ni_{77}Fe_{18}B_5$ ($Py_{95}B_5$) (green) structure, and (d) a FCB/Mg-B-O/$Ni_{65}Fe_{15}B_{20}$ ($Py_{80}B_{20}$) (red) structure. Error bars represent the standard deviation of multiple CIPT measurements for each data point. Each sample has been measured before (squares) and after annealing to 250 °C (circles), 300 °C (up triangles), and 350 °C (down triangles) as labeled. Maximum TMR values approach 190 % for all-CFB and all-FCB structures while CFB/Mg-B-O/$Py_{95}B_5$ structures achieve small TMR ~ 45 %. FCB/Mg-B-O/$Py_{80}B_{20}$ structures achieve TMR values between 60 and 155 % for various annealing temperatures and show little dependence of TMR upon RA.

top electrode, the TMR increased with the annealing temperature as expected. The junction with the $Ni_{77}Fe_{18}B_5$ top electrode did not produce high TMR. The junctions with a $Ni_{65}Fe_{15}B_5$ free electrode (Figure 4.12d) show TMR that steadily increases with annealing temperature, and increases somewhat with decreasing barrier thickness, with junctions incorporating a $\sim$ 1.1 nm Mg-B-O barrier exhibiting $\sim$ 155 % TMR and low RA ($\sim$ 15 $\Omega\,\mu\,m^2$) after annealing to 350 °C.

We acquired TEM imaging and nanometer spot size convergent beam electron diffraction (CBED) to determine the reasons for the successful use of $Ni_{65}Fe_{15}B_{20}$ as the free electrode in our Mg-B-O junctions and for the less successful results achieved with $Ni_{77}Fe_{18}B_5$. TEM images of the two types of junctions before and after annealing are shown in Figure 4.13. The $\sim$ 1.1 nm Mg-B-O barriers are poly-crystalline in both cases, but the $Ni_{77}Fe_{18}B_5$ and $Ni_{65}Fe_{15}B_{20}$ electrodes exhibit quite different crystal structure. The $Ni_{77}Fe_{18}B_5$ electrode has some texturing in the as-grown case (Figure 4.13**a**), but after annealing to 350 °C, becomes less textured (Figure 4.13**c**), as is clearly indicated by the CBED pattern (Figure 4.13**c** inset). In contrast, the as-deposited $Ni_{65}Fe_{15}B_{20}$ electrode is amorphous (Figure 4.13**b**), as expected for such a high concentration of the glass-forming B component. After annealing to 350 °C, however, the TEM and CBED measurements (Figure 4.13**d** and insert) reveal that it has a highly textured (001) bcc crystal structure, which is optimal according to the theoretical coherent spin-dependent tunneling model.

The low TMR values with the $Ni_{77}Fe_{18}B_5$ free electrode correlate with its low B content. This results in a polycrystalline electrode in the as-deposited case, due to the insufficient amount of the glass forming component, and an even more polycrystalline electrode after annealing. The low B content results in more oxidation of the ferromagnetic components of the NiFeB surface during growth due to reaction with surface

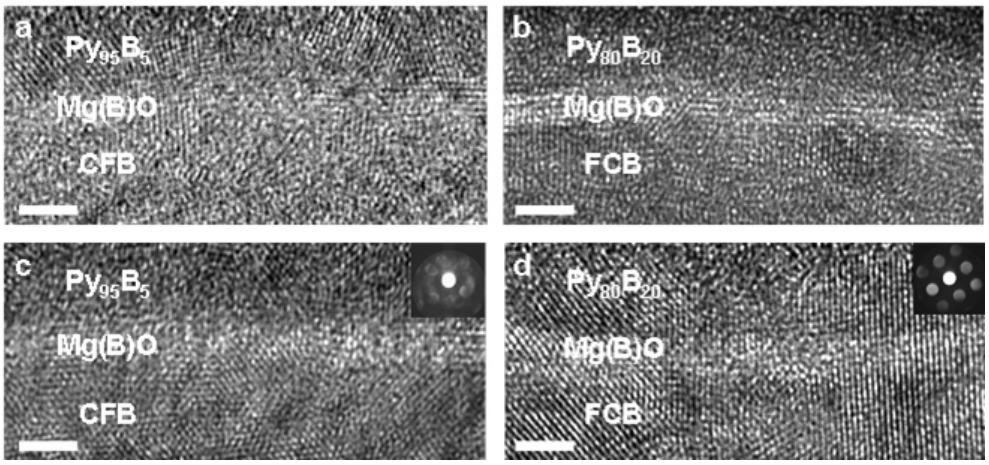

Figure 4.13: Structural investigation of Mg-B-O-based MTJs with NiFeB top electrodes. Cross-sectional bright field TEM images of the as-grown CFB/Mg-B-O/$Py_{95}B_5$ MTJ (a) shows a polycrystalline top electrode and composite Mg-B-O oxide barrier. After annealing (c), the barrier remains polycrystalline while the top electrode appears less textured. In contrast, the as-grown FCB/Mg-B-O/$Py_{80}B_{20}$ MTJ (b) shows an amorphous top electrode and polycrystalline composite Mg-B-O oxide barrier, but after annealing (d), the entire junction shows regions of coherent crystal structure. The scale bar in each of the images is 2 nm. CBED data from the top electrode of the annealed CFB/Mg-B-O/$Py_{95}B_5$ structure (inset in (c)) confirms the electrode is polycrystalline and not well textured. However, CBED data from the top electrode of the annealed CFB/Mg-B-O/$Py_{80}B_{20}$ structure (inset in (d)) has bcc texturing.

oxygen on the MgO barrier. It also results in less BO_3 formation, which beneficially reduces strain on the tunnel barrier upon annealing. In contrast, the use of a more B-rich, and initially amorphous, $Ni_{77}Fe_{18}B_5$ top electrode is successful in forming a (001) textured bcc Py film upon annealing. This material provides sufficient B to both protect the Py components from oxidation and to mix in a significant amount of BO_3 into the top portion of the Mg-B-O barrier during film growth.

4.5 Conclusion

From the study of MgO/CoFeB isolated interfaces via atomic resolution spectroscopic imaging, a Mg-B-O interfacial layer was observed after annealing. Mn, likely oxidized, was also found in the interfacial layer after annealing. In working MTJs where the initial MgO layer was less than 2 nm thick, a hybrid Mg-B-O barrier layer formed. Despite this, a relatively large TMR of $\sim$ 200 % was achieved. $Mg_2B_2O_5$ and $Mg_3B_2O_6$ compounds exist naturally, suggesting that the hybrid Mg-B-O may be more stable than a mixture of MgO and BO_x.[130, 131] The relatively large TMR despite the Mg-B-O formation suggests that MTJs with the hybrid barrier layer are technologically relevant. Elimination of the Mn oxide could lead to higher TMR [119]. Furthermore, by employing $Ni_{65}Fe_{15}B_{20}$ free layers, we have been able to produce MTJs that also show little dependence of TMR upon RA, demonstrating that magnetically soft permalloy electrodes can be successfully incorporated in high performance MTJs for both MRAM and field sensing applications.

CHAPTER 5

NANOSCALE ELECTRON SPECTROSCOPY OF LOCAL OPTICAL DENSITIES OF STATES IN SILICON AND DIAMOND PHOTONIC STRUCTURES OF FINITE SIZES

Spatially-resolved, local photonic densities of states (DOS) of finite silicon and diamond photonic structures in a spectral domain ranging from the ultraviolet to the near-infrared are extracted from monochromated electron energy-loss spectra (EELS) acquired with a sub-5nm electron probe. Retardation effects by relativistic electrons induce radiative losses such as Cherenkov and transition radiation that act as a virtual broadband light source, coupling to the photonic DOS. Through spectroscopic imaging, maps of the resultant energy losses as the electron probe scans across the finite structures are acquired to reveal optical modes with distinct spatial distributions due to different boundary effects. These optical modes are in good agreement with simulated photonic DOS, confirming that EELS can probe optical modes via retardation effects that are absent from a non-relativistic treatment of energy loss mechanisms.

This chapter describes the development of monochromated EELS as a nanometer-scale optical probe for photonic DOS and presents a direct mapping of the electromagnetic field distributions (photonic modes) of finite photonic structures.

5.1 Introduction

Photonic crystals exhibit optical properties characterized by a local electromagnetic density of states (DOS) that is governed by periodic dielectric structures [57]. The local photonic DOS can be significantly modified by sub-wavelength features such as defects in the photonic crystals. For example, perturbing a particular lattice site (i.e. a

point defect) in photonic crystals can spatially confine a mode to dimensions smaller than its wavelength [132]. Conventional optics-based techniques cannot resolve these sub-wavelength optical modes because they are diffraction-limited, resulting in spatial resolution on the order of the probe wavelength, typically a few hundred nanometers. By accessing the information contained in the evanescent modes, near-field scanning optical microscopy (NSOM) [61, 62] overcomes the diffraction limit, but still gives a spatial resolution of tens of nanometers, limited by the tip radius. The limited resolution of optics-based techniques makes electron energy-loss spectroscopy (EELS) combined with scanning transmission electron microscopy (STEM) an attractive alternative because of its superior spatial resolution of 0.1 to 5 nm. Unlike NSOM, which is a surface-sensitive technique, EELS can probe DOS embedded in photonic crystals up to several microns thick as electrons travel through the samples. Furthermore, EELS measures the DOS principally along the direction of the electron trajectory [24], while NSOM measures the DOS principally on the plane of the surface over which it scans [133].

Probing photonic modes with EELS is possible because of radiation generated by relativistic electrons [21, 24]. In the classical regime where radiation is not induced by the electrons, coupling between the electrons and photonic modes is negligible because their wavelengths differ by orders of magnitude. Wavelengths of the probe electrons in electron microscopes are in a sub-nanometer range; for 200 keV electrons, the corresponding wavelength is 0.0251 Å [134]. In contrast, wavelengths of photonic modes generated in photonic crystals are typically in the range of tens or hundreds of nanometers. Hence, the overlap between the probe electrons and the photonic modes is very small. This means that, in the classical regime where the dielectric response of a sample to an electric field induced by electrons is instantaneous, the probe electrons will not couple to the photonic modes significantly enough to produce meaningful EELS signals.

In the relativistic regime where the speed of electrons travelling in or near a dielectric medium is faster than the speed of light in the medium due to a high index of refraction, retardation effects cause a series of radiative losses, one of which is Cherenkov radiation [12]. Even when the speed of electrons does not exceed the speed of light, transition radiation can be emitted if the electrons or their image charges pass through discontinuities in dielectric properties rapidly [13, 23, 25]. For silicon, these radiative losses are expected below the direct electronic transition at 3.4 eV and into the near-infrared range. Both Cherenkov and transition radiation can be considered as a virtual light source [21] because they cover a broad spectrum, ranging from infrared to ultraviolet frequency (0.7 - 3.4 eV). This virtual broadband light source allows EELS to couple to photonic DOS and be used as a probe to investigate photonic crystals at nanometer resolution [22, 135–139].

With developments in monochromators [16–18] and system stability, energy resolution of EELS has improved to reach 100 meV which is comparable to $\sim$ 30 nm spectral resolution in the visible frequencies, a good enough spectral resolution for probing photonic modes. The advantage of using EELS in studying photonic structures is the nanometer resolution of electron microscopes, which allows a direct mapping of the photonic DOS, locally affected by defects. Another important benefit of monochromated EELS is the ability to probe the high-wavelength optical domain, including the important telecom wavelength of 1.5 μm, in addition to a broad spectral range extending down to x-ray wavelengths.

5.2 Methods

Local photonic DOS of various silicon and diamond photonic structures of finite sizes were probed using monochromated EELS at nanometer resolution. Two-dimensional photonic structures were fabricated using a focused ion beam, which milled periodic patterns extending over a few microns onto diamond and silicon slabs with $\sim$ 10 nm precision milling. Monochromated electrons with 200 keV incident energy (from a Tecnai F20 equipped with a monochromator) at 110 - 140 meV energy resolution were used to generate radiation which coupled to and probed the local DOS of the photonic structures. Using EEL spectroscopic images, distinct spatial distributions of the photonic modes were mapped. For EELS calculations, a local dielectric theory including retardation effects by relativistic electrons [140–142] and the MIT PB package [143], which calculates eigen-modes of photonic crystals, were used.

The local dielectric theory with a retardation treatment [141] and a photonic band structure calculation package [143], MIT PB, are discussed here. Also, a brief description of a monochromator equipped in Tecnai F20 microscopes is given in this section. The fabrication of finite-size silicon and diamond photonic structures is described in Appendix B in a step-by-step fashion.

5.2.1 Local dielectric theory with a retardation treatment

Electron energy-loss spectroscopy as a probe for photonic DOS is possible via retardation effects. When the fast electrons in electron microscopes travel through or near a dielectric material, a time-varying dipole response is induced in the material. Because the speed of 200 keV electrons reaches $\sim$70% of the speed of light in vacuum,

the time-varying dipole cannot adiabatically follow the electric field induced by the fast electrons, resulting in radiation. Consequently, a classical dielectric theory cannot be used in this case because the dipole response is instantaneous in the classical dielectric theory. A dielectric theory which includes the full retardation effects is needed. Analytical solutions to a dielectric theory which includes retardation effects exist for simple geometries: a two-dimensional slab [140], an infinite interface [144] and a multi-layer geometry for parallel and normal incidence [141, 142]. The solutions for an infinite interface and a multi-layer geometry with parallel incidence were implemented in MATLAB so that experimental EELS results from the same geometry could be compared to the theory. Figure 5.1 shows the geometry of the multi-layer system where the electrons pass through the m^{th} layer in parallel incidence. Each layer is specified by its frequency-dependent, complex index of refraction [145] and the width of each layer is also specified. For a diamond slab shown in Figure 5.6, the multi-layer geometry was used to simulate EELS.

A general approach to calculating the energy loss probability from the dielectric theory with relativistic electrons is briefly discussed here. The electric field generated by a charged particle (in this case, the probe electron) traveling at speed v in or near a dielectric medium with a known geometry can be obtained by solving Maxwell's equation with given boundary conditions. If the electron travels along the **x** axis, then the energy loss per unit path length $\frac{dW}{dx}$ is equivalent to the retarding force exerted on the electron in the **x** direction which gives,

$$-\frac{dW}{dx} = -eE_x(vt, y, z, t), \tag{5.1}$$

where y and z are Cartesian coordinates and t denotes time. We can relate $\frac{dW}{dx}$ to the energy loss probability at frequency ω per unit length and per unit frequency by,

$$\frac{dW}{dx} = \int_0^\infty \hbar\omega \frac{d^2P}{dxd\omega} d\omega. \tag{5.2}$$

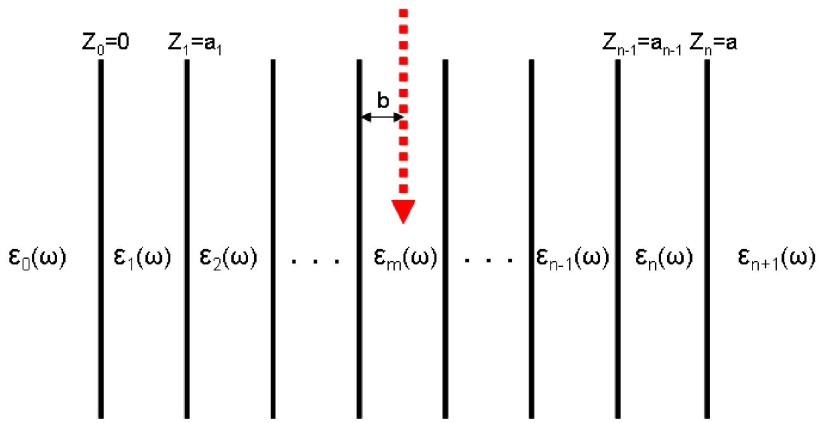

Figure 5.1: Multi-layer geometry for parallel incidence of fast electrons. In this geometry, the fast electrons travel in parallel to the layer interfaces where the layers are infinitely thick in the direction of the electrons' trajectory and also extend to infinity in planes. The red dotted arrow indicates the electron path. The analytical solution of this geometry by Chen *et al.* [141, 142] is implemented for comparison with experimental data.

The low energy-loss EELS results are compared with $\frac{d^2P}{dxd\omega}$ in Equation 5.2. Exact solutions of $\frac{d^2P}{dxd\omega}$ for simple geometries are given by Kroger [140], Garcia-Molina *et al.* [144], and Bolton *et al.* [141, 142].

5.2.2 MIT-PB code

To compare the low energy-loss EELS results with photonic DOS of more complicated dielectric structures, MIT Photonic Bands was used. MIT Photonic Bands is a software package developed by S. G. Johnson and J. D. Joannopoulos [143] and it computes eigen-frequencies of periodic dielectric structures in the frequency domain. The software package and the technical manual can be downloaded freely from the MIT Photonic Bands web page [146].

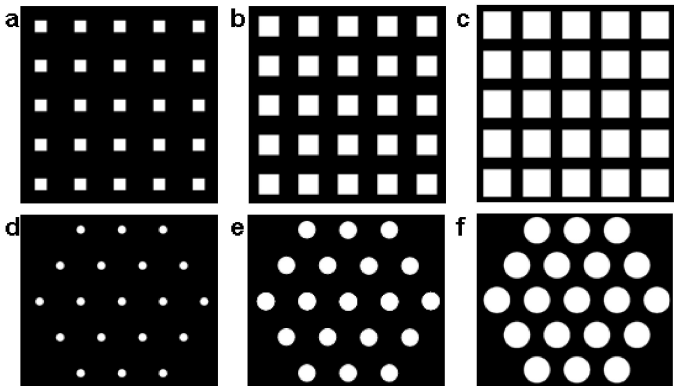

Figure 5.2: Silicon photonic structures for MIT-PB simulation. **a** - **c** show rectangular holes on a square lattice while **d** - **f** show cylindrical holes on a triangular lattice. Let D denote the center-to-center distance between two holes. Then, the widths of the rectangular holes are $0.3D$ in **a**; $0.5D$ in **b**; and $0.7D$ in **c**. The radii of the cylindrical holes are $0.1D$ in **d**; $0.2D$ in **e**; and $0.33D$ in **f**.

To compute the photonic DOS, a periodic dielectric structure was created by specifying the index of refraction as a function of position. The structures simulated using the MIT-PB code, depicted in Figure 5.2, are silicon with arrays of empty holes, where an index of refraction of 3.42 was used to approximately match results for silicon at wavelengths above 700 nm. In particular, the structures in Figure 5.2 **c** and **f** were studied experimentally and the results are shown in Figure 5.8, 5.9, 5.10 and 5.11, which are discussed later in the chapter. To reduce the simulation time, the structures were assumed to be infinitely thick and their periodicity extended to infinity.

Adequate sampling in reciprocal or **k** space is important for computing the DOS accurately from photonic band calculations. Calculating the eigen-frequencies along a few principal axes in Brillouin zone does not result in a truely representative DOS due to significant under-sampling. Special k-points in Brillouin zone can be selected to economically compute the DOS [147, 148]. However the most brute force approach

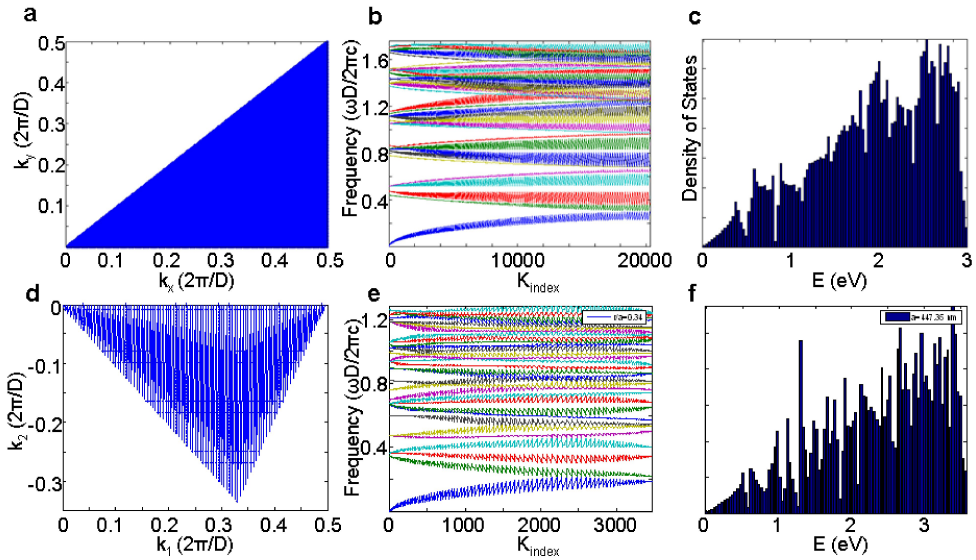

Figure 5.3: MIT-PB simulation for the structures shown in Figure 5.2. The simulation for the rectangular holes on a square grid is shown in **a** - **c**. The width of the square in this case is $0.8D$ where D denotes the center-to-center distance between two squares. The k-sampling in the irreducible Brillouin zone is shown in **a**. **b** shows the simulated eigen-frequencies at all sampled k-points. **c** shows the DOS obtained from **b**. **d** - **f** show the simulation for the cylindrical holes on a triangular grid where the radius of the cylindrical holes is $0.34D$. **d** shows the irreducible Brillouin zone for a triangular lattice, **e** shows the simulated eigen-frequencies, and **f** shows the corresponding density of states.

is taken here: heavily sampling k-points in the irreducible Brillouin zone. The number of sampled k-points was increased until the calculation converged. In the first approximation, the photonic DOS can be obtained by simply performing a histogram on the simulated eigen-frequencies. Figure 5.3 shows the simulation results for photonic structures of a rectangular lattice and a triangular lattice, shown in Figure 5.2. Figure 5.3**a** and **d** show the sampled k-points in the irreducible Brilluoin zone of the rectangular and the triangular lattice, where D is the lattice constant in real space. Figure 5.3**b** and **e** show simulated photonic bands for a structure of rectangular holes on a square grid and

a structure of cylindrical holes on a triangular grid respectively. The photonic DOS of the two structures are shown in Figure 5.3**c** and **f**, obtained from the photonic bands. Interpretation of the simulation results will be discussed in Section 5.3 after comparison with experiments.

5.2.3 Monochromated EELS

To resolve the photonic modes using EELS, it was necessary to operate the microscope in monochromated mode. In the normal operating mode of the microscope, the full width at half maximum (FWHM) of the zero-loss peak is ~ 0.5 eV when the spectrum is acquired at the dispersion setting of 0.01 eV per channel. Despite the relatively small FWHM of ~ 0.5 eV, distinguishing peaks below ~ 1.5 eV is difficult because of the large contribution in intensity from the tail of the zero-loss peak. The tail intensity of the zero-loss peak in normal mode contributes significantly to the spectrum in the low energy-loss region (0.5 eV – 3.4 eV). A monochromator not only greatly improves the energy resolution, but also results in significantly reduced intensity in the zero-loss peak tail.

A monochromator in its simplest form is an energy filter that selects electrons with a narrow energy spread. A Wien filter with an energy-selecting slit is used to achieve this goal in Tecnai F20's. The Wien filter applies an electric and a magnetic field which are perpendicular to each other. Electrons travelling at different velocities due to their thermal spread will have different trajectories upon entering the Wien filter. This effectively spreads the electrons in space according to their energies. By placing an energy-selecting slit after the Wien filter, the energy spread of the electrons after the slit is minimized. Figure 5.4 shows the schematic diagram of electron trajectories when the

monochromator is on in a Tecnai F20. More detailed explanations of the monochromator and Wien filter can be found in the FEI manual by P. Teimeijer [149] and Egerton's EELS book [9].

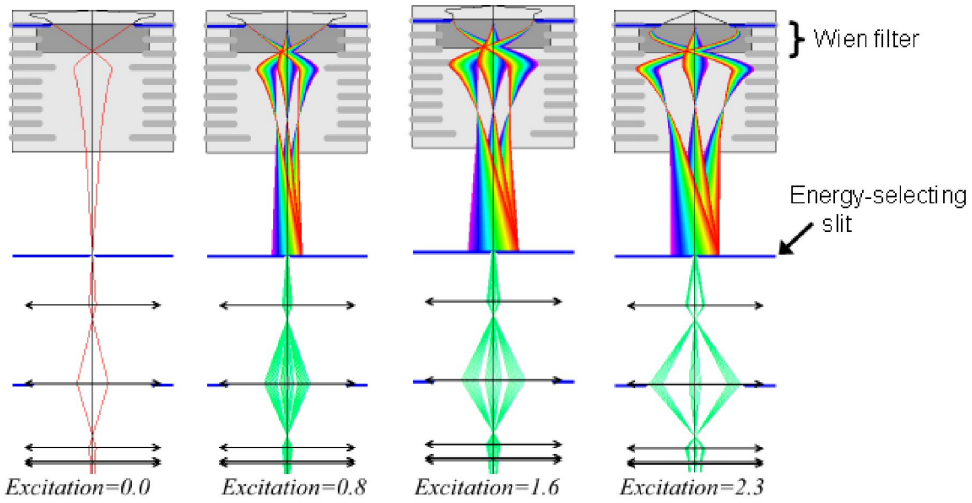

Figure 5.4: Electron trajectories with the monochromator on in a Tecnai F20. Electrons are spread according to their velocities (i.e. thermal spread) after the Wien filter. The energy-selecting slit chooses electrons which travel at a specified velocity. The diagram is reproduced from the FEI manual by P. Tiemeijer [149].

In monochromated mode, the FWHM of the zero-loss peak is ~ 0.1 eV (acquired at the dispersion setting of 0.01 eV per channel), which is a factor of five times improvement compared to the normal operating mode. Figure 5.5 compares the zero-loss peaks obtained in normal and monochromated mode. A detailed monochromator procedure can be found in the FEI manual [149] and Yurtsever's thesis [26].

Practical Considerations for Good Signal-to-Noise Ratio. To increase the signal-to-noise ratio in EEL spectra, a longer acquisition time is usually sufficient. In the low energy-loss region however, a longer acquisition cannot be achieved without risking saturation and possible damage to the charge-coupled device (CCD) camera due to the

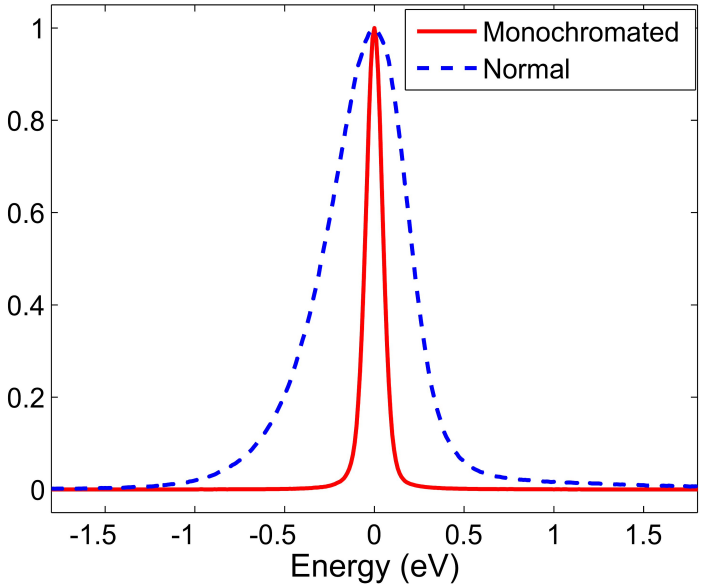

Figure 5.5: Zero energy-loss peak in monochromated versus normal mode. The energy resolution improves by a factor of five by going into the monochromated mode. Spatial resolution in STEM degrades to ~ 1-5 nm to achieve this energy resolution. The intensity reduces considerably in monochromated mode because most of the electrons are filtered out in the monochromator.

intense zero-loss peak. Instead of a longer acquisition time, multiple spectra at a short acquisition time (~ 0.1 second) can be acquired and summed for a higher signal-to-noise ratio. This will avoid saturation but not damage (which is based on dose). However, a voltage instability in which the zero-loss peak jumps around by 0.1 eV in ~ 1-2 second intervals was sometimes observed, preventing a simple cumulative acquisition of spectra. Ks-EELS installed in Digital Micrograph was used to overcome the voltage instability. It acquires multiple spectra sequentially, saves them in a single file, and has a capability to post-align the spectra by several methods such as cross-correlation and maximum value finding. Disadvantages in using Ks-EELS are: first, the acquisition time is long (~ 10 seconds for 10 spectra); second, the files are large (~ 20 Mega-bytes);

and lastly an automated spectroscopic image which contains many pixels is not possible. Another way to increase the signal-to-noise ratio is to block the intense zero-loss peak by inserting a slit. Because the zero-loss peak is blocked, saturating or damaging the CCD camera is not a concern. The signal-to-noise ratio can then be improved by increasing the intensity of the signal with the monochromator x-shift or by acquiring the spectrum longer. The disadvantage in this case is that a precise energy calibration is difficult. Because the zero-loss peak is blocked, there are no obvious features to calibrate the energy-loss axis unless the spectrum has a clear, sharp peak at a known energy-loss value. Taking a spectrum that includes the zero-loss peak at a short acquisition time and cross-correlating it with the spectrum with the slit inserted can be a way to calibrate the energy axis.

5.3 Results and Discussions

A 2 micron-thick diamond film (free supply from Sp3 Diamond Technologies Inc. Santa Clara CA) was initially investigated to confirm that radiative losses could be detected for incident electrons with kinetic energy of 200 keV. Figure 5.6a shows an EEL spectrum taken at $\sim$ 10 nm away from the diamond film in aloof geometry (white dot in Figure 5.6a inset) and calculated EEL spectra using a local dielectric theory in both classical and relativistic regime [141, 144]. In the classical regime, there should be no energy-loss mechanisms below 5.5 eV, which is the electronic band gap of diamond [150]. This can be easily checked by examining the imaginary part of the index of refraction of diamond, which is shown in Figure 5.7. The imaginary part of the index of refraction of diamond is zero below the band gap, indicating that there should be no absorption below the band gap. The calculated EELS in the classical regime (solid line in Figure 5.6a) indeed shows no signal in the energy-loss region below 5.5 eV. However the exper-

imental EEL spectrum shows significant intensity below the band gap of diamond that cannot be accounted for by the extension of the zero-loss peak intensity. A calculated EEL spectrum using a retardation treatment (dotted line in Figure 5.6a) confirms that the intensity below the band gap is due to the emitted radiation.

If boundary conditions are imposed on the emitted, virtual light source (radiation), only those modes whose frequencies satisfy the boundary conditions will be supported. These eigen-modes will appear as sharp peaks in EELS. Figure 5.6b shows an EEL spectrum taken near a diamond waveguide where a rectangular slit was milled with a focused ion beam. The width and the thickness of the waveguide are $\sim$ 165 nm and 2 micron. The white dot in the Figure 5.6b inset indicates the location at which the EEL spectrum was taken, which was $\sim$ 10 nm away from the waveguide. The spectrum shows two distinct peaks at 1.5 eV and 3.7 eV, which correspond to two modes whose frequencies are supported by the waveguide. To compare with the experiment, an EEL spectrum $\sim$ 10 nm away from the 165 nm-wide diamond waveguide was simulated using a local dielectric theory with retardation effects [141]. For simulation, the waveguide was assumed to be infinite in its thickness and length for simplicity. The energies of the experimentally observed peaks agree well with the simulated EEL spectrum. Only the two lowest energy peaks were resolved in the experiment while four peaks were distinctly produced in the simulation. This is likely due to the finite size and roughness of the waveguide in experiment, for which higher frequency modes would easily lose coherence and damp out. When EELS was taken beside a semi-interface film (square in Figure 5.6c inset), a continuous intensity was observed in the spectrum below the band gap of diamond, both experimentally and theoretically (squares and dotted line in Figure 5.6c). This is because all frequency modes should be supported for a continuous medium.

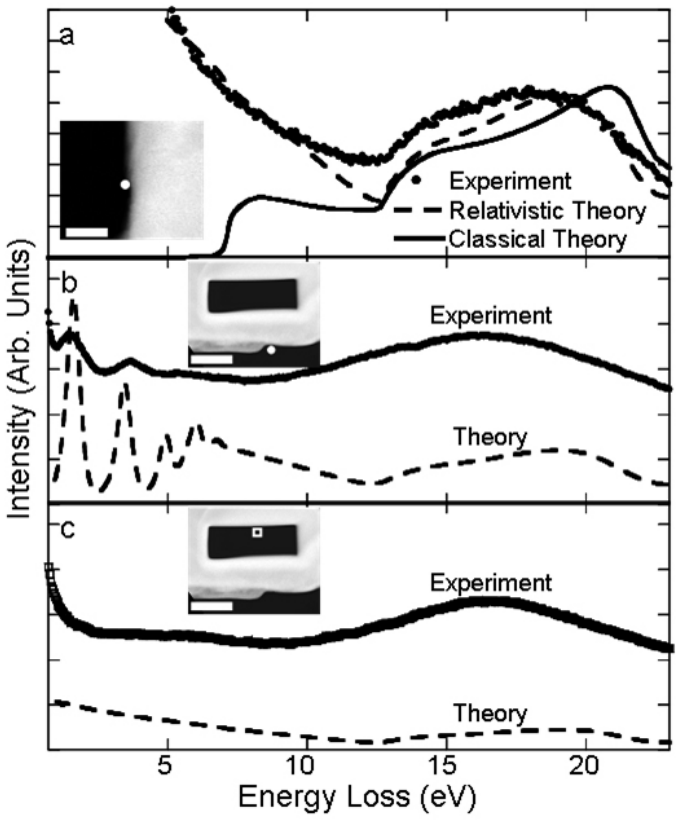

Figure 5.6: Electron energy-loss spectra near a diamond film and waveguide. Relativistic electrons traveling near a 2 micron-thick diamond film generate radiative losses as shown by the significant intensities in the experimental spectrum (dots in (a)) below the band gap of diamond. The dotted and solid line in (a) represent simulated spectra in relativistic and classical regime. The inset in (a) shows the diamond film and the location of the electron probe (white dot). When boundary conditions are provided such as the rectangular waveguide (inset in (b)), peaks appear in the spectrum (dots in (b), taken $\sim$ 10 nm away from the waveguide). The dotted line in (b) represents a simulated spectrum in relativistic regime. For the simulation, electrons pass 10 nm away from the waveguide. When the boundary conditions are removed, as in the case in (c) where electrons pass near semi-infinite film, the peaks disappear in the spectrum (squares in (c)). The dotted line is a simulated spectrum under the same experimental condition. The scale bars for insets are 200 nm.

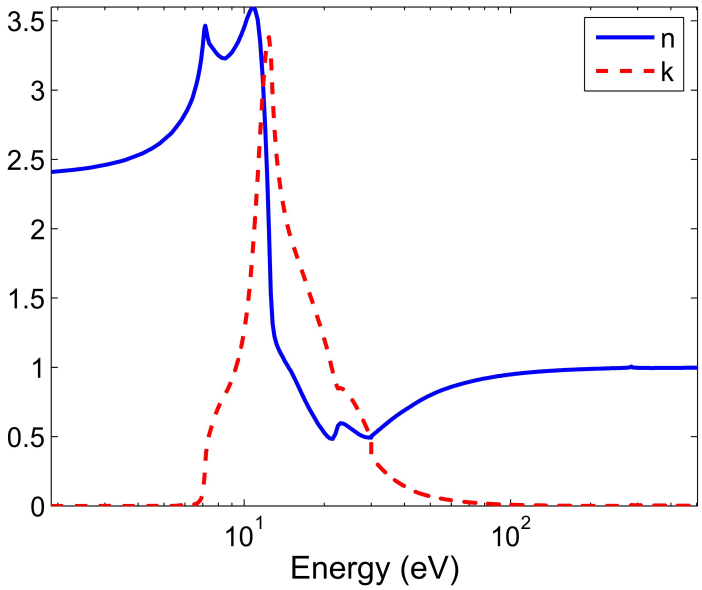

Figure 5.7: Index of refraction of diamond. The solid and dotted lines indicate the real and imaginary part of the index of refraction of diamond.

With a simple, one-dimensional waveguide structure, we confirmed that monochromated EELS could probe photonic DOS. To show that peaks observed in EELS were indeed due to the geometry of photonic structures, more complicated, two-dimensional photonic structures were investigated. Silicon photonic structures of finite sizes, where hollow cylinders were arranged in a triangular lattice grid, were fabricated. Figure 5.8 a-c show three silicon photonic structures with r/a = 0.20, 0.27, and 0.34 where r is the radius of the hollow cylinders and a is the lattice constant, the distance between two cylinders. The lattice constant was $\sim$ 447 nm for all three photonic structures. The radius of the cylinders, r, was varied to observe how the photonic modes would shift in frequencies with different r/a ratios. Probing photonic modes of small, finite structures is straightforward with EELS due to the focused electron beam, which couples to photonic DOS locally.

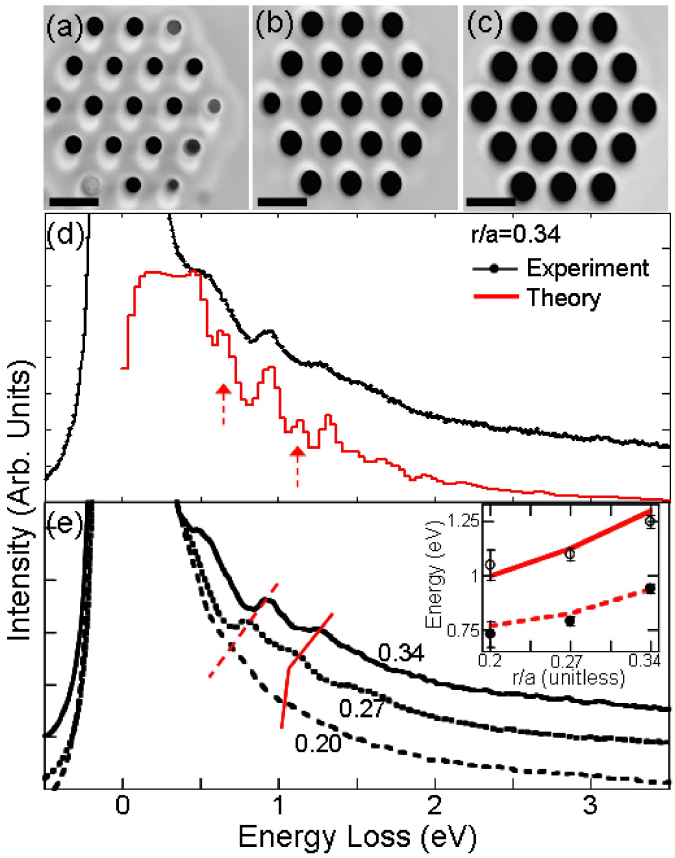

Figure 5.8: Silicon photonic structures of cylindrical holes on a triangular lattice grid. (a-c) show photonic structures with r/a = 0.20, 0.27, and 0.34 respectively where r is the radius of the holes and a is the lattice constant. The scale bars in (a-c) are 500 nm. (d) shows an EEL spectrum taken from the central cylinder of the structure with r/a = 0.34 in aloof mode (black curve) and a simulated photonic DOS of the same structure (red staircase). The arrows indicate simulated modes that are not resolved experimentally. (e) shows shifts in the photonic modes when r/a is varied. The solid, the short dotted, and the long dotted curves are spectra taken from r/a = 0.34, 0.27, and 0.20 respectively. The dotted and solid vertical lines (in red) are a visual guide to indicate the energy shifts in the photonic modes. The inset in (e) shows the agreement between the experimentally observed shifts in the photonic modes near 0.9 eV and 1.3 eV (filled and open circles) and the simulated photonic DOS (solid and dotted lines).

Figure 5.8d shows an EEL spectrum taken from the photonic structure with r/a=0.4 and a simulated photonic DOS of the same structure using the MIT-PB code [143]. For simulation, the photonic structure was assumed to be infinitely thick and to have infinite lateral extent, which reduced the simulation time. Three distinct modes, at ~ 0.5 eV, 0.94 eV and 1.26 eV, were observed experimentally while two extra modes appear in the simulated photonic DOS, indicated by the dotted arrows. These extra modes were not resolved experimentally, principally due to the low experimental energy resolution. When the simulated DOS was binned at the experimental energy resolution of ~ 0.1 eV, the extra modes could not be resolved, resulting in a DOS that matched the experimental spectrum well. It should be noted that the simulated photonic DOS was multiplied by the evanescent decay of the time-varying electric field, $[K_0(bnE/\gamma\hbar\, c)]^2$ where K_0 is the zeroth order modified Bessel function of the second kind, b is the impact parameter (the distance between the probe electron and the dielectric medium), n is the index of refraction of the material, E is the energy loss, γ is the relativistic factor, $\hbar$ is the Planck's constant, and c is the speed of light in vacuum [25]. For the simulation, b was 70 nm and n was 3.44.

Figure 5.8e shows EEL spectra acquired from the silicon photonic structures of various r/a ratios - 0.27, 0.3, and 0.34, which are shown in Figure 5.8a-c respectively. The spectra were acquired from the hollow cylinder located at the center of the photonic structures in aloof geometry. As expected, the characteristic mode frequencies (i.e. the characteristic energy losses for photonic modes) shifted systematically when r/a was varied. Two modes above 0.5 eV were examined carefully (the exact energy loss of the mode at ~ 0.5 eV was difficult to determine due to the contribution from the zero-loss peak tail). The hollow and solid dots in the Figure 5.8e inset correspond to the energy losses of the two modes observed experimentally. The solid and dotted lines in the inset correspond to the simulated energy levels of the two modes, which agree well with the

experiments. The good agreement in the energy location of the two modes between the experimental EELS and the simulated photonic DOS confirms that EELS can be used to probe photonic DOS directly.

A significant advantage of monochromated EELS for probing the local photonic DOS is the nanometer spatial resolution, which allows a direct mapping of the spatial distribution of photonic modes. A photonic structure with hollow squares positioned on a square grid was created to probe this spatial distribution. Figure 5.9a shows the photonic structure where the squares are 600 nm wide and the center-to-center distance between the squares is 800 nm. To probe the spatial distribution of the photonic modes, a 64 x 64 pixel spectroscopic image was acquired, where each pixel contains an EEL spectrum [125, 151]. A subset of the EEL spectra from the spectroscopic image is shown in Figure 5.9b. The spectra were chosen from the top side of the central square and, to increase the clarity of the modes, we used the Richardson-Lucy method [152, 153] to deconvolve the spectra with the zero-loss peak acquired in vacuum under the same acquisition condition.

We observe that the first mode at $\sim$ 0.5 eV has higher intensity at the corners of the square, as shown by the top and bottom spectra in solid line, while the second mode at $\sim$ 0.9 eV has higher intensity at the sides of the square as shown by the middle, dotted spectrum. The intensity under the two modes was integrated to create intensity maps, which are shown in Figure 5.9c and d respectively. As suggested by individual EEL spectra shown in Figure 5.9b, the integrated intensity map of the first mode is higher at the four corners of the central square (Figure 5.9c) while the integrated intensity map of the second mode is higher at the sides of the central square (Figure 5.9d). Line profiles across the bottom side of the central square are shown in Figure 5.9e and f, which again clearly show the corner and the side symmetry of the two modes.

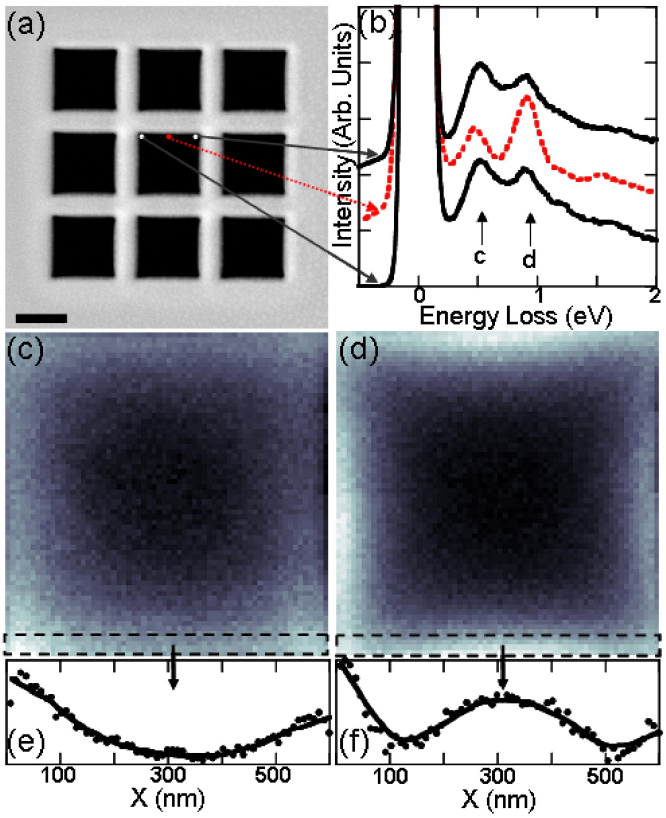

Figure 5.9: Spectroscopic image showing spatial distributions of photonic modes in a photonic structure of hollow squares on a square lattice grid. (a) shows the silicon photonic structure where the hollow squares are 600 nm wide and the lattice constant is 800 nm. The scale bar in (a) is 500 nm. The 64x64 pixel spectroscopic image was taken from the central square. Spectra near the top side of the central square are selectively shown in (b). Using Richardson-Lucy method, spectra are deconvolved with the zero-loss peak, acquired in vacuum under the same experimental conditions, and are displayed with an offset for visual clarity. The areas under the first peak at 0.47 eV and the second peak at 0.9 eV are integrated to create intensity maps, which are shown in (c) and (d). The integrated intensity maps show that the first peak corresponds to a corner mode while the second peak corresponds to a side mode. (e) and (f) are line profiles, averaged over three lines, obtained from (c) and (d) respectively.

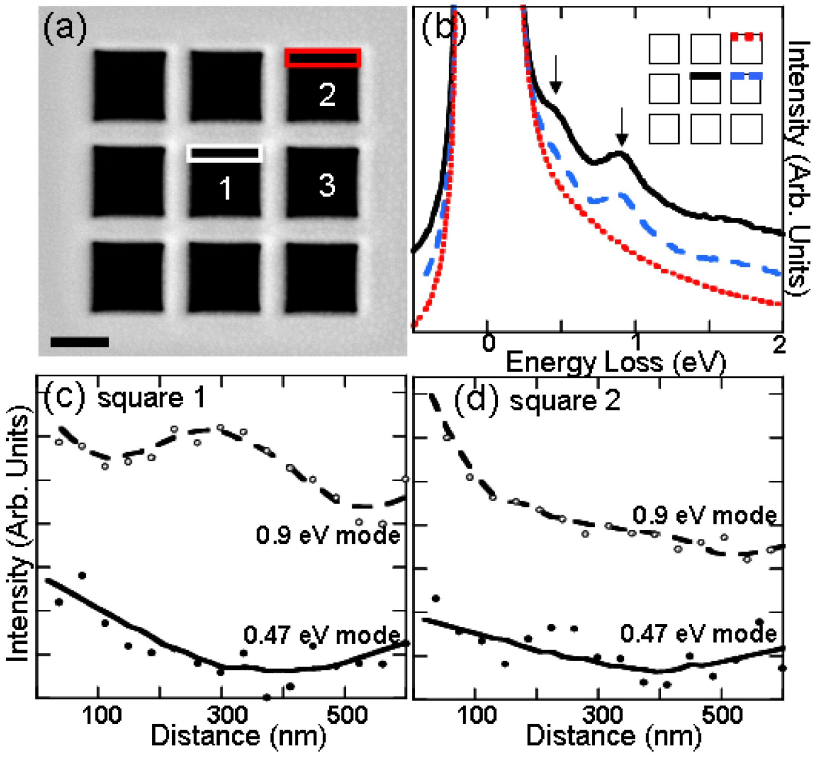

Figure 5.10: Damped photonic modes near the edge of the photonic structure. (a) shows a silicon photonic structure with hollow squares placed on a square grid. The scale bar is 500 nm. (b) shows EELS taken from the top side of squares. Spectrum in solid black is from the central square (square1); spectrum in short, dotted red is from the top, right square (square2); and spectrum in long, dotted blue is from the middle, right square (square3). Spectra in (b) are displayed with an offset for visual clarity and they are not deconvolved with the zero-loss peak. The intensity under the two modes at 0.5 eV and 0.9 eV (indicated by arrows in (b)) was integrated over the top side of square1 and square2. (c) and (d) show the line profiles of the integrated intensities of the two modes from square1 and square 2 respectively. The boxes in (a) indicate where the line profiles were acquired.

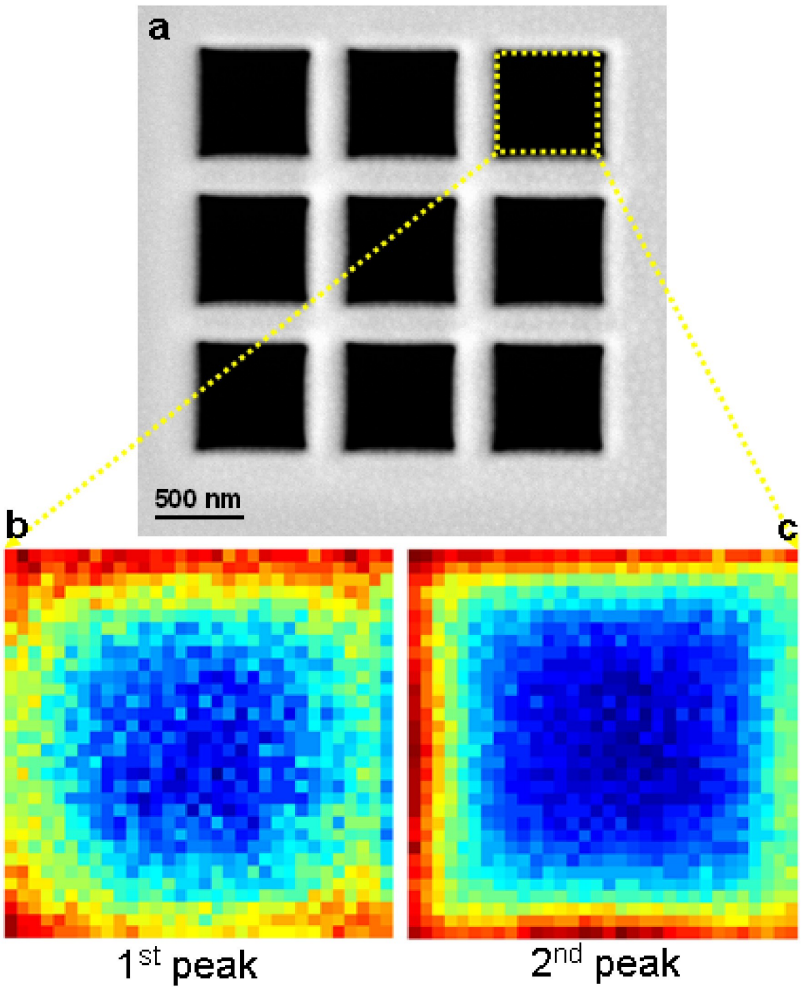

Figure 5.11: Lost symmetry of the photonic modes due to the edge effect. At the top side of the square (yellow, dotted box), which is the edge of the photonic structure, the corner (a) and the side (b) modes have lost their spatial symmetry. A false color scheme is applied for visual clarity. Blue indicates the lowest intensity value while the red indicates the highest.

The ability to probe the photonic modes at nanometer resolution means that a localized defect mode or edge effects due to the finite size of photonic structures can be studied experimentally. In photonic structures with periodicity extending over only a finite region, it would be interesting to observe how the photonic modes damp out near the edge of the photonic structures. The photonic modes expected in a finite-size photonic structure would be analogous to the discrete number of wavefunctions allowed for a particle-in-a-box situation, where the wavefunctions damp out at the edges of the box due to the boundary conditions. To observe this, we acquired spectroscopic images of 64x 64 pixels of three squares labeled box 1, 2, and 3 in Figure 5.10a, which are the central square, the top right square, and the middle, right square. Figure 5.10b shows the EEL spectra, summed over the pixels that make up the top side of the squares from the spectroscopic images. For the central square, the modes at 0.47 eV and 0.9 eV are expected on all sides. However, for the top right square and the middle, right square, the modes are expected to damp out at sides where the periodicity of the photonic structure stops. As expected, Figure 5.10b shows that the photonic modes are not supported at the top side of the top right square (box 2). Figure 5.10c and d show that the symmetry of the corner and the side mode, acquired from the integrated intensity maps, is lost in the top, right square compared to the central square. Figure 5.11 shows the intensity map of the first and the second peak obtained from the spectroscopic image of the top right square (box 2). From Figure 5.11b, it is observed that the two corners on the top side do not show higher intensities whereas the two corners on the bottom side still show higher intensities. Therefore, Figure 5.11b shows that the symmetry of the corner mode is lost on the top side where the periodicity of the structure ends. Figure 5.11c shows a similar result, where the side mode loses its symmetry on the top side while the symmetry is still maintained in the bottom.

5.4 Conclusion

In summary, the coupling between the emitted radiation due to relativistic electrons and the photonic DOS of photonic structures allows for a direct investigation of optical eigen-modes with a nanoscale resolution by monochromated EELS. Several photonic structures were investigated using monochromated EELS, in which photonic modes emerged as peaks. The experimental results agree well with simulated photonic DOS to confirm that the observed spectral features in EELS directly reflect the photonic DOS. A key strength of EELS for probing photonic structures is the spatial resolution achievable in electron microscopes. By acquiring spectroscopic images, distinct spatial distributions of photonic modes were observed on the nanometer scale. Future work includes studying localized linear and point defect modes in photonic crystals, further exploring the finite size effects on photonic modes, as well as extending this approach into the fields of metamaterials.

CHAPTER 6

CONCLUSION

In this thesis, I used spatially-resolved EELS combined with (S)TEM and electron tomography to investigate how nano-scale interfaces would influence local electronic, chemical, and photonic densities of states of nano-scale systems. In particular, I examined three systems: carbon nanotubes in contact with various metals; Mg-B-O-based MTJs; and finite size silicon photonic structures. A summary of each chapter is given here. Suggestions and plans for future work in the Mg-B-O-based MTJ project and the low-loss EELS of photonic structures are also provided here.

6.1 Summary

In Chapter 1, I described what core- and low-loss EELS, which were the primary experimental tool for my thesis, can measure. Core-loss EELS provides information on the local, angular-momentum-resolved electronic density of states in the conduction band by collecting the transmitted, inelastically scattered incident electrons, which undergo energy losses by exciting target electrons bound at the core levels of the sample in a dipole-dominated transition. In discussing low-loss EELS, I focused on relativistic electrons which induce radiative losses such as Cherenkov and transition radiation. I described how monochromated EELS could be used as a nanometer-size probe for photonic densities of states through these types of radiation.

In Chapter 2, I used ADF-STEM electron tomography to reconstruct the three-dimensional contact geometry between carbon nanotubes and various metal contacts, from islanding to wetting contacts. From tomographic reconstructions, I found that islanding metals, whose free surface energies were high and binding energy to carbon

was low, deformed nanotubes radially. Gold, gold-palladium alloy, and pure palladium were found to form islands on the nanotubes. I found that titanium wetted the nanotubes due to the high binding energy of titanium to carbon. By balancing energy terms that were involved in the nanotube-metal contact (deformation energy of the nanotube, surface free energy of the metal, and the contact surface energy between the nanotube and the metal), I confirmed that gold and palladium would island on nanotubes, resulting in deformation of the nanotubes, while titanium would wet the tubes, preserving the shape of the nanotubes. Using spatially-resolved, core-loss EELS, I investigated the effect of nanotube deformation on the electronic properties of the nanotube. Comparing carbon K EELS edges obtained from the pristine and deformed regions of the nanotubes yielded evidence that deformation modified the band structure of nanotubes because the fine structure of the C-K edge obtained from the deformed region of the tube deviated from that obtained from the pristine region of the tube. However, the observed fine structure change in the C-K edge could not be considered a definitive proof of a modified band structure upon nanotube deformation, due to contamination issues which also produced apparent changes in the fine structure of the C-K edge.

In Chapter 3, I described the first part of my work on MgO-based MTJs, which I investigated using spatially-resolved EELS in collaboration with John Read from Buhrman group at Cornell. From electron spectroscopy I found that, in rf-sputtered MgO-based MTJ systems, B from the CoFeB electrodes diffused into the MgO layer and formed BO_x. In contrast, e-beam evaporated MgO layers did not show B diffusion into the MgO. In rf-sputtered MgO-based MTJs, inserting a Mg underlayer between the MgO barrier and the CoFeB base electrode suppressed the formation of BO_x because the Mg underlayer acted as an oxygen sink, pulling oxygens away from B during annealing. However, the Mg-B-O MTJs that included a Mg underlayer produced high RA product values, which is not desirable for spin-transfer-torque MTJ devices.

In Chapter 4, I described the spatial distribution of the BO_x in the Mg-B-O-based MTJs and discussed how relatively high tunneling magnetoresistance (TMR) was obtained with the Mg-B-O barrier layer. Using spectroscopic imaging, I found that the BO_x found within the MgO layer was uniformly distributed throughout the MgO layer. Scanning tunneling spectrospoicy and x-ray photoemission spectroscopy data suggested that upon annealing, a hybrid Mg-B-O layer formed. TMR and RA products of Mg-B-O tunnel junctions with a varying thickness of the tunnel barrier and different electrodes ($Co_{60}Fe_{20}B_{20}$, $Fe_{60}Co_{20}B_{20}$, $Ni_{65}Fe_{15}B_{20}$, and $Ni_{77}Fe_{18}B_5$) were measured using the current in-plane tunneling technique. Despite the formation of Mg-B-O, which is a complete deviation from the theoretical model of epitaxial Fe/MgO/Fe required for high TMR, TMR between 160 % and 200 % was achieved in the Mg-B-O-based MTJs. Furthermore, a low RA product of $\sim 15\ \Omega\ \mu m^2$ was achieved for a thin ($\sim$ 1 nm) Mg-B-O tunnel barrier. Permalloy alloyed with a large concentration of B ($Ni_{65}Fe_{15}B_{20}$) was successfully used as a free electrode to produce relatively high TMR, low RA MTJs. This is beneficial for spin-transfer-torque magnetic random access memories (STT-MRAMs) because the current needed to flip the magnetization of the top electrode can be lowered as the saturation magnetization of the permalloy is low.

Finally in Chapter 5, I described the use of monochromated EELS in the low energy-loss region to probe optical modes of photonic structures and to map the spatial distribution of the modes at nanometer resolution. Finite-size effects of the photonic structures on optical modes, in particular damping of the modes and shifts in mode energies, were also discussed briefly. As relativistic electrons pass near or through dense dielectric media, Cherenkov and transition radiation are emitted. The radiation allows the relativistic electrons to couple to photonic modes because they act as a virtual broad-band light source. Diamond films and waveguides were first studied to confirm that the system was in a relativistic regime where radiation was emitted. Dielectric theory in both

the classical and relativistic regime was used for comparison with experimental data. Then, two-dimensional silicon photonic structures were fabricated using a focused ion beam. The optical modes of the finite size silicon photonic structures were measured and their distributions were mapped out. The measured optical modes were compared to the simulated photonic densities of states obtained by the MIT PB code.

6.2 Future Work

Each project summarized in the previous section suggests promising avenues for future work. Here, I will discuss future plans for the two projects - Mg-B-O-based MTJs and monochromated, low-loss EELS on photonic structures.

6.2.1 Failure mechanisms in Mg-B-O-based magnetic tunnel junctions in nano-pillar shapes

For this thesis, the Mg-B-O-based MTJs were studied in their thin film stack geometry (in bulk wafers). This was possible because the CIPT technique [116] can measure TMR and RA values directly from un-patterned wafers, which speeds up the research considerably. For future work, actual devices using the Mg-B-O barrier layer can be fabricated so that transport measurements on devices can be performed. The Mg-B-O-based MTJ structures will be incorporated in a shape of nano-pillars. Working devices will be intentionally damaged by biasing them with a large voltage, then using spectroscopic imaging, we can compare working and damaged devices. Questions we want to ask are: how stable is the Mg-B-O layer, will BO_x segregate out upon break-down, and will diffusion of additional species occur due to the voltage bias? All of these questions

will help to advance the development of STT-MRAMs, a potential universal memory solution.

Additionally, the Mn diffusion can be investigated further. Mn from the IrMn pinning layer was observed to diffuse into the Mg-B-O layer upon annealing as discussed in Chapter 4 (Figure 4.7). Lee, Ikeda and co-workers attributed the high TMR (500 $\sim$ 600 % at room temperature) obtained with their CoFeB/MgO/CoFeB MTJs to the elimination of Ta diffusion [119] and Mn diffusion [120]. Ta diffusion was suppressed by putting a thicker bottom electrode, while Mn diffusion was prevented by removing the IrMn pinning layer. Therefore, with our Mg-B-O-based MTJs, it is possible that TMR would increase even more if Mn diffusion can be suppressed. The easiest way to suppress the Mn diffusion is by removing the IrMn pinning layer. However without the pinning layer, the overall device structure becomes much more complicated because there are four possible configurations of relative orientations of magnetizations of the electrodes, instead of just two possible configurations that are achieved by pinning the magnetization of the bottom electrode. Another way to achieve the suppression of the Mn diffusion is to create a double bottom electrode stack with a thin Ru insertion layer, creating a synthetic anti-ferromagnic (SAF) pinned layer. The main junction structure would be IrMn / CoFeB / Ru / CoFeB / Mg-B-O / CoFeB, instead of IrMn / CoFeB / Mg-B-O / CoFeB. In this way, Mn diffusion can be suppressed. Using EELS, we would like to confirm that Mn diffusion is minimized when a SAF layer is used in the full stack and that TMR will increase more.

Electronic properties of electrodes with different composition ratios of Co, Fe, and B can be investigated by obtaining reference Co and Fe EEL spectra from electrodes of various composition ratios. By comparing the fine structure of the EELS edge, we hope to illuminate how the inclusion of B into the ferromagnetic electrodes modifies

the overall electronic properties of the electrodes. Since the difference in the fine structures of the EELS edges is expected to be small, a good signal-to-noise ratio and a high energy resolution are required. A NION UltraSTEM, which is equipped with a cold field-emission gun and a 5th order aberration corrector, produces a beam current of $\sim$ 100 pA or higher and has a 0.3 eV energy resolution. Therefore, this study could be carried out using the NION electron microscope. It may also be useful to use a Tecnai F20 scope in monochromated mode to achieve 0.1 eV energy resolution. However the spectra can be noisy in this case because the beam current is reduced considerably in the monochromated mode. Furthermore, we would like to see if B segregation occurs at grain boundaries of these electrodes upon annealing the electrodes using spectroscopic imaging. B segration is suspected because we observe that B diffuses out of the electrodes upon annealing, indicating that B omission in these electrodes is thermodynamically preferable.

6.2.2 Point and linear defects in photonic structures and finite-size effects

The main advantage that electron microscopes offer for probing optical modes with monochromated low-loss EELS is the nanometer spatial resolution, which provides a unique opportunity to investigate local defects such as point and linear defects in photonic structures where these defects are smaller than the wavelength of the light that propagates through the structures. For future work, the effect of point and linear defects on photonic modes in silicon photonic structures can be studied. Figure 6.1a shows as an example a silicon photonic structure with a point defect, which is a smaller hollow cylinder compared to the rest of the cylinders. Figure 6.1b shows the comparison be-

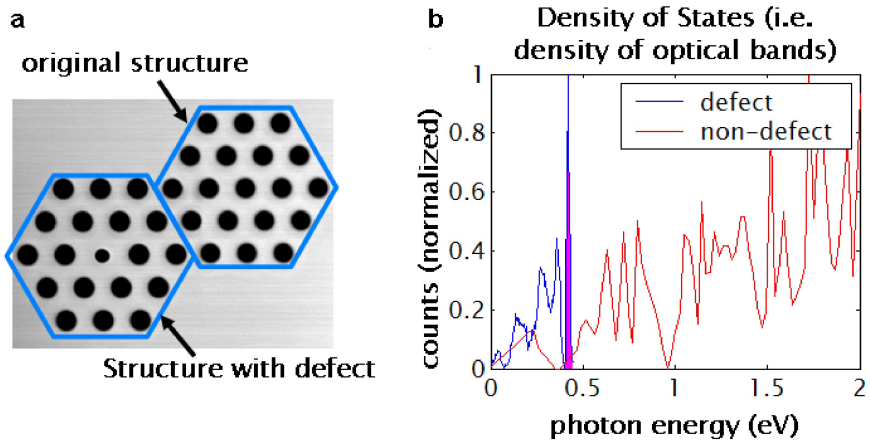

Figure 6.1: Comparative study of photonic structures with and without defects. **a** shows two adjacent photonic structures where one includes a point defect - a smaller cylindrical hole in the center. **b** shows the simulated photonic density of states of the normal and defective photonic structures shown in **a**.

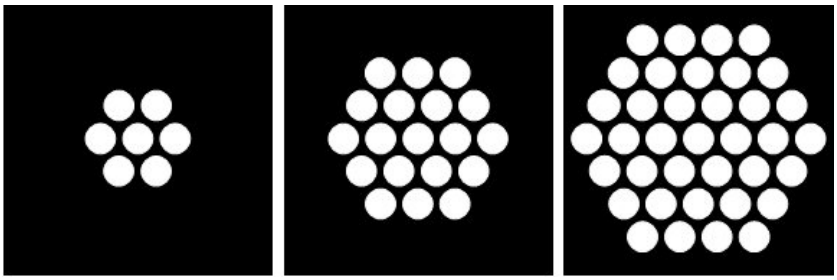

Figure 6.2: Comparative study of photonic structures with increasing structure size. The photonic structure progressively gets larger (from left to right). The photonic modes are expected to shift in their energies as the photonic structure changes in its size.

tween the corresponding simulated photonic density of states of the structures with and without the defect.

Another capability the low-loss EELS provides due to the nanometer probe is the ability to investigate the finite-size effect on photonic modes. Because the electron

probe is localized, photonic modes can be easily excited in structures whose periodicity extends over only a finite region. Treating photonic modes in a finite-size photonic structure as a particle-in-a-box problem, where only a discrete number of energy modes will be allowed for the particle due to the box size, it can be expected that the photonic modes would shift in their energies as a function of the structure size. Figure 6.2 shows, in schematics, a series of photonic structures whose periodic regions become progressively larger. The electron probe will be placed at the center of all three structures (if the EELS intensity is too low due to a weak coupling between the probe and the photonic DOS, the beam should be placed near the edge of the central hollow cylinder), and differences in the peak positions and shapes in the fine structure of low-loss EELS will be investigated.

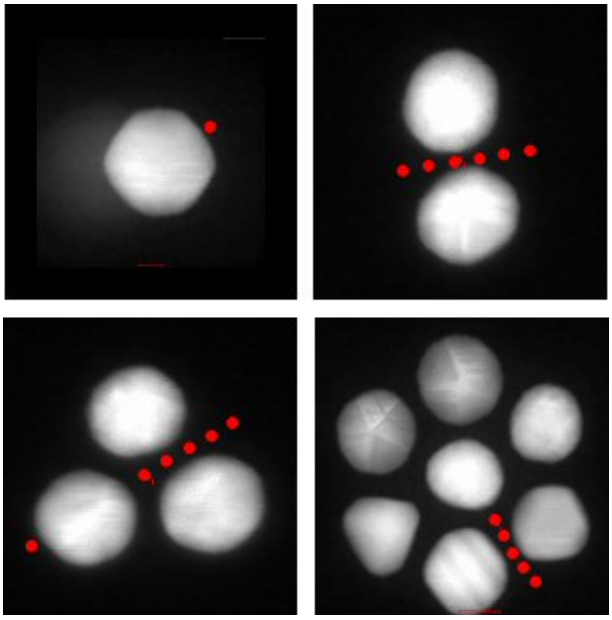

Figure 6.3: Various configurations of gold particles. Coupling of surface plasmons of the gold particles arranged in various configurations will result in either a shift in the plasmon peak, or additional peaks. Monochromated EELS can be used to study the plasmon coupling effect.

Lastly, low-loss EELS is not limited to studying photonic structures. It can be extended to study meta-materials such as plasmonic structures and materials with negative indices [154]. One example would be to study the plasmon coupling of nano-particles as a function of number of particles and distance between the particles [155]. The advantage of using EELS compared to other optical techniques would be again the nanometer resolution. Figure 6.3 shows some interesting configurations of gold particles ($\sim$ 5 nm in diamter), which may result in various plasmon coupling scenarios. The red dots indicate possible probe locations. For this study, silver or aluminum particles would be better than gold because their plasmon energies are higher (above 4 eV) than gold so that the tail of the zero-loss peak does not interfere with plasmons. For gold, the surface plasmon is at $\sim$ 2.2 eV which is low enough that a careful examination of a shift in the plasmon peak due to plasmon coupling is difficult due to the contribution from the zero-loss peak tail intensity. This study requires monochromated EELS.

APPENDIX A

DERIVATION OF ENERGY-BALANCING EQUATION BETWEEN DEFORMATION ENERGY OF NANOTUBES AND SURFACE ENERGIES OF METALS IN CHAPTER 2

In this appendix, I will give a detailed derivation of Equation (2.1) given in the main text of Chapter 2. The schematic diagram shown in Figure A.1 illustrates the assumed, ideal geometry for the wetting and the islanding metal on a carbon nanotube with radius R. The nanotube is assumed single-walled in this calculation although a multiple number of walls does not change the outcome of the calculation.

The energy cost to deform the nanotube is calculated using an elastic theory that treats the nanotube as a thin membrane. Only the radial deformation is considered in this case, giving [91]

$$E_{NT} = \frac{2\pi^2 DL}{\pi R - a} \tag{A.1}$$

where D is the effective bending stiffness of the nanotube, L is the length of the nanotube in the deformed region, R is the radius of the nanotube, and 2a is the flat contact region of the nanotube. The bending stiffness D is defined as $Et^3/12(1-\nu^2)$ where E is the Young's modulus, t is the wall thickness of the nanotube, and ν is the Poisson's ratio. From Ref. [91], D=0.5793 eV is used for the calculation.

Next, the contact surface energy between the metal and the nanotube is calculated by subtracting the binding energy of the metal to the nanotube from the free-surface energy of the contact surface of the metal. The binding energy, u_{bc}, of Au, Pd, and Ti to the nanotube is 0.60, 1.70, and 2.90 eV/atom respectively, obtained from theoretical calculations [68, 92]. To calculate the free-surface energy of the contact surface of the metal, the most stable surface orientation, <111> for Au and Pd and <0001> for Ti, is chosen for the contact surface. Hence, the free-surface energy of the contact surface,

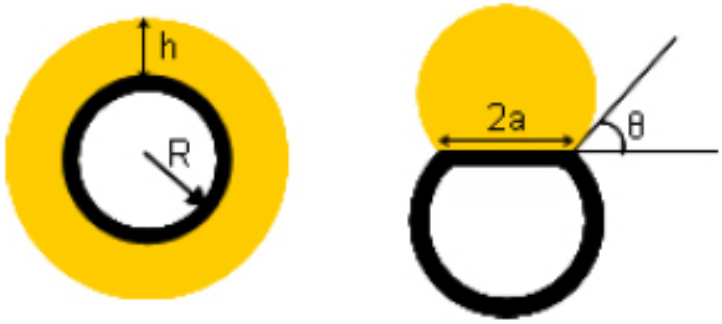

Figure A.1: Schematics of a wetting versus islanding contact on a carbon nanotube. Two extreme cases - an islanding and a wetting metal on a nanotube - are illustrated here. The nanotube is in black while the metal is in yellow. The radial deformation in the nanotube occurs only in the case of islanding metals.

u_{fc}, for Au, Pd, and Ti is 0.61, 0.82, and 1.23 eV/atom respectively [93]. The contact surface energy is then,

$$E_c = \sigma(u_{fc} - u_{bc})S_c \tag{A.2}$$

where σ is the number density of the metal per unit area and S_c is the contact surface area. The number density, σ, is approximately 13.87, 15.27, and 13.26 atoms/nm^2 for Au, Pd, and Ti respectively. For the wetting case, S_c is 2πRL and for the islanding case it is 2aL.

Finally, the remaining free surface energy is calculated. The round shape of the Au-Pd and Pd islands observed experimentally suggests that all crystallographic orientations are present equally for the free remaining surface. Therefore, the averaged free-surface energy per atom, u_{fs}, is used to calculate the remaining free surface energy of the metal island for the Au and Pd islands. For the Ti wetting contact, the surface energy of the <0001> orientation is used because the surface energies of the other surface orientations are too high to form a large free surface area, which is what we observe experimentally.

For Au, Pd, and Ti, u_{fs} is 0.75, 0.99, and 1.23 eV/atom respectively [93]. The remaining free surface energy is then,

$$E_s = \sigma u_{fs} S_s \tag{A.3}$$

where σ is the number density of the metal per unit area, which is assumed the same as above, and S_s is the remaining surface area. For the wetting case, S_s is 2π(R + h)L and for the islanding case, it is (2π-2θ)La/sinθ . Experimentally, θ ranges from approximately 50 degrees to 80 degrees. The general trend that Au would always island while Ti would always wet does not change with θ. Pd shows both wetting and islanding as long as θ is less than 65 degrees. When it is larger than 65 degrees, then Pd shows only islanding. However, ΔE for Pd remains very close to zero regardless of θ so that wetting does not cost too much energy for Pd case. For Figure 2.6, θ = 60 degrees was used.

Combining all three energy terms gives the total energy of the system,

$$E_{tot} = \frac{2\pi^2 DL}{\pi R - a} + (u_{fc} - u_{bc})\sigma S_c + u_{fs}\sigma S_s \tag{A.4}$$

which is Equation (2.1) in the main text in Chapter 2. The volume energy of the metal is not present in Equation (A.4) because the cross-sectional area of the islanding and wetting contact is the same, thus cancelling out the volume energy term.

APPENDIX B

MAKING PHOTONIC CRYSTALS USING A FOCUSED-ION BEAM

Photonic structures that are discussed in Chapter 5 are made using the FEI Strata 400S DualBeam system. In this appendix, I discuss the fabrication process of the photonic structures in detail.

The FEI Strata 400S DualBeam system is equipped with both an electron gun and an ion gun so that milling with the focused ion beam and imaging with the electron beam are allowed simultaneously. A flip stage which holds TEM grids is installed to make it possible to prepare TEM samples using the focused ion beam. A tungsten tip omniprobe is used to lift and move TEM samples.

B.1 Slab Lift-out with Focused Ion Beam

A step-by-step instruction of how to lift out a slab from bulk wafers for TEM samples is described here. A more detailed instruction can be obtained from Mick Thomas from Cornell Center for Materials Research.

1. Set the eucentric height of the sample by slowly bringing the Z height of the stage to 5 mm. A finer eucentric height is done by tilting the bulk stage between 0 and 52 degrees.
2. Tilt the bulk stage to 52 degrees. The ion beam should be normal to the sample surface at this tilt.
3. Launch the AutoTEMG2 software. Select a thick lift-out. Basic settings are width = 15 micron, thickness = 1.5 micron, and depth = 5 micron.

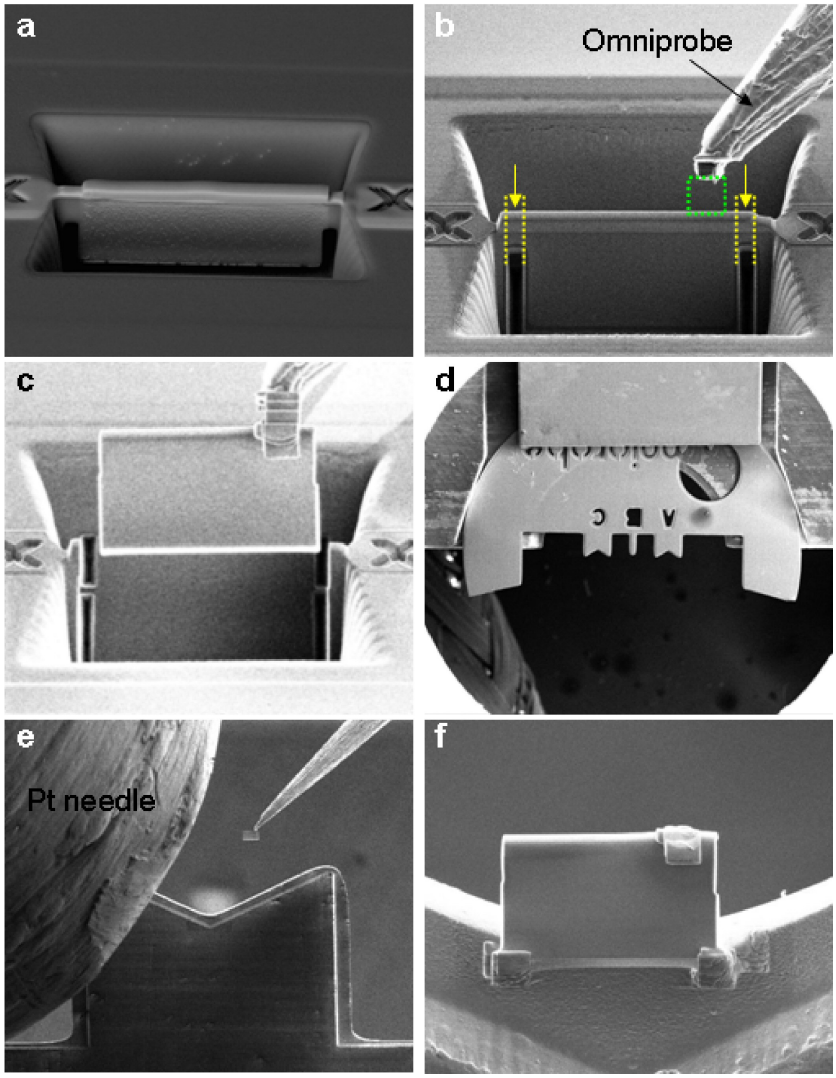

Figure B.1: Lift-out steps using a focused-ion beam. Each panel describes a step in the slab lift-out process.

4. Run the automated thick lift-out job. Figure B.1a shows the result after the automation is completed.
5. Tilt the bulk stage back to 0 degrees. In this setting, the ion beam makes a 52-degree incident angle with the sample surface.
6. At 200 x magnification, insert the Pt needle and then the omniprobe.
7. Slowly position the omniprobe near the slab as shown in Figure B.1b.
8. Attach the omniprobe to the slab by depositing Pt. The green dotted box in Figure B.1b shows the region of Pt deposition. A rule of thumb for an appropriate level of ion current density is $4 \sim 6$ pA per micrometer-squared.
9. Once the omniprobe is securely attached to the slab, mill through the two taps (yellow dotted lines in Figure B.1b) that connect the slab to the bulk sample.
10. Slowly lift the slab up (Figure B.1c) and position the omniprobe at home position, an upper right corner at 200 kX magnification.
11. Retract the omniprobe and the Pt needle.
12. Select the flip stage where the TEM grids are loaded (Figure B.1d). Set the eucentric height of the grids by followng step 1.
13. Insert the Pt needle and then the omniprobe.
14. Slowly bring the omniprobe, which holds a sample now, to the desired location of the grid (Figure B.1e).
15. Attach the slab to the TEM grid using Pt deposition (Figure B.1f).
16. Once the sample is securely glued to the TEM gril, mill through the Pt pad that connects the omniprobe to the slab.
17. Move the omniprobe to the home position. Retract the omniprobe and the Pt needle.

Because it is desired to have a thick slab for 2 dimensional photonic structures, no further thinning is performed on the slab. For high-resolution TEM analysis, the sample in Figure B.1f needs to be thinned until the area of interest is electron-transparent. For further thinning, please ask Mick Thomas from Cornell Center for Materials Research.

B.2 Milling Patterns with Bitmap Images

To mill a periodic pattern precisely, the milling process is automated by using bitmap images, which shortens the milling time compared to manual drawing of patterns on the screen of the FEI FIB software. 24-bit bitmap images were created where blue (0,1,255) means a full beam-on and black (0,0,0) means a beam-off. If the bitmap images are not 24-bit, then errors occur such as milling multiple patterns instead of one pattern or milling wrong size patterns. Typical bitmap images are shown in Figure B.2.

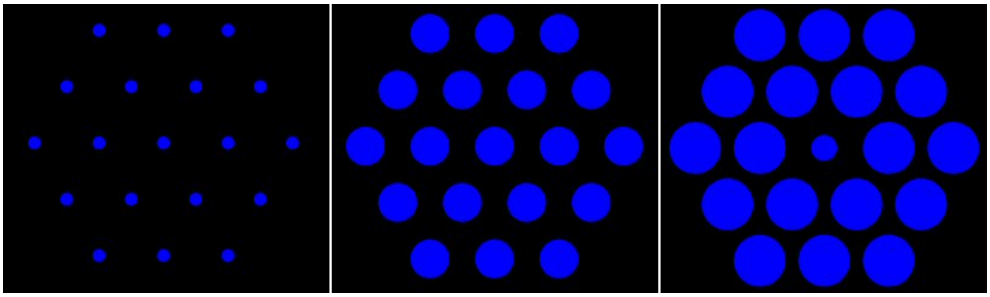

Figure B.2: Example of bitmap images of photonic structures for automated ion milling. Black (0,0,0) means that the ion beam is off while blue (0, 1, 255) means that the ion beam is on.

The bitmap images were loaded into the FEI FIB software, which is explained in detail in the FEI Strata 400S DualBeam mannual. The ion current of 9.7 pA was used for milling. Using higher ion currents was not successful because of a larger ion-beam source size at a higher current. With higher currents, a big hole was punched through

instead of a patterned structure in the slab. To make sure that the slab was milled all the way through, periodically the milling was paused. The bitmap image was shifted with a known displacement so that the milled region could be shown clearly (Figure B.3a and b. The intensity of the milled region was checked against the intensity of vacuum to determine if the slab was milled all the way through. After checking, the bitmap image was shifted back by the known displacement and the milling continued. One should note that the milling is done in a tapering fashion. Figure B.3c shows that the hole at the entrance surface of the slab is larger than the hole at the exit surface of the slab, as indicated by the intensity gradient at the edges of the hole.

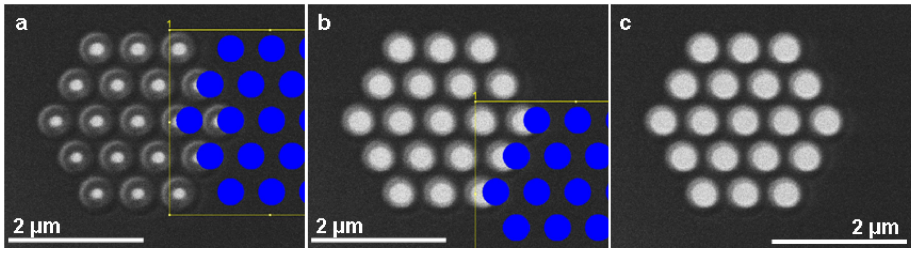

Figure B.3: Milling a pattern into a slab using bitmap images. The milling process was periodically checked by displacing the bitmap images by a known amount and checking the intensity of the milled regions against the intensity of vacuum.

Multiple optical structures were patterned into a single slab. The structures were spaced far from each other to ensure that optical coupling between structures will be negligible. Figure B.4 shows finished samples, which contain several photonic structures in each slab.

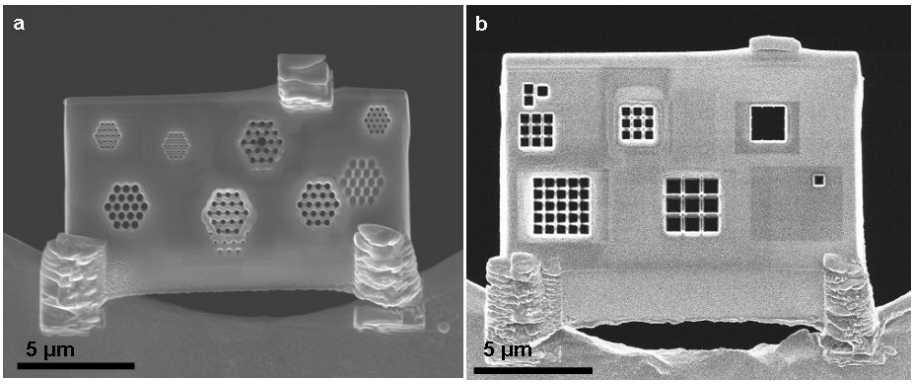

Figure B.4: Photonic structures fabricated with a focused-ion beam. Monochromated EELS on these structures, which probes the photonic densities of states via induced radiation by relativistic electrons, is described in Chapter 5.

BIBLIOGRAPHY

[1] G. Ruthemann. Diskrete energieverluste schneller elektronen in festkorpern. *Naturwissenschaften*, 29:648, 1941.

[2] D. A. Muller. *Electron Energy Loss Spectroscopy*. Lecture notes are available at http://people.ccmr.cornell.edu/~davidm/WEELS/summer06/index.html.

[3] H. A. Bethe. Penetration of fast charged particles throught matter. *Ann. Physik*, 5:325, 1930.

[4] M. Inokuti and B. Bederson. Bethe's contributions to atomic and molecular physics. *Physica Scripta*, 73:C98–C106, 2006.

[5] J. E. Muller and J. W. Willkins. Band structure approach to the X-ray spectra of metals. *Physical Review B*, 29:4331–48, 1984.

[6] D. K. Saldin. The theory of electron energy loss near-edge structure. *Philosopical Magazine B*, 56:515–525, 1987.

[7] M. Nelheibel, P-H. Louf, P. Schattschneider, P. Blaha, K. Schwarz, and B. Jouffrey. Theory of orientation sensitive near edge fine structure core level spectroscopy. *Physical Review B*, 59:12807–14, 1999.

[8] S-P Gao, C. J. Pickard, M. C. Payne, J. Zhu, and J. Yuan. Theory of core-hole effects in 1s core-level spectroscopy of the first-row elements. *Physical Review B*, 77:115122, 2008.

[9] R. F. Egerton. *Electron Energy-Loss Spectroscopy in the Electron Microscope*. Plenum Press, 1986.

[10] P. Rez and D. A. Muller. The theory and interpretation of electron energy loss near-edge find structure. *Annual Reviews of Materials Research*, 38:535–58, 2008.

[11] D. A. Muller. *Near atomic scale studies of electronic structure at grain boundaries in Ni_3Al*. PhD thesis, Cornell Univeristy, 1996.

[12] P. A. Cherenkov. *Dokl. Akad. Nauk SSSR*, 2:451, 1934.

[13] V. L. Ginzburg and I. M. Frank. Uniformly moving electron radiation due to its transition from one medium to another. *Journal of Experimental and Theoretical Physics*, 16:15, 1946.

[14] H. A. Kramers. La diffusion de la lumiere par les atomes. *Transactions of Volta Centenary Congress*, 2:545–557, 1927.

[15] R. de L. Kronig. On the theory of the dispersion of x-rays. *Journal of Optical Society of America*, 12:547–557, 1926.

[16] H. Rose. Prospects for realizing a sub-angstrom sub-eV resolution EFTEM. *Ultramicroscopy*, 78:13–25, 1999.

[17] P. C. Tiemeijer. Measurement of Coulomb interactions in an electron beam monochromator. *Ultramicroscopy*, 78:53–62, 1999.

[18] H. W. Mook and P. Kruit. Construction and characterization of the fringe field monochromator for a field emission gun. *Ultramicroscopy*, 81:129–130, 2000.

[19] M. Stoger-Pollach, C. Hebert, P. Schattschneider, and A. Laister. Retardation effects in valence-EELS spectra. *Microscopy and Microanalysis*, 12 (Suppl. 02):1136–1137, 2006.

[20] M. Stoger-Pollach, A. Laister, and P. Schattschneider. Treating retardation effects in valence EELS spectra for Kramers-Kronig analysis. *Ultramicroscopy*, 108:439–444, 2008.

[21] F. J. Garcia de Abajo, A. G. Pattantyus-Abraham, N. Zabala, A. Rivacoba, M. O. Wolf, and P. M. Echenique. Cherenkov effect as a probe of photonic nanostructures. *Physical Review Letters*, 91:143902, 2003.

[22] F. J. Garcia de Abajo, A. Rivacoba, N. Zabala, and P. M. Echenique. Electron energy loss spectroscopy as a probe of two-dimensional photonic crystals. *Physical Review B*, 68:205105, 2003.

[23] J. K. Hyun, M. Couillard, P. Rajendran, C. M. Liddell, and D. A. Muller. Measuring far-ultraviolet whispering gallery modes with high energy electrons. *Applied Physics Letters*, 93:243106, 2008.

[24] F. J. Garcia de Abajo and M. Kociak. Probing the photonic local density of states with electron energy loss spectroscopy. *Physical Review Letters*, 100:106804, 2008.

[25] J. D. Jackson. *Classical Electrodynamics*. John Wiley and Sons, Inc., 1999.

[26] A. Yurtsever. *Three-dimensional Plasmon Imaging and Photonic States of Silicon Nano-composites by Fast Electrons*. PhD thesis, Cornell Univeristy, 2008.

[27] S. Iijima. Helical microtubules of graphitic carbon. *Nature*, 354:56–57, 1991.

[28] G. Tibbetts. Why are carbon filaments tubular? *Journal of Crystal Growth*, 66:632, 1984.

[29] D. H. Robertson, D. W. Brenner, and J. W. Mintmire. Energetics of nanoscale graphitic tubules. *Physical Review B*, 45:12592–12595, 1992.

[30] B. I. Yakobson, C. J. Brabec, and J. Bernholc. Nanomechanics of carbon tubes: Instabilities beyond linear response. *Physical Review Letters*, 76:2511–2514, 1996.

[31] J. P. Lu. Elastic properties of carbon nanotubes and nanoropes. *Physical Review Letters*, 79:1297, 1997.

[32] N. Hamada, S. Sawada, and A. Oshiyama. New one-dimensional conductors: Graphitic microtubules. *Physical Review Letters*, 68:1579, 1992.

[33] R. Saito, M. Fujita, G. Dresselhaus, and M. S. Dresselhaus. Electronic structure of graphene tubules based on C60. *Physical Review B*, 46:1804, 1992.

[34] J. W. Mintmire and C. T. White. Universal density of states for carbon nanotubes. *Physical Review Letters*, 81:2506, 1998.

[35] C. T. White and J. W. Mintmire. Density of states reflects diameter in nanotubes. *Nature*, 394:29, 1998.

[36] J-Q. Lu, J. Wu, W. Duan, F. Liu, B-F. Zhu, and B-L. Gu. Metal-to-semiconductor transition in squashed armchair carbon nanotubes. *Physical Review Letters*, 90:156601, 2003.

[37] V. H. Crespi, M. L. Cohen, and A. Rubio. In situ band gap engineering of carbon nanotubes. *Physical Review Letters*, 79:2093, 1997.

[38] W. Fa, F. Hu, and J. Dong. Band gap variations in an AFM tip-deformed metallic carbon nanotube. *Physics Letters A*, 331:99–104, 2004.

[39] M. S. C. Mazzoni and H. Chacham. Bandgap closure of a flattened semiconductor carbon nanotube: A first-principles study. *Applied Physics Letters*, 76:1561, 2000.

[40] P. E. Lammert, P. Zhang, and V. H. Crespi. Gapping by squashing: Metal-insulator and insulator-metal transitions in collapsed carbon nanotubes. *Physical Review Letters*, 84:2453, 2000.

[41] O. Gulseren, T. Yildirim, S. Ciraci, and C. Kilic. Reversible band-gap engineering in carbon nanotubes by radial deformation. *Physical Review B*, 65:155410, 2002.

[42] E. D. Minot, Y. Yaish, V. Sazonova, J-Y. Park, M. Brink, and P. L. McEuen. Tuning carbon nanotube band gaps with strain. *Physical Review Letters*, 90:156401, 2003.

[43] T. W. Tombler, C. Zhou, L. Alexseyev, J. Kong, H. Dai, L. Liu, C. S. Jayanth, M. Tang, and S-Y. Wu. Reversible electromechanical characteristics of carbon nanotubes under local-probe manipulation. *Nature*, 405:769–772, 2000.

[44] C. Gomez-Navarro, J. J. Saenz, and J. Gomez-Herrero. Conductance oscillations in squashed carbon nanotubes. *Physical Review Letters*, 96:076803, 2006.

[45] S. J. Tans, A. R. M. Verschueren, and C. Dekker. Room-temperature transistor based on a single carbon nanotube. *Nature*, 393:49–52, 1998.

[46] S. Heinze, J. Tersoff, R. Martel, V. Derycke, J. Appenzeller, and Ph. Avouris. Carbon nanotubes as schottky barrier transistors. *Physical Review Letters*, 89:106801, 2002.

[47] M. Julliere. Tunneling between ferromagnetic films. *Physics Letters*, 54A:225–226, 1975.

[48] R. Meservey and P. M. Tedrow. Spin-polarized electron tunneling. *Physics Reports*, 238:173–243, 1994.

[49] D. Wang, C. Nordman, J. M. Daughton, Z. Qian, and J. Fink. 70 % TMR at room temperature for SDT sandwich junctions with CoFeB as free and reference layers. *IEEE Transactions Magazine*, 40:2269–2271, 2004.

[50] W. H. Butler, X. G. Zhang, T. C. Schulthess, and J. M. MacLaren. Spin-dependent tunneling conductance of Fe / Mgo / Fe sandwiches. *Physical Review B*, 63:054416, 2001.

[51] J. Mathon and A. Umerski. Theory of tunneling magnetoresistance of an epitaxial Fe / MgO / Fe(001) junction. *Physical Review B*, 63:220403, 2001.

[52] S. Yuasa, T. Nagahama, A. Fukushima, Y. Suzuki, and K. Ando. Giant room-temperature magnetoresistance in single-crystal Fe / MgO / Fe magnetic tunnel junctions. *Nature Materials*, 3:868–871, 2004.

[53] S. S. P. Parkin, C. Kaiser, A. Panchula, P. M. Rice, B. Hughes, M. Samant, and S-H. Yang. Giant tunneling magnetoresistance at room temperature with MgO (100) tunnel barriers. *Nature Materials*, 3:862–868, 2004.

[54] D. D. Djayaprawira, K. Tsunekawa, M. Nagai, H. Maehara, S. Yamagata, N. Watanabe, S. Yuasa, Y. Suzuki, and K. Ando. 230 % room-temperature magnetoresistance in CoFeB / MgO / CoFeB magnetic tunnel junctions. *Applied Physics Letters*, 86:092502, 2005.

[55] K. Tsunekawa, D. D. Djayaprawira, M. Nagai, H. Maehara, S. Yamagata, N. Watanabe, S. Yuasa, Y. Suzuki, and K. Ando. Giant tunneling magnetoresistance effect in low-resistance CoFeB / MgO(001) / CoFeB magnetic tunnel junctions for read-head applications. *Applied Physics Letters*, 87:072503, 2005.

[56] S. Yuasa, Y. Suzuki, T. Katayama, and K. Ando. Characterization of growth and crystallization processes in CoFeB / MgO / CoFeB magnetic tunnel junction

structure by reflective high-energy electron diffraction. *Applied Physics Letters*, 87:242503, 2005.

[57] J. D. Joannopoulos, P. R. Villeneuve, and S. Fan. Photonic crystals: putting a new twist on light. *Nature*, 386:143, 1997.

[58] J. D. Joannopoulos, R. D. Meade, and J. N. Winn. *Photonic Crystals*. Princeton University Press, 1995.

[59] E Yablonovitch. Inhibited spontaneous emission in solid-state physics and electronics. *Physical Review Letters*, 58:2059–2062, 1987.

[60] S. John. Strong localization of photons in certain disordered dielectric superlattices. *Physical Review Letters*, 58:2486–2489, 1987.

[61] D. W. Pohl, W. Denk, and M. Lanz. Optical stethoscopy: Image recording with resolution $\lambda/20$. *Applied Physics Letters*, 44:651–653, 1984.

[62] A. Lewis, M. Isaacson, A. Harootunian, and A. Murray. Development of a 500 Å spatial resolution light microscope. I. Light is efficiently transmitted through $\lambda/16$ diameter apertures. *Ultramicroscopy*, 13:227, 1984.

[63] J. J. Cha, W. Weyland, J. F. Briere, I. P. Daykov, T. A. Arias, and D. A. Muller. Three-dimensional imaging of carbon nanotubes deformed by metal islands. *Nano Letters*, 7:3770–3773, 2007.

[64] V. Sazonova, Y. Yaish, H. UstUnel, D. Roundy, T. A. Arias, and P. L. McEuen. A tunable carbon nanotube electromechanical oscillator. *Nature*, 431:284–287, 2004.

[65] W. Kim, A. Javey, R. Tu, J. Cao, Q. Wang, and H. Dai. Electrical contacts to

carbon nanotubes down to 1nm in diameter. *Applied Physics Letters*, 87:173101, 2005.

[66] Z. Chen, J. Appenzeller, J. Knoch, Y. M. Lin, and Ph. Avouris. The role of metal-nanotube contact in the performance of carbon nanotube field-effect transistors. *Nano Letters*, 5:1497–1502, 2005.

[67] W. Zhu and E. Kaxiras. The nature of contact between Pd leads and semiconducting carbon nanotubes. *Nano Letters*, 6:1415–1419, 2006.

[68] B. Shan and K. Cho. Ab initio study of schottky barriers at metal-nanotube contacts. *Physical Review B*, 70:233405, 2004.

[69] N. Nemec, D. Tomanek, and G. Cuniberti. Contact dependence of carrier injection in carbon nanotubes: An ab initio study. *Physical Review Letters*, 96:076802, 2006.

[70] P. A. Midgley and M. Weyland. 3D electron microscopy in the physical sciences: The development of Z-contrast and EFTEM tomography. *Ultramicroscopy*, 96:413–431, 2003.

[71] Y. Zhang and H. Dai. Formation of metal nanowires on suspended single-walled carbon nanotubes. *Applied Physics Letters*, 77:3015–3017, 2000.

[72] D. J. de Rosier and A. Klug. Reconstruction of three dimensional structure from electron micrographs. *Nature*, 217, 1986.

[73] W. Hoppe, R. Langer, G. Rnesch, and C. Poppe. *Naturwissenschaften*, 55:333, 1968.

[74] R. G. Hart. Electron microscopy of unstained biological material: The polytropic montage. *Science*, 159:1464–1467, 1968.

[75] J. S. Barnard, J. Sharp, J. R. Tong, and P. A. Midgley. High-resolution three-dimensional imaging of dislocations. *Science*, 313:319, 2006.

[76] A. Yurtsever, M. Weyland, and D. A. Muller. Three-dimensional imaging of nonspherical silicon nanoparticles embedded in silicon oxide by plasmon tomography. *Applied Physics Letters*, 89:151920, 2006.

[77] P. Ercius, M. Weyland, D. A. Muller, and L. M. Gignac. Three-dimensional imaging of nanovoids in copper interconnects using incoherent bright field tomography. *Applied Physics Letters*, 88:243116, 2006.

[78] R. N. Bracewell. Numerical transforms. *Science*, 248:697–704, 1990.

[79] R. A. Crowther, L. A. Amos, J. T. Finch, D. J. de Rosier, and A. Klug. Three dimensional reconstructions of spherical viruses by fourier synthesis from electron micrographs. *Nature*, 226:421, 1970.

[80] P. Gilbert. Iterative methods for the three-dimensional reconstruction of an object from projections. *Journal of Theoretical Biology*, 36:105–117, 1972.

[81] R. A. Crowther, D. J. de Rosier, and A. Klug. Reconstruction of 3 dimensional structure from projections and its application to electron microscopy. *Proceedings of the Royal Society of London Series A*, 317:319, 1970.

[82] J. Frank. *Electron tomography: Methods for three-dimensional visualization of structures in the cell*. Springer, 1992.

[83] M. Weyland. *Two and three dimensional nanoscale analysis: New techniques and applications*. PhD thesis, University of Cambridge, 2002.

[84] A Howie. Image-contrast and localized signal selection techniques. *Journal of Microscopy*, 117:11–23, 1979.

[85] A. J. Koster, R. Grimm, D. Typke, R. Hegerl, A. Stoschek, J. Walz, and W. Baumeister. Perspectives of molecular and cellular electron tomography. *Journal of Structural Biology*, 120:276–308, 1997.

[86] M. C. Payne, M. P. Teter, D. C. Allan, T. A. Arias, and J. D. Joannopoulos. Iterative minimization techniques for ab initio total-energy calculations: Molecular dynamics and conjugate gradients. *Review of Modern Physics*, 64:1045–1097, 1992.

[87] L. Kleinman and D. M. Bylander. Efficacious form for model pseudopotentials. *Physical Review Letters*, 48:1425, 1982.

[88] T. A. Arias, M. C. Payne, and J. D. Joannopoulos. Ab initio molecular dynamics: Analytically continued energy functionals and insights into iterative solutions. *Physical Review Letters*, 69:1077, 1992.

[89] T. Hertel, R. E. Walkup, and Ph. Avouris. Deformation of carbon nanotubes by surface Van der Waals forces. *Physical Review B*, 58:13870, 1998.

[90] R. Bai, J. Molenaur, and R. B. Pipes. On the flexural characteristics of multi-walled carbon nanotubes. *Materials Research Society Symposium Proceedings*, 858E:HH3.23, 2005.

[91] T. Tang, A. Jagota, and C-Y. Hui. Adhesion between single-walled carbon nanotubes. *Journal of Applied Physics*, 97:074304, 2005.

[92] E. Durgun, S. Dag, V. M. K. Bagci, O. Gulseren, T. Yildirim, and S. Ciraci. Systematic study of adsorption of single atoms on a carbon nanotube. *Physical Review B*, 67:201401, 2003.

[93] L. Vitos, A. V. Ruban, H. L. Skriver, and J. Kollar. The surface energy of metals. *Surface Science*, 411:186–202, 1998.

[94] K. Suenaga, C. Colliex, and S. Iijima. In situe electron energy-loss spectroscopy on carbon nanotubes during deformation. *Applied Physics Letters*, 78:70–72, 2001.

[95] K. Suenaga, E. Sandre, C. Colliex, C. J. Pickard, H. Kataura, and S Iijima. Electron energy-loss spectroscopy of electron states in isolated carbon nanostructures. *Physical Review B*, 63:165408, 2001.

[96] O. Stephan, P. M. Ajayan, C. Colliex, F. Cyrot-Lackmann, and E. Sandre. Curvature-induced bonding changes in carbon nanotubes investigated by electron energy-loss spectroscopy. *Physical Review B*, 53:13824, 1996.

[97] B. Shan, G. W. Lakatos, S. Peng, and K. Cho. First-principles study of band-gap change in deformed nanotubes. *Applied Physics Letters*, 87:173109, 2005.

[98] C-J. Park, Y-H. Kim, and K. J. Chang. Band-gap modification by radial deformation in carbon nanotubes. *Physical Review B*, 60:10656, 1999.

[99] J. Hayakawa, S. Ikeda, Y. M. Lee, F. Matsukura, and H. Ohno. Effect of high annealing temperature on giant tunnel magnetoresistance ratio of CoFeB / MgO / CoFeB magnetic tunnel junctions. *Applied Physics Letters*, 89:232510, 2006.

[100] R. Wang, X. Jiang, R. M. Shelby, R. M. Macfarlane, S. S. P. Parkin, S. R. Bank, and J. S. Harris. Increase in spin injection efficiency of a CoFe / MgO(100) tunnel spin injector with thermal annealing. *Applied Physics Letters*, 86:052901, 2005.

[101] P. X. Xu, V. M. Karpan, K. Xia, M. Zwierzycki, I. Marushchenko, and P. J. Kelly. Influence of roughness and disorder on tunneling magnetoresistance. *Physical Review B*, 73:180402, 2006.

[102] C. Park, J-G. Zhu, M. T. Moneck, Y. Peng, and D. E. Laughlin. Annealing effects on structural and transport properties of rf-sputtered CoFeB/MgO/CoFeB magnetic tunnel junctions. *Journal of Applied Physics*, 99:08A901, 2006.

[103] J. C. Read, P. G. Mather, and R. A. Buhrman. X-ray photoemission study of CoFeB / MgO thin film bilayers. *Applied Physics Letters*, 90:132503, 2007.

[104] P. M. Voyles, J. L. Grazul, and D. A. Muller. Imaging individual atoms inside crystals with ADF-STEM. *Ultramicroscopy*, 96:251–273, 2003.

[105] P. Rez, X. D. Weng, and M. Hong. The interpretation of near edge structure. *Microscopy Microanalysis Microstructures*, 2:143–151, 1991.

[106] D. A. Muller, D. A. Shashkov, R. Benedek, L. H. Yang, J. Silcox, and D. N. Seidman. Atomic scale observations of metal-induced gap states at 222 MgO / Cu interfaces. *Physical Review Letters*, 80:4741, 1998.

[107] M. J. Plisch, J. L. Change, J. Silcox, and R. A. Buhrman. Atomic-scale characterization of a Co / AlO_x / Co magnetic tunnel junction by scanning transmission electron microscopy. *Applied Physics Letters*, 79:391–393, 2001.

[108] S. Kostlmeier and C Elsasser. Ab initio calculation of near-edge structures in electron-energy-loss spectra for metal-oxide crystals. *Physical Review B*, 60:14025, 1999.

[109] P. G. Mather, J. C. Read, and R. A. Buhrman. Disorder, defects, and band gaps in ultrathin (001) MgO tunnel barrier layers. *Physical Review B*, 73:205412, 2006.

[110] J. P. Velev, K. D. Belashchenko, S. S. Jaswal, and E. Y. Tsymbal. Effect of oxygen vacancies on spin-dependent tunneling in Fe / MgO / Fe magnetic tunnel junctions. *Applied Physics Letters*, 90:072502, 2007.

[111] E. Tan, P. G. Mather, A. C. Perrella, J. C. Read, and R. A. Buhrman. Oxygen stoichiometry and instability in aluminum oxide tunnel barrier layers. *Physical Review B*, 71:161401, 2005.

[112] H. L. Meyerheim, R. Popescu, J. Kirschner, N. Jedrecy, M. Sauvage-Simkim, B. Heinrich, and R. Pinchaux. Geometrical and compositional structure at metal-oxide interfaces: MgO on Fe(001). *Physical Review Letters*, 87:076102, 2001.

[113] H. Sauer, R. Brydson, P. N. Rowley, W. Engel, and J. M. Thomas. Determination of coordinations and coordination-specific site occupancies by electron energy-loss spectroscopy: an investigation of boron-oxygen compounds. *Ultramicroscopy*, 49:198–209, 1993.

[114] E. W. Muller, J. A. Panitz, and S. B McLane. The atom-probe field ion microscope. *Review of Scientific Instruments*, 39:83–86, 1968.

[115] T. F. Kelly and M. K Miller. Invited review article: Atom probe tomography. *Review of Scientific Instruments*, 78:031101, 2007.

[116] D. C. Worledge and P. L. Trouilloud. Magnetoresistance measurement of unpatterned magnetic tunnel junction wafers by current-in-plane tunneling. *Applied Physics Letters*, 83:84, 2003.

[117] T. Linn and D. Mauri. Tunneling magnetoresistance (TMR) sensor having a barrier layer made of magnesium-oxide (Mg-O). *United States Patent*, page 20050009211, 2005.

[118] J. Akerman. Toward a universal memory. *Science*, 308:508–510, 2005.

[119] S. Ikeda, J. Hayakawa, Y. Ashizawa, Y. M. Lee, K. Miura, M. Hasegawa, F. Tsunoda, F. Matsukura, and H. Ohno. Tunnel magnetoresistance of 604 % at 300 K

by suppression of Ta diffusion in CoFeB / MgO / CoFeB pseudo-spin-valves annealed at high temperature. *Applied Physics Letters*, 93:082508, 2008.

[120] Y. M. Lee, J. Hayakawa, S. Ikeda, F. Matsukura, and H. Ohno. Effect of electrode composition on the tunnel magnetoresistance of pseudo-spin-valve magnetic tunnel junction with a mgo tunnel barrier. *Applied Physics Letters*, 90:212507, 2007.

[121] X. G. Zhang and W. H. Butler. Large magnetoresistance in bcc Co / MgO / Co and FeCo / MgO / FeCo tunnel junctions. *Physical Review B*, 70:172407, 2004.

[122] J. J. Cha, J. C. Read, R. A. Buhrman, and D. A. Muller. Spatially resolved electron energy-loss spectroscopy of electron-beam grown and sputtered CoFeB / MgO / CoFeB magnetic tunnel junctions. *Applied Physics Letters*, 91:062516, 2007.

[123] C. Y. You, T. Ohkubo, Y. K. Takahashi, and K. Hono. Boron segregation in crystallized MgO / amorphous-$Co_{40}Fe_{40}B_{20}$ thin films. *Journal of Applied Physics*, 104:033517, 2008.

[124] S. Pinitsoontorn, A. Cerezo, A. K. Petford-Long, D. Mauri, L. Folks, and M. J. Carey. Three-dimensional atom probe investigation of boron distribution in CoFeB / MgO / CoFeB magnetic tunnel junctions. *Applied Physics Letters*, 93:071901, 2008.

[125] D. A. Muller, L. F. Kourkoutis, M. Murfitt, J. H. Song, H. Y. Hwang, J. Silcox, N. Dellby, and O. L. Krivanek. Atomic-scale chemical imaging of composition and bonding by aberration-corrected microscopy. *Science*, 319:1073–1076, 2008.

[126] J. Y. Bae, W. C. Lim, H. J. Kim, T. D. Lee, K. W. Kim, and T. W. Kim. Compositional change of MgO barrier and interface in CoFeB / MgO / CoFeB tunnel junction after annealing. *Journal of Applied Physics*, 99:08T316, 2006.

[127] J. C. Read, J. J. Cha, W. F. Jr. Egelhoff, H. W. Tseng, P. Y. Huang, D. A. Muller, and R. A. Buhrman. High magnetoresistance tunnel junctions with Mg-B-O barriers and Ni-Fe-B free electrodes. *Applied Physics Letters*, 94:112504, 2009.

[128] Th. Lindner, H. Sauer, W. Engel, and K. Kambe. Near-edge structure in electron-energy-loss spectra of MgO. *Physical Review B*, 33:22–24, 1986.

[129] P. M. Braganca, I. N. Krivorotov, O. Ozatay, A. G. F. Garcia, N. C. Emley, J. C. Sankay, D. C. Ralph, and R. A. Buhrman. Reducing the critical current for short-pulse spin-transfer switching of nanomagnets. *Applied Physics Letters*, 87:112507, 2005.

[130] Y. Zeng, H. Yang, W. Fu, L. Qiao, L. Chang, J. Chen, H. Zhu, M. Li, and G. Zou. Synthesis of magnesium borate ($Mg_2B_2O_5$) nanowires, growth mechanism and their lubricating properties. *Materials Research Bulletin*, 43, 2008.

[131] H. Wang, G. Jia, Y. Wang, Z. You, J. Li, Z. Zhu, F. Yang, Y. Wei, and C. Tu. Crystal growth and spectral properties of pure and Co^{2+}-doped $Mg_3B_2O_6$ crystal. *Optical Materials*, 29:1635, 2007.

[132] S. L. McCall, P. M. Platzmann, R. Dalichaouch, D. Smith, and S. Schultz. Microwave propagation in two-dimensional dielectric lattices. *Physical Review Letters*, 67:2017, 1991.

[133] C. Chicanne, T. David, R. Quidant, J. C. Weeber, Y. Lacroute, E. Bourillot, A. Dereux, G. Colas des Fracs, and C Girard. Imaging the local density of states of optical corrals. *Physical Review Letters*, 88:097402, 2002.

[134] Earl J. Kirkland. *Advanced Computing in Electron Microscopy*. Plenum Press, 1998.

[135] M. Couillard, A. Yurtsever, and D. A. Muller. Competition between bulk and interface plasmonic modes in valence electron energy-loss spectroscopy of ultrathin SiO_2 gate stacks. *Physical Review B*, 77:085318, 2008.

[136] A. Yurtsever, M. Couillard, and D. A. Muller. Formation of guided Cherenkov radiation in silicon-based nanocomposites. *Physical Review Letters*, 100:217402, 2008.

[137] G. F. Bertsch, H. Esbensen, and B. W. Reed. Electron energy-loss spectrum of nanowires. *Physical Review B*, 58:14031, 1998.

[138] N. Zabala, F. J. Garcia de Abajo, A. Rivacoba, A. G. Pattantyus-Abraham, M. O. Wolf, L. A. Blanco, and P. M. Echenique. Stopping power and Cherenkov radiation in photonic crystals. *Nuclear Instruments and Methods in Physics Research B*, 230:24–30, 2005.

[139] C. H. Chen and J. Silcox. Detection of optical surface guided modes in thin graphite films by high-energy electron scattering. *Physical Review Letters*, 35:390, 1975.

[140] E. Kroger. Berechnung der energieverluste schneller elektronen in dunnen schichten mit retardierung. *Zeitschrift Fur Physik*, 216:115–135, 1968.

[141] J. P. R. Bolton and M. Chen. Electron energy loss in multilayered slabs: II. Parallel incidence. *Journal of Physics*, 7:3389–3403, 1995.

[142] J. P. R. Bolton and M. Chen. Electron energy loss in multilayered slabs: I. Normal incidence. *Journal of Physics*, 7:3373–3387, 1995.

[143] S. G. Johnson and J. D. Joannopoulos. Block-iterative frequency-domain methods for Maxwell's equations in a planewave basis. *Optics Express*, 8:173, 2001.

[144] R. Garcia-Molina, A. Gras-Marti, A. Howie, and R. H. Ritchie. Retardation effects in the interaction of charged particle beams with bounded condensed media. *Journal of Physics C*, 18:5335–5345, 1985.

[145] E. D Palik. *Handbook of Optical Constants*. Academic, 1998.

[146] S. G. Johnson and J. D. Joannopoulos. *MIT Potonic Bands*. The software and the manual are available at http://ab−initio.mit.edu/wiki/index.php/MPB_manual.

[147] H. J. Monkhorst and J. D. Pakc. Special points for Brillouin-zone integrations. *Physical Review B*, 13:5188–5192, 1976.

[148] G. Lehmann and M. Taut. On the numerical calculation of the density of states and related properties. *Phys. Stat. Sol. (b)*, 54:469, 1972.

[149] P. Tiemeijer. *Monochromator manual for Fei Tecnai F20*.

[150] L. R. Saravia and D. Brust. Band structure and interband optical absorption in diamond. *Physics Review*, 170:683–686, 1968.

[151] J. Nelayah, M. Kociak, O. Stephan, F. J. Garcia de Abajo, M. Tence, L. Henrard, D. Taverna, I. Pastoriza-Santos, L. M. Liz-Marzan, and C. Colliex. Mapping surface plasmons on a single metallic nanoparticle. *Nature Physics*, 3:348–353, 2007.

[152] W. H. Richardson. Bayesian-based iterative method of image restoration. *Journal of the Optical Society of America*, 62:55–59, 1972.

[153] L. B. Lucy. An iterative techniques for the rectification of observed distributions. *Astronomical Journal*, 79:745–754, 1974.

[154] V. M. Shalaev. Optical negative-index metamaterials. *Nature Photonics*, 1:41, 2007.

[155] P. E. Batson. Surface plasmon coupling in clusters of small spheres. *Physical Review Letters*, 49:936–940, 1982.